Rheo-dielectric Behavior of Entangled cis-Polyisoprene under Shear Flow(Dissertation_全文)

AUTHOR(S):

Horio, Kazushi

Rheo-dielectric Behavior of Entangled *cis*-Polyisoprene under Shear Flow

Kazushi Horio

2014

Contents

Chapter 4

Dynamical Model with Anisotropic Mobility Tensor for Polymers under Shear

Chapter 5

Rheo-Dielectric Responses of Entangled *cis*-Polyisoprene under Uniform Steady Shear and LAOS

Chapter 1. Introduction

1-1. Overview

Long, flexible polymer chains are deeply overlapping with each other in concentrated systems. Such chains mutually constrain their motion over large length scales, because the real chains cannot pass each other. This constraint results in retarded viscoelastic relaxation of the system, which is referred to as the "entanglement" effect in analogy with bundle of sawing threads.

Dynamics of such entangled polymers under fast and large deformations is one of the important subjects in polymer science and industry. Entangled polymers have long relaxation times and are easily oriented and stretched at deformation rates typically attained in polymer processing. In such a condition, the polymers exhibit non-equilibrium dynamics and, correspondingly, nonlinear viscoelastic behavior.[1-5] For example, entangled polymer melts show a decrease of steady state viscosity with an increase of shear rate, which is referred to as the shear thinning behavior.[1-5] Such nonlinear viscoelasticity and the underlying non-equilibrium dynamics of polymers are of interest from scientific as well as industrial points of view. The non-equilibrium features under the industrial processing conditions, such as the chain orientation/stretch, are preserved in the final products. Thus, it is desired to understand the polymer dynamics in relation to the processing for optimizing the product properties/performance.

Owing to the scientific and industrial interest, experimental investigations have been performed on polymer dynamics under fast and large deformations, in particular for shear deformations. Stratton[6] showed that the steady shear viscosity of entangled monodisperse polystyrene melt decreases on an increase of the shear rate above the terminal relaxation frequency at equilibrium. This result suggests that the polymer chain orientation under flow results in this shear thinning behavior. Menezes and Graessley[7] studied the transient viscosity growth of entangled solutions of monodisperse polybutadiene to report that the transient viscosity shows an overshoot before reaching the steady state. Osaki et al[8] further investigated this overshoot behavior and showed that the peak position is related to the strain imposed through the flow (when the shear is relatively slow) and to a characteristic time for relaxation of the chain stretching (when the shear is fast).

Attempts have been made to explain those experimental results, in particular with the "tube model". Edwards[9] proposed, for the first time, that the motion of mutually overlapping/entangled polymer chains may be treated as the motion of a single chain constrained into a tube-like region surrounding the chain. Then, the large-scale motion is limited along the tube axis (that is essentially the same as the chain backbone). de Gennes[10] showed that the tube idea can explain several power-law relationships between dynamic quantities at equilibrium (such as the diffusion coefficient and relaxation time) and the chain molecular weight. Doi and Edwards[11-13] derived a constitutive equation based on the tube

picture (DE model) to explain the nonlinear damping of the relaxation modulus (stress normalized by the applied strain) on an increase of step shear strain. However, DE model has a flaw in its description of the viscosity under fast shear flow; DE model predicts a decrease of shear stress with an increase of shear rate at shear rates higher than the terminal relaxation frequency at equilibrium. This problem of DE model results from over-orientation of the tube and the chain therein along the flow direction.

Marrucci[14] focused on this problem to propose a mechanism that reduces the orientation under fast shear flow. This mechanism, referred to as "convective constraint release" (CCR), results in contraction of a chain convectively stretched by the shear flow, and this contraction induces disentanglement between the chains to reduce the orientation. The advanced tube models[15-19] incorporating the CCR mechanism are capable to describe quantitatively the nonlinear viscoelastic properties that includes the nonlinear damping under step deformations, the stress overshoot after start-up of fast shear flow, and the shear thinning of the viscosity under fast steady shear flow.

There remain, however, a few open problems that have not been explained theoretically. *Cis*-polyisoprene (PI) has the so-called type-A dipoles parallel along the chain backbone, and its end-to-end fluctuation can be detected as the dielectric relaxation that occurs in the same time scale as the viscoelastic relaxation. Watanabe et al[20] utilized this feature to dielectrically examine the end-to-end fluctuation of monodisperse PI under fast steady shear

flow. For entangled linear PI solutions, the end-to-end fluctuation in the shear gradient direction was found to be insensitive to the shear flow, even at high shear rates where the viscosity exhibited strong shear thinning.[20] On the other hand, for entangled solutions of star-branched PI, the fluctuation was found to be accelerated moderately under fast shear, but the magnitude of this acceleration was much less significant compared to the magnitude of shear thinning of the viscosity. Teixeira et al[21] used fluorescence microscopy to observe the conformational dynamics of individual entangled DNA molecules on start-up of fast shear. They found that the characteristic time of the conformational response is not dependent on the shear rate.

The above results contradict the CCR idea that unavoidably leads to flow-induced acceleration of chain motion/relaxation at shear rates higher than the terminal relaxation frequency at equilibrium. This flow-induced acceleration has been predicted not only from the tube model considering the CCR mechanism but also from the multi-chain sliplink simulation.[22] The simulation does not incorporate the CCR mechanism explicitly, but the force balance between the chains considered in the simulation results in flow-induced, local disentanglements that effectively activate the CCR relaxation. Indeed, some experiments suggested flow-induced acceleration of chain motion. For isotactic polypropylene melt, Somma et al[23] examined effects of small amplitude oscillatory shear superposed on steady shear in the parallel direction. The characteristic relaxation frequency for the (apparent)

storage and loss moduli defined for the superposed oscillatory shear was found to increase (*i.e*., the relaxation was accelerated) with an increase of the steady shear rate. Furthermore, Wang et al[24,25] performed similar experiments for entangled solutions of several DNA and polybutadiene (PBD) samples to report that the acceleration is semi-quantitatively consistent with the CCR theory. The acceleration has been also reported under large amplitude oscillatory shear (LAOS) that periodically stretches/orients the polymer chains in the material: Isayev and Wong[26,27] reported that the fundamental and higher harmonics of the shear stress under LAOS are consistent with the calculation based on the viscoelastic constitutive equation of Leonov,[28,29] although there were some deviations for storage modulus (corresponding to the fundamental component).

In relation to the problems mentioned above, a question is to be asked from an experimental viewpoint for the *flow uniformity* that has been implicitly but widely assumed in the molecular theories/models. Tapadia et al[30,31] utilized micrometer-sized tracer particles to examine the flow profile in entangled solutions. They utilized a cone-plate geometry, the geometry widely used in rotational rheometer to measure shear viscosity, that is supposed to give a uniform flow field. Nevertheless, Tapadia et al found that the velocity profile in the entangled PB solutions is not uniform but split into two flow regions with different shear rates. Furthermore, Wang et al[32] reported that the flow non-uniformity emerges when a rotation speed of the cone-plate geometry exceeds a certain critical value and this critical value

depends on the material. If the flow were not uniform at the conditions for the experiments mentioned earlier, it is not so straightforward to discuss the nonlinear viscoelastic behavior in relation to the CCR mechanism.

Thus, there still remain open problems for the polymer dynamics under fast and large deformations, in particular for the shear effect on the chain relaxation time under fast, uniform shear flow. For this problem, it is necessary to systematically measure the flow profile, rheological response, and the dielectric response of a given entangled PI system(s) under the same flow/deformation condition. Furthermore, explanation is desired if the results of such measurements contradict the CCR theory.

1-2. Scope of this thesis

Concerning the questions asked in the previous section, this thesis makes detailed investigation of viscoelastic and dielectric behavior for entangled PI chains under fast shear with both theoretical and experimental approaches. The dielectric response of PI chains detects fluctuation of the end-to-end fluctuation in the direction of the shear gradient, whereas the viscoelastic response reflects the orientational anisotropy of the chains. For the theoretical approach, the molecular expression of the dielectric response under fast steady shear and LAOS is formulated on the basis of the Langevin analysis and Green-Kubo theorem. Anisotropy of local friction, that could have different effects on the viscoelastic and dielectric

responses under fast shear flow, is theoretically analyzed as well. For the experimental approach, well-characterized linear and star-branched PI samples are examined to elucidate the flow-induced acceleration. The flow profile is also investigated to guarantee the flow uniformity in these experiments.

This thesis is composed of six chapters.

Chapter 1 (this chapter) provides the overview and scope.

Chapter 2 summarizes current molecular pictures for the entangled polymer dynamics.

In Chapter 3, a theoretical analysis is conducted for the molecular expression of the dielectric response of the type-A PI chains under steady shear and LAOS. The expression relates the response to the conformational dynamics of the PI chains.

Chapter 4 describes a simple dynamic model of polymers having an anisotropic mobility tensor under fast shear. The shear viscosity, the dielectric response function, and the relaxation modulus under shear flow are deduced from the model.

Chapter 5 is devoted for experimental tests of the rheo-dielectric behavior of entangled solutions of linear and star-branched PI under uniform steady shear and LAOS. The particle tracking velocimetry (PTV) experiments are also conducted to examine if the shear-insensitivity of the rheo-dielectric responses (already reported in literature[20]) is the real feature under uniform shear without shear-banding and/or secondary flow. In fact, the shear uniformity was confirmed. Thus, the rheo-dielectric difference between the linear and star

PI suggests an essential difference of the entanglement dynamics of linear and star chains, and this difference is discussed within the context of the current molecular idea.

Finally, Chapter 6 gives the summary of the thesis.

References

1) J. D. Ferry, Viscoelastic Properties of Polymers, (Wiley, New York, 1980).

2) H. Watanabe, Progress in Polymer Science, 24, 1253 (1999).

3) T. C. B. McLeish, Advances in Physics, 51, 1379 (2002).

4) W. W. Graessley, Advances in Polymer Science, 16 (1974).

5) M. Rubinstein, R. H. Colby, Polymer Physics, (Clarendon Press, Oxford, 2003)

6) R. A. Stratton, The Journal of Colloid and Interface Science, 22, 517 (1966).

7) E. V. Menezes, W. W. Graessley, Journal of Polymer Science: Polymer Physics Ed., 20, 1817 (1982).

8) K. Osaki, T. Inoue, T. Uematsu, Journal of Polymer Science : Polymer Physics Ed., 38, 3271 (1985).

9) S. F. Edwards, Proceedings of the Physical Society 92, 9 (1967).

10) P. G. de Gennes , The Journal of Chemical Physics, 55, 572 (1971).

11) M. Doi and S. F. Edwards, Journal of the Chemical Society, Faraday Transactions 2 74,

1789 (1978).

12) M. Doi and S. F. Edwards, Journal of the Chemical Society, Faraday Transactions 2 74, 1818 (1978).

13) M. Doi, S. F. Edwards, The Theory of Polymer Dynamics, (Clarendon Press, Oxford, 1986).

14) G. Marrucci, Journal of Non-Newtonian Fluid Mechanics, 62, 279 (1996).

15) G. Ianniruberto, G. Marrucci, Journal of Non-Newtonian Fluid Mechanics, 65, 241 (1996).

16) D. W. Mead, R. G. Larson, M. Doi, Macromolecules, 31, 7895 (1998).

17) S. T. Milner, T. C. B. McLeish, A. E. Likhtman, Journal of Rheology, 45, 539 (2001).

18) A. E. Likhtman, R. S. Graham, Journal of Non-Newtonian Fluid Mechanics, 144, 1, (2003).

19) R. S. Graham, A. E. Likhtman, T. C. B. McLeish, Milner, S. T. Milner, Journal of Rheology, 47, 1171 (2003).

20) H. Watanabe, S. Ishida, Y. Matsumiya, Macromolecules, 35, 8802 (2002).

21) R. E. Teixeira, A. K. Dambal, D. H. Richter, E. S. G. Shaqfeh, S. Chu, Macromolecules, 40, 2461(2007).

22) Y. Masubuchi, H. Watanabe, G. Ianniruberto, F. Greco, G. Marrucci, Nihon Reoroji Gakkaishi (Journal of the Society of Rheology, Japan), 32, 197 (2004).

23) E. Somma, O. Valentino, G. Titomanlio, G. Ianniruberto, Journal of Rheology, 51, 987, (2007).

24) P. E. Boukany, S. Q. Wang, Journal of Rheology, 53, 1425 (2009).

25) X. Li, S. Q. Wang, Macromolecules, 43, 5904 (2010).

26) A. I. Isayev, C. M. Wong, Journal of Polymer Science Part B: Polymer Physics, 26, 2303 (1988).

27) C. M. Wong, A. I. Isayev, Rheologica Acta, 28, 176, (1989).

28) A. I. Leonov, Rheologica Acta, 15, 85 (1976)

29) A. I. Leonov, E. H. Lipkina, E. D. Paskhin, A. N. Prokunin Rheologica Acta, 15, 411 (1976)

30) P. Tapadia, S. Q. Wang, Physical Review Letters, 91, 198301 (2003).

31) P. Tapadia, S. Ravindranath, S. Q. Wang, Physical Review Letters, 96, 196001 (2006).

32) S. Q. Wang, S. Ravindranath, P. E. Boukany, Macromolecules, 44, 183, (2011).

Chapter 2. Theoretical Basics and Literature Data

2-1. Microscopic Expression of Relaxation Functions at Equilibrium

2-1-1. *Viscoelastic properties*

For polymeric liquids, the stress tensor $\boldsymbol{\sigma}(t)$ in long time scales (after completion of glassy relaxation) is intimately related to anisotropy of the orientation distribution of the subchains of the constituent polymer chains. Specifically, for the liquid of monodisperse chains each being composed of N subchains and altogether having the number density ν (cf. Fig. 2-1), $\boldsymbol{\sigma}(t)$ can be expressed in terms of the end-to-end vector of nth subchain at time t, $\mathbf{u}(n,t)$, as:[1-3)]

$$\boldsymbol{\sigma}(t) = 3\nu k_{\mathrm{B}}T\sum_{n=1}^{N}\mathbf{S}(n,t) - p\mathbf{I} \tag{2-1a}$$

with

$$\mathbf{S}(n,t) = \left\langle \frac{\mathbf{u}(n,t)\mathbf{u}(n,t)}{gb^2} \right\rangle_{\gamma} \tag{2-1b}$$

Here, k_{B} and T are the Boltzmann constant and the absolute temperature, respectively, p is the isotropic pressure, and $\mathbf{I}$ is the unit tensor. The orientation tensor $\mathbf{S}(n,t)$ defined by Eq. 2-1b is expressed in terms of the dyadic of the subchain bond vector, $\mathbf{uu}$, the number of monomeric segments *per* subchain, g, and the effective step length of the monomeric segment, b. (The factor gb^2 gives the mean-square end-to-end distance of the subchain at equilibrium.) $\langle\cdots\rangle_{\gamma}$ represents the

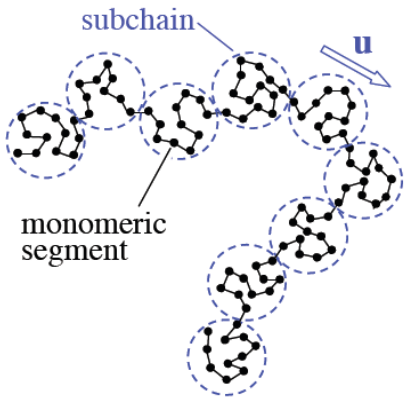

Fig. 2-1. Schematic illustration of chain and subchain.

ensemble average over the subchains under strain γ. Eq. 2-1 means that the stress is equivalent to the orientational anisotropy of the subchains that can be detected as an optical anisotropy. This equivalence is the basis for the experimentally established stress-optical rule being valid in long time scales after completion of glassy relaxation.[4-6] Eq. 2-1 serves as the basis for modeling rheology of polymeric liquids just through analysis of the chain motion (time evolution of $\mathbf{u}(n,t)$).

2-1-2. *Dielectric properties*

For a dielectric material, the electrical displacement $D(t)$ (macroscopic charge) is stored under a constant electric field E and decays on removal of the field.[7,8] $D(t)$ is proportional to E when E is small, and a normalized dielectric relaxation function in the linear response regime, $\Phi(t)$, is defined as $D(t)/D(0)E$, where $D(t)$ denotes the electrical displacement that decays with time t (> 0) after its full evolution (to have the value $D(0)$) under the electric field E at $t < 0$.

In the linear response regime, $\Phi(t)$ ($\equiv D(t)/D(0)E$) is related to fluctuation of a microscopic polarization $\mathbf{P}(t)$ and expressed as the auto-correlation function,[7-9]

$$\Phi(t) = \frac{\langle P_E(t) P_E(0) \rangle_{eq}}{\langle P_E^2 \rangle_{eq}} \qquad (2\text{-}2a)$$

Here, P_E is the component of $\mathbf{P}$ in the direction of the electric field, and $\langle \cdots \rangle_{eq}$ denotes the ensemble average at equilibrium without any field (electric and shear fields, for example). If

the material is isotropic and homogeneous, Eq. 2-2a can be rewritten as:[7-9)]

$$\Phi(t) = \frac{\langle \mathbf{P}(t) \bullet \mathbf{P}(0) \rangle_{eq}}{\langle \mathbf{P}^2 \rangle_{eq}} \qquad (2\text{-}2b)$$

The microscopic polarization $\mathbf{P}(t)$ is given by a sum of all dipoles $\mathbf{m}$ in a unit volume:[7,8)]

$$\mathbf{P}(t) = \sum_j \mathbf{m}_j(t) \qquad (2\text{-}3)$$

Some polymers such as *cis*-polyisoprene (PI) have the so-called type-A dipoles $\mathbf{m}_A$ that are parallel along the chain backbone. $\mathbf{m}_A$ is expressed in terms of the bond vector of subchains $\mathbf{u}(n,t)$ as $\mathbf{m}_A(n,t) = m\mathbf{u}(n,t)$, with m being the magnitude of the dipole per unit length of the backbone.[10)] From Eq. 2-3, $\mathbf{P}(t)$ of such type-A polymers in the long time scale can be expressed as:[8)]

For linear chain without dipole inversion

$$\mathbf{P}(t) = \Sigma_n m\mathbf{u}(n,t) = m\mathbf{R}(t) \qquad (2\text{-}4a)$$

For star-branched chain with the arm dipoles converging to the branching point

$$\mathbf{P}(t) = \Sigma_\alpha \Sigma_n m\mathbf{u}_\alpha(n,t) = m\Sigma_\alpha \mathbf{R}_{arm}^{[\alpha]}(t) \qquad (2\text{-}4b)$$

$\mathbf{R}(t)$ appearing in Eq. 2-4a denotes the end-to-end vector of the linear chain at time t, and $\mathbf{R}_{arm}^{[\alpha]}(t)$ in Eq. 2-4b, the end-to-branching point vector of αth arm at time t. Eqs. 2-2 and 2-4 give the molecular expression of the normalized dielectric relaxation function of type-A polymers (at long t where the so-called type-B dipoles perpendicular to the chain backbone, *if any*, have fully relaxed):[8)]

$$\Phi(t) = \frac{\left\langle \mathbf{R}(t) \bullet \mathbf{R}(0) \right\rangle_{\mathrm{eq}}}{\left\langle \mathbf{R}^2 \right\rangle_{\mathrm{eq}}} \qquad \text{(for linear polymer)} \qquad (2\text{-}5)$$

$$\Phi(t) = \frac{\sum_{\alpha,\beta=1}^{q} \left\langle \mathbf{R}_{\mathrm{arm}}^{[\alpha]}(t) \bullet \mathbf{R}_{\mathrm{arm}}^{[\beta]}(0) \right\rangle_{\mathrm{eq}}}{q\left\langle \mathbf{R}_{\mathrm{arm}}^2 \right\rangle_{\mathrm{eq}}} \qquad \text{(for } q\text{-arm star polymer)} \qquad (2\text{-}6)$$

The dielectric relaxation intensity Δε is related to mean-square end-to-end distance $\left\langle R^2 \right\rangle_{\mathrm{eq}}$ and/or mean-square end-to-branching point distance $\left\langle R_{\mathrm{arm}}^2 \right\rangle_{\mathrm{eq}}$ as:[7,8)]

$$\Delta\varepsilon = F\left(\frac{4\pi m^2}{3k_{\mathrm{B}}T}\right)\nu\left\langle R^2 \right\rangle_{\mathrm{eq}} \qquad \text{(for linear polymer)} \qquad (2\text{-}7a)$$

$$\Delta\varepsilon = F\left(\frac{4\pi m^2}{3k_{\mathrm{B}}T}\right)\nu q\left\langle R_{\mathrm{arm}}^2 \right\rangle_{\mathrm{eq}} \text{ (for } q\text{-arm star polymer)} \qquad (2\text{-}7b)$$

Here, ν is the number density of the chains, and F is a correction factor for a difference in the strengths of microscopic and macroscopic electric fields.

2-1-3. *Responses against oscillatory field.*

The linear response is most fundamentally defined as the response against a constant stimulus (*e.g.*, strain and electric field) step-wisely applied to a material at times $t > 0$. Specifically, the shear stress $\sigma(t)$ against a step strain γ and the polarization $P(t)$ against a step electric field E are described as

$$\sigma(t) = G(t)\gamma, \quad P(t) = P(\infty)\{1-\Phi(t)\}E \qquad (2\text{-}8)$$

where $G(t)$ and $\Phi(t)$ denote the relaxation modulus and normalized dielectric relaxation function, respectively. $G(t)$ and $\Phi(t)$ are related to the chain conformation through Eqs. 2-1,

2-5, and 2-6.

In actual measurements, however, the step stimulus is not so frequently utilized. Instead, most of measurements are made with sinusoidal stimuli oscillating with the angular frequency ω, $\gamma(t) = \gamma_0 \sin \omega t$ and $E(t) = E_0 \sin \omega t$. The responses for these stimuli are described as

$$\sigma(t) = \gamma_0 \left\{ G'(\omega) \sin \omega t + G''(\omega) \cos \omega t \right\} \tag{2-9}$$

$$P(t) = E_0 \varepsilon_{\mathrm{vac}} \left\{ \varepsilon'(\omega) \sin \omega t - \varepsilon''(\omega) \cos \omega t \right\} \tag{2-10}$$

where $\varepsilon_{\mathrm{vac}}$ (= 8.85×10^{-12} $\mathrm{C^2\ J^{-1}\ m^{-1}}$) is the absolute dielectric permittivity of vacuum. The storage and loss moduli, $G'(\omega)$ and $G''(\omega)$, are related to the normalized relaxation modulus $\mu(t) = G(t)/G_0$ and the initial modulus $G_0 = G(0)$ (viscoelastic relaxation intensity) as

$$G^*(\omega) \equiv G'(\omega) + iG''(\omega) = i\omega G_0 \int_0^\infty \mu(t)\, e^{-i\omega t}\, \mathrm{d}t \quad (i = \sqrt{-1}) \tag{2-11}$$

Similarly, the dynamic dielectric permittivity $\varepsilon'(\omega)$ and dielectric loss $\varepsilon''(\omega)$ are related to the normalized dielectric relaxation function $\Phi(t)$ and the dielectric intensity $\Delta\varepsilon$ as

$$\Delta\varepsilon^*(\omega) \equiv \left\{ \varepsilon'(0) - \varepsilon'(\omega) \right\} + i\varepsilon''(\omega) = i\omega\Delta\varepsilon \int_0^\infty \Phi(t)\, e^{-i\omega t}\, \mathrm{d}t \tag{2-12}$$

Thus, the ω dependence of $G^*(\omega)$ and $\Delta\varepsilon^*(\omega)$ represents the relaxation mode distribution of $\mu(t)$ and $\Phi(t)$, respectively. This mode distribution can be explicitly described in terms of the normalized viscoelastic and dielectric relaxation spectra $\{g_p, \tau_{G,p}\}$ and $\{h_p, \tau_{\varepsilon,p}\}$, as

$$\mu(t) = \sum_{p\geq 1} g_p \exp\left(-\frac{t}{\tau_{G,p}} \right), \quad G^*(\omega) = G_0 \sum_{p\geq 1} g_p \frac{\omega^2\tau_{G,p}^2 + i\omega\tau_{G,p}}{1 + \omega^2\tau_{G,p}^2} \tag{2-13}$$

$$\Phi(t) = \sum_{p\geq 1} h_p \exp\left(-\frac{t}{\tau_{\varepsilon,p}} \right), \quad \Delta\varepsilon^*(\omega) = \Delta\varepsilon \sum_{p\geq 1} h_p \frac{\omega^2\tau_{\varepsilon,p}^2 + i\omega\tau_{\varepsilon,p}}{1 + \omega^2\tau_{\varepsilon,p}^2} \tag{2-14}$$

Eqs. 2-13 and 2-14 are the basic equations that relate the $G^*(\omega)$ and $\Delta\varepsilon^*(\omega)$ data to the viscoelastic and dielectric mode relaxation times, $\tau_{G,p}$ and $\tau_{\varepsilon,p}$, and the normalized mode intensities, g_p and h_p. Specifically, $G^*(\omega)$ and $\Delta\varepsilon^*(\omega)$ exhibit characteristic power-law behavior at sufficiently low frequencies, $\omega << 1/\tau_{G,1}$ and/or $1/\tau_{\varepsilon,1}$:

$$G'(\omega) = \omega^2 G_0 \sum_{p\geq 1} g_p \tau_{G,p}^2 \propto \omega^2 \tag{2-15a}$$

$$G''(\omega) = \omega G_0 \sum_{p\geq 1} g_p \tau_{G,p} \propto \omega \tag{2-15b}$$

$$\Delta\varepsilon'(\omega) \equiv \varepsilon'(0) - \varepsilon'(\omega) = \omega^2 \Delta\varepsilon \sum_{p\geq 1} h_p \tau_{\varepsilon,p}^2 \propto \omega^2 \tag{2-16a}$$

$$\varepsilon''(\omega) = \omega \Delta\varepsilon \sum_{p\geq 1} h_p \tau_{\varepsilon,p}^2 \propto \omega \tag{2-16a}$$

The second moment average relaxation time, being close to the relaxation time $\tau_{G,1}$ and/or $\tau_{\varepsilon,1}$ of the slowest mode, is defined with respect to the low-ω asymptotes described by Eqs. 2-15 and 2-16 as

$$\tau_G \equiv \frac{\sum_{p\geq 1} g_p \tau_{G,p}^2}{\sum_{p\geq 1} g_p \tau_{G,p}} = \left[\frac{G'(\omega)}{\omega G''(\omega)}\right]_{\omega\to 0}, \quad \tau_\varepsilon \equiv \frac{\sum_{p\geq 1} h_p \tau_{\varepsilon,p}^2}{\sum_{p\geq 1} h_p \tau_{\varepsilon,p}} = \left[\frac{\Delta\varepsilon'(\omega)}{\omega\varepsilon''(\omega)}\right]_{\omega\to 0} \tag{2-17}$$

2-2. Literature Data under Fast Shear Flow

Entangled polymer chains are in a non-equilibrium state under fast flow. Namely, the chains are oriented under flow at rates larger than the terminal relaxation frequency at equilibrium, and also stretched at rates larger than the Rouse relaxation frequency for the whole backbone of the chain.[1-3] Nevertheless, the chains exhibit linear responses against

small stimuli (such as small oscillatory strain[11,12] and weak electric field[13,14]) superposed on the fast flow, although the relaxation functions underlying such linear responses are not necessarily expressed in terms of the chain conformation in the same way as for the responses at equilibrium explained in section 2-1.[15]

As an example of the linear response under fast shear flow, Fig. 2-2 shows the storage modulus $G'_{//}$ of an entangled linear isotactic polypropylene (iPP) melt, having $M_w = 3.8 \times 10^5$ and $M_w/M_n = 6.8$, measured at 220°C against a small-amplitude oscillatory shear superimposed parallel to the steady shear flow.[12] The steady shear was attained at the stresses as indicated, and the shear rate $\dot{\gamma}$ increased from 0.01 s^{-1} to 1 s^{-1}, the latter being well beyond the terminal viscoelastic relaxation frequency at equilibrium, $1/\tau_G(0)$ (< 0.01 s^{-1}). Clearly, the terminal relaxation of $G'_{//}$ is accelerated on an increase of the rate $\dot{\gamma}$ of the background steady shear. This behavior has been related to the acceleration of viscoelastic relaxation due to the convective constraint release (CCR) mechanism explained in Chapter 1.[12]

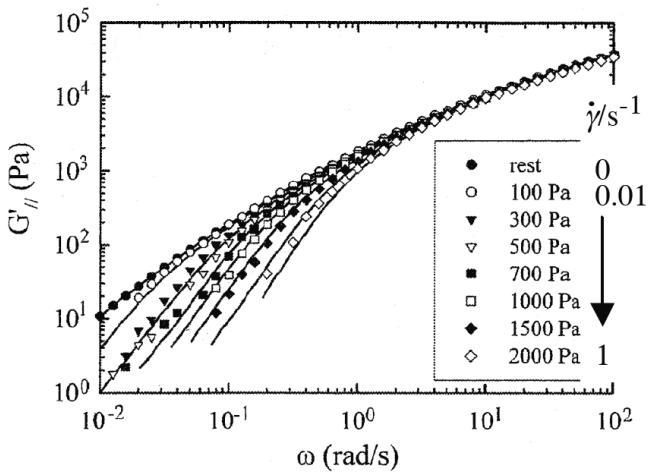

Fig. 2-2. Storage modulus $G'_{//}$ of entangled linear iPP melt at 220°C measured against small oscillatory strain superposed parallel to the steady shear.[12] The steady shear was attained at stresses as indicated.[12]

Fig. 2-3 shows another example, the dielectric loss ε'' of a linear *cis*-polyisoprene (PI) solution ($M_w = 1.19 \times 10^6$, $M_w/M_n = 1.11$, dissolved in a vinyl-rich oligomeric butadiene at 15 wt%).[13] The measurement was performed at 30°C under a weak electric field applied in the shear gradient direction, and the shear rate was increased well beyond the terminal viscoelastic relaxation frequency at equilibrium, $1/\tau_G(0)$ (= 0.014 s^{-1}).[13] Contradictory to the storage modulus data shown in Fig. 2-2, the dielectric loss data are hardly affected by the shear flow, even at high shear rates where the viscosity exhibited significant thinning.[13]

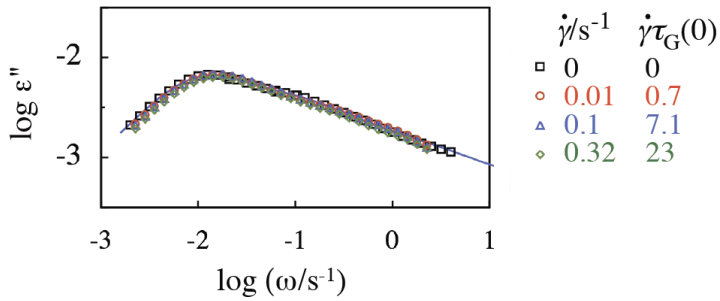

Fig. 2-3. Dielectric loss ε'' of an entangled PI solution at 30°C measured against a weak electric field superposed perpendicular to the steady shear at the rates as indicated.[13]

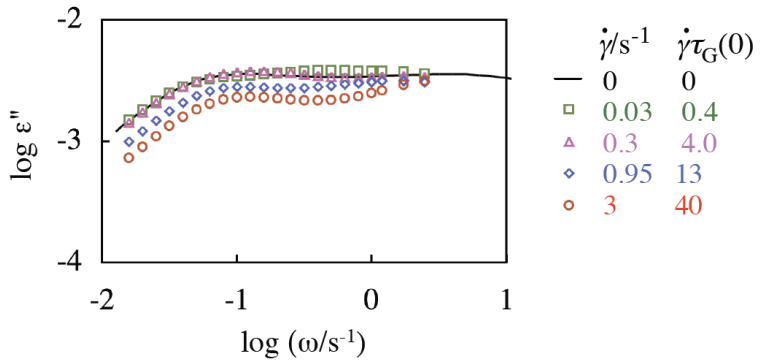

Fig. 2-4. Dielectric loss ε'' of an entangled 6-rm star PI solution at 25°C measured against a weak electric field superposed perpendicular to the steady shear at the rates as indicated.[13]

Remarkably, the dielectric behavior of star polymers is affected by the shear. Fig. 2-4

shows ε'' data of a 6-arm star-branched PI solution (the arm molecular weight $M_{arm} = 1.79 \times 10^5$, $M_w/M_n = 1.03$, dissolved in a vinyl-rich oligomeric butadiene at 20wt%) measured at 25°C.[13] The shear rate was increased well beyond $1/\tau_G(0)$ (= 0.076 s^{-1}) [13], and the terminal dielectric relaxation is accelerated moderately and the dielectric intensity decreases a little at such high rates.

2-3. Current Models for Entangled Polymer Dynamics

2-3-1. *Tube models for linear chain at equilibrium*

It has been established that the polymer dynamics in entangled state can be cast into the dynamics of single chain confined in the tube. Edwards[16] and de Gennes[17] considered that diffusion of a linear chain lateral to its backbone is significantly suppressed because the chain is trapped in a parabolic potential in the lateral direction. Thus, they assumed that the linear chain is constrained within a tube having the diameter a (formed by surrounding the chain), and that the slow dynamics of the chain is governed by the curvilinear diffusion along the tube referred to as "reptation". (Formulation of the reptation dynamics is summarized in Appendix 2A.) During the reptation process, the chain backbone is considered to keep its equilibrium length, as shown in Fig. 2-5.

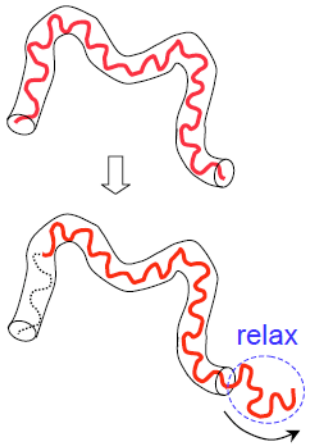

Fig. 2-5. Schematic illustration of reptation of linear chain in a fixed tube (of diameter a).

Linear viscoelastic behavior predicted from the pure reptation mechanism is, however, not in quantitative agreement with experiments. For instance, the relaxation time of the linear chain observed in experiments is shorter and more strongly dependent on the molecular weight compared to the reptation prediction.[18)]

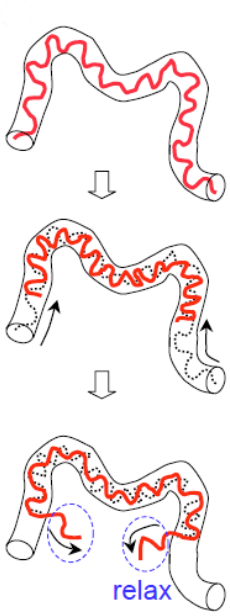

Fig. 2-6. Schematic illustration of CLF of linear chain in a tube.

Because of such disagreements, the tube model for the linear chain has been refined through incorporation of additional relaxation mechanisms referred to as the "contour length fluctuation" (CLF)[18,19)] and "constraint release" (CR)[18)] depicted in Figs. 2-6 and 2-7. The CLF mechanism results in fluctuation of the curvilinear length of the chain along the tube, thereby shortening the effective length of the tube to accelerate the relaxation. In contrast, the CR mechanism allows the chain to fluctuate in a direction lateral to the tube axis over a distance larger than the tube diameter *a*, thereby activating local relaxation as depicted in the top three cartoons in Fig. 2-7. The tube model is intrinsically a mean-field model for *single chain*, but incorporation of the

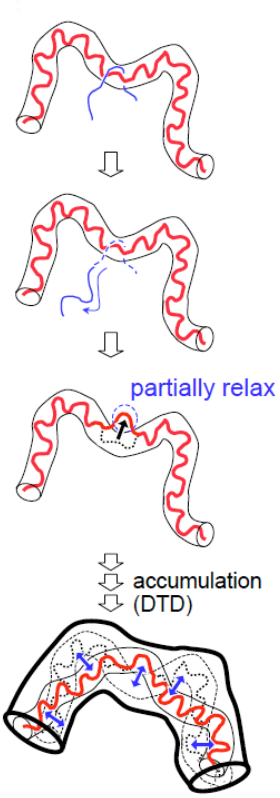

Fig. 2-7. Schematic illustration of CR/DTD of linear chain.

CR mechanism allows the tube model to describe/consider the motional correlation between the focused chain and the surrounding, tube-forming chains, though in a very crude way.

The CR process has been cast in the theory in three different but related ways. The double reptation (DR) theory, developed by Tsenoglou[20] and des Cloizeaux,[21] regards the entanglement as a binary interaction (binary hooking), thereby allowing the disentanglement on motion of one of the two entangling chains. Consequently, the relaxation modulus $G(t)$ deduced from the DR theory is given by $G(t) = G_N\{\varphi(t)\}^2$, where G_N is the entanglement plateau modulus and $\varphi(t)$ is the tube survival probability (calculated for the reptation process in the fixed tube in the simplest treatment[20]) .

As the second way (historically, at first), Graessley[18] described the CR process as a retarded Rouse process with its local relaxation frequency being determined by the large-scale motion (*e.g.*, reptation) of the tube forming chains, as depicted in the top three cartoons in Fig. 2-7. (Formulation of Rouse dynamics is summarized in Appendix 2B.) This CR-Rouse description is based on the idea that the local CR process is equivalent to flip of a freely jointed pair of rods (each having the length a). Large-scale conformational changes of a chain composed of freely-jointed N rods, resulting from accumulation of such local flips, are equivalent to the changes described by the Rouse theory with the local relaxation frequency being equivalent to the local flip frequency.[18]

As the third way, Marrucci[22] focused on this accumulation of local CR processes that

increases a length scale allowed for the chain motion in a direction lateral to the tube axis. As a result, the accumulation of local CR processes effectively dilates the tube diameter, as depicted in the bottom cartoon in Fig. 2-7. During this dynamic tube dilation (DTD) process, the chain is forced to move only along the dilated tube because the dilated tube diameter $a_{\mathrm{DTD}}(t)$ ($> a$) specifies the maximum length scale allowed for the lateral motion of the chain in a given time scale. Thus, the reptation process can be naturally/simply combined with the CR process if this molecular view of DTD is adopted.

Nevertheless, the DTD picture requires $a_{\mathrm{DTD}}(t)$ to be explicitly specified in terms of known molecular parameters. In the simplest view, the relaxed portion of the chains is assumed to behave as a "solvent", and only the unrelaxed portion having the fraction $\varphi'(t)$ (being identical to the survival probability of the dilated tube) is considered to constrain the chain motion. In this view, $\varphi'(t)$ is equivalent to a polymer concentration in an entangled solution, and the tube fully dilates to a diameter in this solution, $a_{\text{full-DTD}}(t) = a\{\varphi'(t)\}^{-d}$ with the dilation exponent d = 1-1.3.[22] Correspondingly, the number of dilated entanglement segments (enlarged stress sustaining units) having the size $a_{\text{full-DTD}}(t)$ at time t is smaller than the number of undilated segments (of the size a) by a factor of $\{\varphi'(t)\}^{d}$, and the normalized viscoelastic relaxation function $\mu(t) = G(t)/G_{\mathrm{N}}$ is simply expressed in terms of the survival probability of the dilated tube $\varphi'(t)$ as[22-24]

$$\mu_{\text{f-DTD}}(t) = \{\varphi'(t)\}^{1+d} \tag{2-18}$$

However, this full-DTD picture assumes that the chain can explore, *in time*, all local conformations within the length scale $a_{\text{full-DTD}}(t) = a\{\varphi'(t)\}^{-d}$. If the CR dynamics does not allow this exploration, the tube specifying the length scale of confinement for the chain motion dilates only partially to a diameter $a_{\text{partial-DTD}}(t) = a/\beta(t)$, where $\beta(t)$ is the maximum number of entanglement segments that can be CR-equilibrated in a given time scale of t.[25,26] The corresponding expression of the relaxation modulus is given by[25,26]

$$\mu_{\text{p-DTD}}(t) = \varphi'(t)/\beta(t) \tag{2-19}$$

For type-A chains having the dipoles parallel along the chain backbone, the survival fraction of the dilated tube $\varphi'(t)$ can be dielectrically evaluated ($\varphi'(t)$ essentially coincides with the normalized dielectric relaxation function $\Phi(t)$ defined in section 2-1).[25,26] In addition, $\beta(t)$ can be evaluated from the CR time data.[27] Thus, Eqs. 2-18 and 2-19 have been tested in a purely experimental way through comparison of the $\varphi'(t)$ and viscoelastic data:[25,26] It turned out that Eq. 2-18 is valid for monodisperse linear chains but fails for binary blends of linear chains, whereas Eq. 2-19 works for the blends. (An example of the test of Eqs. 2-18 and 2-19 is later shown in Chapter 5.)

2-3-2. *Tube models for star-branched chain at equilibrium*

The tube model has been extended to star-branched polymers. For star polymers composed of monodisperse linear arms being bound at their ends, reptation does not occur

because the branching point impedes the chain sliding. Instead, the retraction of each arm along the tube is considered to be the dominant mechanism of relaxation, as depicted in Fig. 2-8. This arm retraction is different from CLF of the linear chain (Fig. 2-6) because the full retraction of the arm is entropically unfavorable. CLF of the linear chain just considers shallow fluctuation of the chain length associated with no entropic penalty. Such shallow fluctuation occurs also for the star arm, but the full relaxation of the arm requires deep retraction back to the branching point and is associated with the entropic penalty.

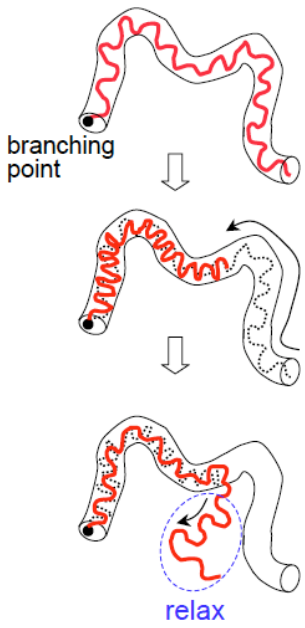

Fig. 2-8. Schematic illustration of arm retraction of star chain in a tube.

Doi and Kuzuu[28] first proposed a constitutive equation for star polymers on the basis of the deep arm retraction mechanism. Later, Pearson and Helfand[29] analyzed the arm retraction process as a first-passage time problem to obtain the linear relaxation modulus. The Doi-Kuzuu and Pearson-Helfand models considered no tube dilation, so that the relaxation time deduced from these models is orders of magnitude longer than the experiments if the entropic penalty for the arm retraction is faithfully calculated for Gaussian chains, as pointed out by Ball and McLeish.[30] For this problem, Ball and McLeish[30] refined the tube model by considering the dynamic tube dilation (DTD) mechanism that reduces the entropic penalty for the arm retraction. Milner and McLeish[23]

further refined the model by formulating the arm retraction process as the first passage process, incorporating the higher Rouse modes of the arm retraction, and considering the Colby–Rubinstein scaling[31] of the tube diameter for DTD. The full-DTD molecular picture explained in section 2-3-1 was adopted in both Ball-McLeish and Milner-McLeish models.

Modern tube models incorporating the arm retraction and DTD have achieved significant success to reproduce viscoelastic data.[1,2,23] Nevertheless, those model do not describe the dielectric data. Watanabe et al[32] considered the fluctuation at the dilated tube edge to derive the expression of the dielectric relaxation function for the Milner-McLeish model adopting the full-DTD picture.[23] They found that the model excellently describe the viscoelastic data of entangled star PI but the same model with the same parameter values does not consistently describe the dielectric data.[32] (Adjustment of the parameter values allows the model to describe the dielectric data, but then the model fails to describe the viscoelastic data.[32]) This problem is related to the very rapid CR-equilibration assumed in the full-DTD picture:[32] The star chains have intensive fast relaxation modes that significantly increase the dilated tube diameter $a_{\text{full-DTD}}$ considered in the full-DTD picture. However, actual CR process is not that fast, and the star arm cannot explore, in time, all local conformations within the length scale of $a_{\text{full-DTD}}$. For this reason, the full-DTD picture (and the model adopting this picture) is not valid for the star chain. Instead, the partial-DTD picture explicitly considering the length scale of CR-equilibration (cf. section 2-3-1) is valid for the star

chain.[32)]

2-3-3 *Tube models under fast and large deformations*

Although the theory under equilibrium has not yet been fully established as mentioned above, attempts have been made to describe polymer dynamics under fast and large deformations. Doi and Edwards[33)] assumed that the tube is affinely deformed, whereas the chain contracts along the tube to maintain the contour length. Although the Doi–Edwards model satisfactorily describe the magnitude of nonlinearity of entangled linear and/or star chains under large step shear deformations, it fails, even qualitatively, for the other types of flow/deformation.[1,2)] For example, the Doi-Edwards model predicts a decrease in the shear stress on an increase in the shear rate above the terminal viscoelastic relaxation frequency at equilibrium, $1/\tau_G(0)$. Such behavior is not observed in experiment, and thus, it is a flaw in the model that arises when the tube is over-oriented along the flow direction. Marrucci and Grizzuti[34)] extended the Doi-Edwards model to take into account the chain stretching. Their model (known as the DEMG model) resulted in improved predictions of the Doi-Edwards model for the transient response. Specifically, the DEMG model predicts an increase in the shear stress with an increase of the shear rate above the contraction rate (given as the Rouse relaxation frequency, $1/\tau_R$). However, if the flow rate is between $1/\tau_G(0)$ and $1/\tau_R$, the DEMG model gives a decrease in the shear stress because the chain stretching does not affect the tube

orientation.

An important ingredient to describe polymer dynamics under fast flow is the "convective constraint release" (CCR) mechanism proposed by Marrucci.[35] CCR results from contraction of a given chain convectively stretched by the shear, and this contraction leads to disentanglements of the surrounding chains thereby eliminating the over-orientation of the tube for those chains. Marrucci first proposed such a mechanism for a dumbbell model (without entanglement).[35] Later, Ianniruberto and Marrucci[36] incorporated CCR into the Doi-Edwards constitutive equation:[37] They assumed that the longest relaxation time decreases with increasing shear rate (because of the convective motion) irrespective of the other relaxation mechanisms. This decrease of the longest relaxation time is consistent with the viscoelastic data measured for small-amplitude oscillatory strain superposed on fast steady shear flow in parallel and/or orthogonal directions[11,12] (cf. Fig. 2-2), but it contradicts the flow insensitivity of dielectric response under fast shear flow[13] (cf. Fig. 2-3).

Several modified tube models have been formulated to implement all the mechanisms explained above (*i.e.,* reptation, CLF, CR/DTD, chain stretching, and CCR). Mead et al[38] elaborated on construction of such a model, known as the MLD model. This model is a full-chain model (also termed as contour-variable model) in which the subchain orientation and the chain stretching are dependent on their curvilinear position along the chain. Following Marrucci's idea, the MLD model considers that the longest relaxation time decreases due to

CCR (under the influence of flow-induced chain stretching).[38] Graham et al[39] proposed another full-chain model (GLaMM model) in which CCR is considered on the basis of molecular motion. They introduced Rouse dynamics of the tube (as in the formulation of CR at equilibrium) to express CCR under the assumption that the Rouse bead friction corresponds to the CCR rate.

The full-chain models are computationally demanding, and simplified versions (the so-called single segment models) have been developed, specifically for the use in computational fluid dynamics. Likhtman and Graham[40] proposed the Rolie–Poly model, a single mode version of the GLaMM model. Mead et al[38] replaced the chain by a dumbbell in the tube to formulate a simplified version of the MLD model. Marrucci and Ianniruberto[41] also proposed another single-segment model.

These modified tube models (full-chain models and single-segment models) are capable of predicting nonlinear viscoelastic behavior semi-quantitatively, but not yet examined for the relaxational quantities (cf. Figs. 2-2 and 2-3) under shear flow.

Appendix 2A: Formulation of reptation dynamics at equilibrium.[1,2]

Reptation is the coherent diffusive motion of the whole backbone of the chain along the tube axis, as depicted in Fig. 2-5. Thus, the bond vector of nth subchain at time t, $\mathbf{u}(n,t)$, obeys the time evolution equation at equilibrium,

$$\mathbf{u}(n,t+\Delta t) = \mathbf{u}(n+\Delta n,t) \tag{2-20}$$

where Δn indicates a stochastic displacement along the tube in an interval of time, Δt, being normalized by the tube diameter a. For the one-dimensional diffusive motion along the tube axis, Δn is related to Δt as

$$<\Delta n> = 0, \quad <\Delta n^2> = (2D_c/a^2)\Delta t \tag{2-21}$$

where D_c indicates the curvilinear diffusion coefficient of the chain. Specifically, for the chain composed of N entanglement segments each having the friction ζ_e, D_c is expressed in terms of N, ζ_e, Boltzmann constant k_B, and absolute temperature T, as

$$D_c = k_B T/N\zeta_e \tag{2-22}$$

Eq. 2-20 can be solved directly if Δn is modeled as a stochastic variable having the Gaussian distribution. However, usually, Eq. 2-20 is utilized to formulate a deterministic time evolution equation for a macroscopic quantity that can be solved with a standard method. For example, for the shear orientation function $S(n,t) = <u_x(n,t)u_y(n,t)/a^2>_\gamma$ (shear component of the orientation tensor **S** defined by Eq. 2-1b; under small strain, the factor gb^2 appearing in Eq. 2-1b is equal to the squared size of the entanglement segment, a^2), the time evolution equation is obtained as

$$\frac{\partial S(n,t)}{\partial t} = \frac{D_c}{a^2}\frac{\partial^2 S(n,t)}{\partial n^2} \tag{2-23}$$

The initial and boundary conditions for Eq. 2-23 are given by

$$S(n,0) = S_0 \text{ (uniform orientation along the chain backbone)} \tag{2-24}$$

$S(0,t) = S(N,t) = 0$ (no orientation at chain ends) (2-25)

With these conditions, Eq. 2-23 is solved to give

$$S(n,t) = S_0 \sum_{p=\text{odd}} \frac{4}{p\pi} \sin\left(\frac{p\pi n}{N}\right) \exp\left(-\frac{p^2 t}{\tau_{\text{rep}}}\right) \tag{2-26}$$

with

$$\tau_{\text{rep}} = \frac{a^2 N^2}{\pi^2 D_{\text{c}}} = \frac{\zeta_{\text{e}} a^2 N^3}{\pi^2 k_{\text{B}} T} \quad \text{(reptation time)} \tag{2-27}$$

From Eqs. 2-26 and 2-27, the relaxation modulus under small step strain, the basic relaxation function for the viscoelastic data, is obtained as

$$G(t) = \frac{3\nu k_{\text{B}} T}{\gamma} \int_0^N S(n,t)\, \text{d}n \;=\; G_{\text{N}} \sum_{p=\text{odd}} \frac{8}{p^2 \pi^2} \exp\left(-\frac{p^2 t}{\tau_{\text{rep}}}\right) \tag{2-28}$$

with

$$G_{\text{N}} \;= \frac{3\nu N k_{\text{B}} T}{\gamma} S_0 \quad \text{(entanglement modulus)} \tag{2-29}$$

In derivation of Eq. 2-28, the summation appearing in the stress expression (Eq. 2-1a) has been replaced by integral. $S_0 = \gamma/3$ and $G_{\text{N}} = \nu N k_{\text{B}} T$ for the affine deformation at $t = 0$, whereas $S_0 = 4\gamma/15$ and $G_{\text{N}} = 4\nu N k_{\text{B}} T/5$ after the local tension equilibration considered in the Doi-Edwards model.[1-3] However, this small difference of G_{N} is not important, in particular when the G_{N} data are utilized in Eq. 2-28.

The normalized dielectric relaxation function of type-A linear chain, $\Phi(t)$ defined by Eq. 2-5, is expressed in terms of the local correlation function $C(n,t;m)$:[1,8]

$$\Phi(t) = \frac{1}{N} \int_0^N C(n,t;m)\, \text{d}n\, \text{d}m \tag{2-30}$$

with

$$C(n,t;m) = \frac{1}{a^2} < \mathbf{u}(n,t) \bullet \mathbf{u}(m,0) >_{\mathrm{eq}} \tag{2.31}$$

From Eq. 2-20, the time evolution equation for $C(n,t;m)$ is obtained as

$$\frac{\partial C(n,t;m)}{\partial t} = \frac{D_{\mathrm{c}}}{a^2} \frac{\partial^2 C(n,t;m)}{\partial n^2} \tag{2-32}$$

The initial and boundary conditions are given by

$$C(n,0;m) = \delta(n-m) \quad \text{(Gaussian conformation at equilibrium)} \tag{2-33}$$

$$C(n,t;m) = 0 \text{ for } n, m = 0 \text{ and } N \text{ (no memory at chain ends)} \tag{2-34}$$

With these conditions, Eq. 2-32 is solved to give

$$C(n,t;m) = \frac{2}{N} \sum_{p} \sin\left(\frac{p\pi n}{N}\right) \sin\left(\frac{p\pi m}{N}\right) \exp\left(-\frac{p^2 t}{\tau_{\mathrm{rep}}}\right) \tag{2-35}$$

and

$$\Phi(t) = \sum_{p=\mathrm{odd}} \frac{8}{p^2 \pi^2} \exp\left(-\frac{p^2 t}{\tau_{\mathrm{rep}}}\right) \tag{2-36}$$

It should be noted that the normalized viscoelastic relaxation function $\mu(t) = G(t)/G_{\mathrm{N}}$ (Eq. 2-28) and normalized dielectric relaxation function $\Phi(t)$ are exactly the same for the reptation motion in the fixed (undilated) tube. In fact, the coincidence of $\mu(t)$ and $\Phi(t)$ is concluded whenever the tube is fixed, irrespective of the details of the chain motion (*e.g.*, even for the case of arm retraction of star chains).[8] Thus, the viscoelastic and dielectric data of type-A chains have been frequently compared to judge if the tube (or entanglement) is fixed in space.

Appendix 2B: Formulation of Rouse dynamics at equilibrium.[1,2)]

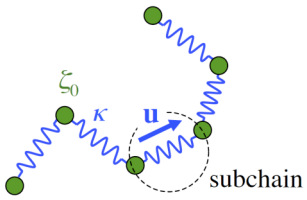

Fig. 2-9. Schematic illustration of Rouse chain.

In the Rouse theory, a chain is subdivided into N subchains, as depicted in Fig. 2-9. The entropy elasticity of each subchain is represented by a Hookean spring of the strength κ (= $3k_BT/a^2$ with a being the size of the subchain at equilibrium). The subchain friction ζ_0 is localized in a bead, and the neighboring beads are connected by the spring. Each bead is subjected to the elastic force from the neighboring beads (exerted by the springs), the frictional force due to the motion against a medium, and the thermal Brownian force. The inertia is neglected, so that the balance of these forces determines the motion of the Rouse chain (motion of the beads). In the continuous limit, the equation of motion (in the absence of flow at time t) is formulated for the end-to-end vector of the nth subchain at time t, $\mathbf{u}(n,t)$ (cf. Fig. 2-9), as[1,2)]

$$\zeta_0 \frac{\partial \mathbf{u}(n,t)}{\partial t} = \kappa \frac{\partial^2 \mathbf{u}(n,t)}{\partial n^2} + \frac{\partial \mathbf{F}_B(n,t)}{\partial n} \qquad (2\text{-}37)$$

Here, $\mathbf{F}_B(n,t)$ is the Brownian force acting on the nth bead at time t. $\mathbf{F}_B(n,t)$ is modeled as a white noise characterized by

$$\left\langle \mathbf{F}_B(n,t)\mathbf{F}_B(n',t') \right\rangle = 2\zeta_0 k_B T \delta(n-n')\delta(t-t')\mathbf{I} \qquad (2\text{-}38)$$

Here, $\mathbf{I}$ is the unit tensor.

Eq. 2-37 can be explicitly and easily solved with a method of eigenmode expansion. However, it is more convenient to formulate a time evolution equation for a macroscopic

quantity of interest (as was the case also for the reptation calculation; cf. Appendix 2A). For calculation of the relaxation modulus $G(t)$ for the Rouse dynamics, it is convenient to focus on a cross-correlation function defined by

$$S_2(n,m,t) \equiv (1/a^2) < u_x(n,t)u_y(m,t) >_\gamma \tag{2-39}$$

where the ensemble average $< \cdots >_\gamma$ is made under a small step shear strain γ. From Eqs. 2-37 and 2-38, the time evolution equation for $S_2(n,m,t)$ is formulated as

$$\zeta_0 \frac{\partial S_2(n,m,t)}{\partial t} = \kappa \left\{ \frac{\partial^2}{\partial n^2} + \frac{\partial^2}{\partial m^2} \right\} S_2(n,m,t) \tag{2-40}$$

The initial and boundary conditions are given by

$$S_2(n,m,0) = (\gamma/3)\delta(n-m) \quad \text{(no cross-correlation at } t = 0) \tag{2-41}$$

$$S_2(n,m,0) = 0 \text{ for } n, m = 0 \text{ and } N \text{ (no orientation at chain ends)} \tag{2-42}$$

(The affine deformation is assumed in Eq. 2-41.) For these conditions, Eq. 2-40 gives

$$S_2(n,m,t) = \frac{2\gamma}{3N} \sum_p \sin\left(\frac{p\pi n}{N}\right) \sin\left(\frac{p\pi m}{N}\right) \exp\left(-\frac{p^2 t}{\tau_R^{[G]}}\right) \tag{2-43}$$

with

$$\tau_R^{[G]} = \frac{\zeta_0 N^2}{2\kappa\pi^2} = \frac{\zeta_0 a^2 N^2}{6\pi^2 k_B T} \quad \text{(longest viscoelastic relaxation time)} \tag{2-44}$$

Consequently, the relaxation modulus is obtained as (cf. Eq. 2-1a)

$$G(t) = \frac{3\nu k_B T}{\gamma} \int_0^N S_2(n,n,t)\, dn = \nu k_B T \sum_p \exp\left(-\frac{p^2 t}{\tau_R^{[G]}}\right) \tag{2-45}$$

(In derivation of Eq. 2-45, the summation appearing in Eq. 2-1a has been replaced by integral.)

The basic correlation function for the dielectric relaxation is the local correlation function $C(n,t;m) \equiv \frac{1}{a^2} < \mathbf{u}(n,t) \bullet \mathbf{u}(m,0) >_{\mathrm{eq}}$ (cf. Eq. 2-31). For this function, the time evolution equation can be easily found from Eqs. 2-37 and 2-38 as

$$\zeta_0 \frac{\partial C(n,t;m)}{\partial t} = \kappa \frac{\partial^2 C(n,t;m)}{\partial n^2} \tag{2-46}$$

With the initial and boundary conditions given by Eqs. 2-33 and 2-34, respectively, Eq. 2-46 is easily solved to give

$$C(n,t;m) = \frac{2}{N} \sum_p \sin\left(\frac{p\pi n}{N}\right) \sin\left(\frac{p\pi m}{N}\right) \exp\left(-\frac{p^2 t}{\tau_{\mathrm{R}}^{[\varepsilon]}}\right) \tag{2-47}$$

with

$$\tau_{\mathrm{R}}^{[\varepsilon]} = \frac{\zeta_0 N^2}{\kappa \pi^2} = \frac{\zeta_0 a^2 N^2}{3\pi^2 k_{\mathrm{B}} T} \quad \text{(longest dielectric relaxation time)} \tag{2-48}$$

Consequently, the normalized dielectric relaxation function is obtained as (cf. Eq. 2-30)

$$\Phi(t) = \sum_{p=\mathrm{odd}} \frac{8}{p^2 \pi^2} \exp\left(-\frac{p^2 t}{\tau_{\mathrm{R}}^{[\varepsilon]}}\right) \tag{2-49}$$

It should be noted that the Rouse dynamics gives quite different relaxation mode distribution for the viscoelastic $G(t)$ (Eq. 2-45) and dielectric $\Phi(t)$ (Eqs. 2-49). The relaxation time is different as well ($\tau_{\mathrm{R}}^{[\varepsilon]}$ for the dielectric relaxation is twice of $\tau_{\mathrm{R}}^{[G]}$ for the viscoelastic relaxation; cf. Eqs. 2-44 and 2-48). These features of Rouse dynamics is quite different from those of reptation dynamics, which in turn demonstrates that comparison of viscoelastic and dielectric data for type-A chains is crucial for investigation of the details of the chain motion. In particular, for the constraint release (CR) mechanism modeled as the

retarded Rouse process, $G(t)$ and $\Phi(t)$ are given by Eqs. 2-45 and 2-49 with $\tau_R^{[G]}$ and $\tau_R^{[\varepsilon]}$ therein being replaced by the viscoelastic and dielectric longest CR times, $\tau_{CR}^{[G]}$ and $\tau_{CR}^{[\varepsilon]}$ $(= 2\tau_{CR}^{[G]})$.

References

1) H. Watanabe, Progress in Polymer Science, 24, 1253 (1999).

2) T. C. B. McLeish, Advances in Physics, 51, 1379 (2002).

3) M. Doi, S. F. Edwards, The Theory of Polymer Dynamics, (Clarendon Press, Oxford, 1986).

4) H. Janeschitz-Kriegl, Polymer melt rheology and flow birefringence, (Springer, Berlin, 1983).

5) T. Inoue, H. Okamoto, K. Osaki, Macromolecules, 24, 5670 (1991).

6) H. Okamoto, T. Inoue, K. Osaki, Journal of Polymer Science Part B: Polymer Physics, 33, 417 (1995).

7) E. Riande, Dipole Moments and Birefringence of Polymers, (Prentice Hall, Englewood, NJ, 1992).

8) H. Watanabe, Macromolecular Rapid Communications, 22, 127 (2001).

9) R. J. Cole, The Journal of Chemical Physics, 42, 637 (1965).

10) W. H. Stockmayer, Pure and Applied Chemistry, 15, 539 (1967).

11) J. Vermant, L. Walker, P. Moldenears, and J. Mewis, Journal of Non-Newtonian Fluid Mechanics, 79, 173 (1998).

12) E. Somma, O. Valentino, G. Titomanlio, and G. Ianniruberto, Journal of Rheology, 51, 987 (2007).

13) H. Watanabe, S. Ishida, and Y. Matsumiya, Macromolecules, 35, 8802 (2002).

14) H. Watanabe, Y. Matsumiya, K. Horio, Y. Masubuchi, and T. Uneyama, "Rheo-Dielectric Behavior of Soft Matters", in Non-Equilibrium Soft Matter Physics, vol.4, edited by S. Komura and T. Ohta, World Scientific, Singapore, 2012, Chapter 2 (pp 37-87).

15) D. Evans and P. Morris, Statistical Mechanics of Nonequilibrium Liquids, (Academic Press, London, 1990).

16) S. F. Edwards, Proceedings of the Physical Society, 92, 9 (1967).

17) P. G. de Gennes, The Journal of Chemical Physics, 55, 572 (1971).

18) W. W. Graessley, Advances in Polymer Science, 47, 67 (1982).

19) M. Doi, Journal of Polymer Science: Polymer Physics Edition, 21, 667 (1983).

20) C. Tsenoglou, ACS Polymer Preprints, 28, 185 (1987).

21) J. des Cloizeaux, Europhysics Letters, 5, 437 (1988).

22) G. Marrucci, Journal of Polymer Science: Polymer Physics Edition 23, 159 (1985).

23) S. T. Milner and T. C. B. McLeish, Macromolecules 30, 2159 (1997).

24) S. T. Milner and T. C. B. McLeish, Physical Review Letters, 81, 725 (1998).

25) H. Watanabe, S. Ishida, Y. Matsumiya, and T. Inoue, Macromolecules, 37, 1937 (2004).

26) H. Watanabe, S. Ishida, Y. Matsumiya, and T. Inoue, Macromolecules, 37, 6619 (2004).

27) T. Sawada, X. Qiao, and H. Watanabe, Nihon Reoroji Gakkaishi (Journal of the Society of Rheology, Japan), 35, 11 (2007).

28) M. Doi and N. Kuzuu, Journal of Polymer Science: Polymer Letters Edition, 18, 775 (1980).

29) D. S. Pearson and E. Helfand, Macromolecules, 17, 888 (1984).

30) R. C. Ball and T. C. B. McLeish, Macromolecules, 22, 1911 (1989).

31) R. H. Colby and M. Rubinstein, Macromolecules, 23, 2753 (1990).

32) H. Watanabe, Y. Matsumiya and T. Inoue, Macromolecules, 35, 2339 (2002).

33) M. Doi and S. F. Edwards, Journal of the Chemical Society, Faraday Transactions 2, 74, 1802. (1978).

34) G. Marrucci and N. Grizzuti, Gazzetta Chimica Italiana, 118, 179 (1988).

35) G. Marrucci, Journal of Non-Newtonian Fluid Mechanics 62, 279 (1996).

36) G. Ianniruberto and G. Marrucci, Journal of Non-Newtonian Fluid Mechanics, 65, 241 (1996).

37) M. Doi and S. F. Edwards, Journal of the Chemical Society, Faraday Transactions 2, 74, 1818 (1978).

38) D. W. Mead, R. G. Larson and M. Doi, Macromolecules, 31, 7895 (1998).

39) R. S. Graham, A. E. Likhtman, T. C. B. McLeish and S. T. Milner, Journal of Rheology, 47, 1171 (2003).

40) A. E. Likhtman and R. S. Graham, Journal of Non-Newtonian Fluid Mechanics, 114, 1 (2003)

41) G. Marrucci and G. Ianniruberto, Philosophical transactions. Series A, Mathematical, physical, and engineering sciences, 361(1805), 677 (2003).

Chapter 3. Expression of Dielectric Relaxation Function under Steady Shear and LAOS

3-1. Introduction

Cis-polyisoprene chains have the type-A dipoles parallel along the chain backbone. Thus, their large-scale motion is detected as both viscoelastic and dielectric relaxation processes in long time scales, as explained in Chapters 1 and 2. In the linear response regime (at equilibrium), the normalized viscoelastic and dielectric relaxation functions $\mu(t)$ (= $G(t)/G_N$) and $\Phi(t)$ are unequivocally related to the chain conformation through Eqs. 2-1, 2-5, and 2-6. In the nonlinear regime under fast flow/large deformation, Eq. 2-1 giving $\mu(t)$ is still valid as long as the chains are not highly stretched and the stress-optical rule is valid.[1,2] However, Eqs. 2-5 and 2-6 giving $\Phi(t)$ are not necessarily valid under fast flow/large deformation, because the underlying Green-Kubo theorem[3,4] does not hold rigorously in such nonlinear regime. Thus, it is necessary to examine if Eqs. 2-5 and 2-6 are satisfactorily valid in the nonlinear regime. For this purpose, this chapter makes analysis on the basis of Langevin equation for linear type-A chains under steady shear. A simple calculation is made also for the rheo-dielectric response under large amplitude oscillatory strain (LAOS).

3-2. Formulation of Dielectric Response under Fast Steady Shear

An ensemble of linear type-A chains each being composed of N+1 subchains is

considered. The steady shear is applied in x direction, and a weak, constant electric field E is applied at time $t \geq 0$ in the direction of the shear gradient (y direction), as shown in Fig. 3-1. The total dipole of the chain is expressed as $mR_y(t)$, where m is the magnitude of dipole *per* unit length of the chain backbone and $R_y(t)$ is the y component of the end-to-end vector of the chain. Thus, the unnormalized dielectric relaxation function is expressed as

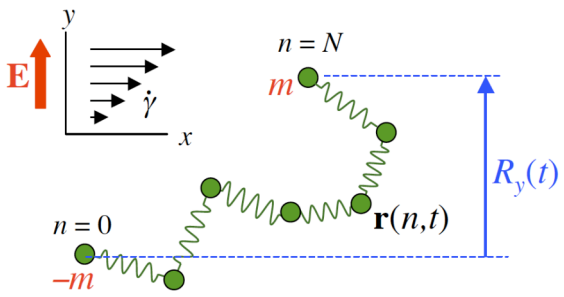

Fig. 3-1. Schematic illustration of chain under steady shear and electric field

$$\Phi_{ss}^{un}(t;\dot{\gamma}) = \frac{\nu m}{E}\left\{\left\langle R_y(\infty)\right\rangle_{ss,E} - \left\langle R_y(t)\right\rangle_{ss,E}\right\} \tag{3-1}$$

where ν is the number density of the chain, and the average $\langle\cdots\rangle_{ss,E}$ is taken for the chains under steady shear in the presence of the electric field. The end-to-end vector fluctuation under steady shear in the absence of the electric field is described by an auto-correlation function,

$$\Psi_{ss}(t;\dot{\gamma}) = \left\langle R_y(t)R_y(0)\right\rangle_{ss,E=0} \tag{3-2}$$

If the shear rate $\dot{\gamma}$ is sufficiently small, the Green-Kubo theorem works to guarantee the proportionality between $\Phi_{ss}^{un}(t;\dot{\gamma})$ and $\Psi_{ss}(t;\dot{\gamma})$. However, under fast shear, this theorem is not rigorously valid. The relationship between $\Phi_{ss}^{un}(t;\dot{\gamma})$ and $\Psi_{ss}(t;\dot{\gamma})$ for such cases needs to be analyzed on the basis of the chain motion described by a Langevin equation.

The type-A chain under the electric field is equivalent to a totally neutral chain having negative and positive charges $-m$ and m at zero-th and Nth subchains, as depicted in Fig. 3-1.

Thus, the electric force acting on nth subchain can be expressed as

$$\mathbf{F}^{\mathrm{E}}(n,t) = \begin{bmatrix} 0 \\ mE\{\delta(n-N) - \delta(n)\} \\ 0 \end{bmatrix} \tag{3-3}$$

The chain motion is determined by a balance of the frictional force, intra- and inter-chain potential forces (such as the thermal tension along the chain backbone and the excluded volume force, the latter resulting from the uncrossability of chains and raising the entanglement effect for long chains), the Brownian force, and this $\mathbf{F}^{\mathrm{E}}(n,t)$. The time evolution of the position $\mathbf{r}(n,t)$ of nth subchain is described by a Langevin equation representing this force balance. Within the mean-field treatment where the interactions of a given chain with the surrounding chains are pre-averaged, this equation can be cast in a rather general form,

$$-\zeta\left\{\dot{\mathbf{r}}(n,t) - \dot{\Gamma}\bullet\mathbf{r}(n,t)\right\} + \mathbf{\Lambda}(n;\dot{\gamma})\bullet\mathbf{r}(n,t) + \mathbf{F}^{\mathrm{B}}(n,t) + \mathbf{F}^{\mathrm{E}}(n,t) = \mathbf{0} \tag{3-4}$$

with

$$\dot{\Gamma} = \begin{bmatrix} 0 & \dot{\gamma} & 0 \\ 0 & 0 & 0 \\ 0 & 0 & 0 \end{bmatrix} \quad \text{(shear rate tensor)} \tag{3-5}$$

In Eq. 3-4, ζ is the subchain friction coefficient, and $\mathbf{F}^{\mathrm{B}}(n,t)$ is the stochastic Brownian force that can be safely assumed to have a white-noise character, $\left\langle \mathbf{F}^{\mathrm{B}}(n,t)\mathbf{F}^{\mathrm{B}}(n',t')\right\rangle = 2\mathbf{I}\zeta k_{\mathrm{B}}T\delta(n-n')\delta(t-t')$ with $\mathbf{I}$ = unit tensor. In general, $\mathbf{\Lambda}(n;\dot{\gamma})$ is a 3-dimensional tensorial operator with respect to n (having components $\Lambda_{\alpha\beta}$ with α, $\beta = x$, y, and z) and may explicitly depend on the shear rate $\dot{\gamma}$. This $\mathbf{\Lambda}$, giving the potential forces for a given chain

conformation $\mathbf{r}(n,t)$ thereby governing the chain motion, is determined by an effective Hamiltonian of the chain under steady shear. In general, the chain motion can be decomposed into eigenmodes. For such cases, $\boldsymbol{\Lambda}$ is considered to be a linear operator within the framework of the mean-field treatment, *i.e.*, $\boldsymbol{\Lambda}\bullet(\mathbf{r}+\mathbf{r}') = \boldsymbol{\Lambda}\bullet\mathbf{r} + \boldsymbol{\Lambda}\bullet\mathbf{r}'$.

From this consideration, the position $\mathbf{r}(n,t)$ can be expanded with respect to the Rouse eigenfunctions, $\cos(p\pi n/N)$ with $p = 0, 1, 2, ..,$ as

$$\mathbf{r}(n,t) = \sum_{p\geq 0} \begin{bmatrix} X_p(t) \\ Y_p(t) \\ Z_p(t) \end{bmatrix} \cos\left(\frac{p\pi n}{N}\right) \tag{3-6}$$

The Rouse eigenfunctions are not necessarily the eigenfunctions of the chain motion determined by $\boldsymbol{\Lambda}$ but are chosen as the base functions for easy calculation. From Eqs. 3-3, 3-4, and 3-5, the unnormalized dielectric relaxation function, $\Phi_{ss}^{un}(t;\dot{\gamma})$ (Eq. 3-1), and the end-to-end vector auto-correlation function, $\Psi_{ss}(t;\dot{\gamma})$ (Eq. 3-2), both being defined in the shear gradient direction, can be calculated with a standard method explained in Appendix 3A. The results are summarized as

$$\Phi_{ss}^{un}(t;\dot{\gamma}) = \frac{2m^2\nu}{N\zeta} \sum_{\beta\geq 1} g_\beta^{[\Phi]} \exp\left(-\lambda_\beta t\right) \tag{3-7a}$$

with

$$g_\beta^{[\Phi]} = \frac{1}{\lambda_\beta} \left\{ \sum_{p\geq 1} (\cos p\pi - 1)\ Q_{3p-1,\beta} \right\} \left\{ \sum_{p'\geq 1} (\cos p'\pi - 1)\ Q^{-1}_{\beta,3p'-1} \right\} \tag{3-7b}$$

and

$$\Psi_{ss}(t;\dot{\gamma}) = \frac{2k_B T}{N\zeta} \sum_{\beta \geq 1} g_{\beta}^{[\Psi]} \exp\left(-\lambda_{\beta} t\right) \tag{3-8a}$$

with

$$g_{\beta}^{[\Psi]} = \sum_{\beta' \geq 1} \frac{2}{\lambda_{\beta} + \lambda_{\beta'}} \left\{ \sum_{\alpha \geq 1} Q_{\beta,\alpha}^{-1} Q_{\beta',\alpha}^{-1} \right\} \times \left\{ \sum_{p \geq 1} (\cos p\pi - 1)\, Q_{3p-1,\beta} \right\} \left\{ \sum_{p' \geq 1} (\cos p'\pi - 1)\, Q_{\beta',3p'-1}^{-1} \right\} \tag{3-8b}$$

The parameters λ_{β}, $Q_{i,j}$, and $Q_{i,j}^{-1}$ appearing in Eqs. 3-7 and 3-8, being dependent on $\dot{\gamma}$ in principle, are related to an infinite matrix **A** having the components,

$$\begin{aligned} &A_{3p-2,3q-2} = a_{p,q}^{xx}, \quad A_{3p-2,3q-1} = a_{p,q}^{xy} + \zeta\dot{\gamma}, \quad A_{3p-2,3q} = a_{p,q}^{xz}, \\ &A_{3p-1,3q-2} = a_{p,q}^{yx}, \quad A_{3p-1,3q-1} = a_{p,q}^{yy}, \quad A_{3p-2,3q} = a_{p,q}^{yz}, \\ &A_{3p,3q-2} = a_{p,q}^{zx}, \quad A_{3p,3q-1} = a_{p,q}^{zy}, \quad A_{3p,3q} = a_{p,q}^{zz} \quad (p, q = 1, 2, ...) \end{aligned} \tag{3-9}$$

Here, $a_{i,j}^{\alpha\beta}$ (i, j = 1, 2, ..; α, β = x, y, z) are the expansion coefficients of the Rouse eigenfunction defined with respect to the $\alpha\beta$ component of the operator, $\Lambda_{\alpha\beta}$, as

$$\Lambda_{\alpha\beta}(n;\dot{\gamma}) \cos\left(\frac{j\pi n}{N}\right) = \sum_{i \geq 1} a_{i,j}^{\alpha\beta} \cos\left(\frac{i\pi n}{N}\right) \quad (i, j = 1, 2, ..) \tag{3-10}$$

(Equivalently, $a_{i,j}^{\alpha\beta} = (2/N) \int_0^N \mathrm{d}n \cos(i\pi n/N) \{\Lambda_{\alpha\beta} \cos(j\pi n/N)\}$.) The parameter λ_{β} is the βth eigenvalue of the matrix **A** divided by ζ, $Q_{i,j}$ is the i,j component of a matrix **Q** that diagonalizes **A**, and $Q_{i,j}^{-1}$ is the i,j component of the inverse matrix $\mathbf{Q}^{-1}$; namely, $\{\mathbf{Q}^{-1}\mathbf{A}\mathbf{Q}\}_{\alpha\beta} = -\zeta\lambda_{\beta}\delta_{\alpha\beta}$ with $\delta_{\alpha\beta}$ being Kronecker delta.

Eqs. 3-7a and 3-8a indicate that the dielectric relaxation function $\Phi_{ss}^{un}(t;\dot{\gamma})$ and the end-to-end vector auto-correlation function $\Psi_{ss}(t;\dot{\gamma})$ have the same relaxation rates of the modes, λ_{β}. Namely, in rather general cases where Eq. 3-4 is valid, the dielectric and

fluctuation modes have the same relaxation times $1/\lambda_\beta$ under steady shear. Thus, the terminal relaxation time of the *end-to-end vector fluctuation* can be rigorously evaluated as the terminal *dielectric relaxation* time, even under the steady shear.

As for the mode distribution of $\Phi_{ss}^{un}(t;\dot{\gamma})$ and $\Psi_{ss}(t;\dot{\gamma})$, it should be noted that the operator $\mathbf{\Lambda}$ is determined by the effective Hamiltonian, so that the coefficient $a_{p,q}^{\alpha\beta}$ appearing in Eqs. 3-9 and 3-10 is invariant on exchange of α and β, *e.g.*, $a_{p,q}^{xy} = a_{p,q}^{yx}$. Thus, the matrix $\mathbf{A}$ is symmetric *at equilibrium* (*i.e.*, $A_{ij} = A_{ji}$ in Eq. 3-9 with $\dot{\gamma} \to 0$), and the diagonalizing matrix $\mathbf{Q}$ is orthogonal for this case ($\mathbf{Q}^{-1} = \mathbf{Q}^{+}$ with $\mathbf{Q}^{+}$ = transpose matrix of $\mathbf{Q}$). Then, the term appearing in eq. 3-8b, $\Sigma_{\alpha\geq 1} Q_{\beta,\alpha}^{-1} Q_{\beta',\alpha}^{-1}$, reduces to $\delta_{\beta\beta'}$ (cf. $\Sigma_{\alpha\geq 1} Q_{\beta,\alpha}^{-1} Q_{\beta',\alpha}^{-1} = \Sigma_{\alpha\geq 1} Q_{\beta,\alpha}^{-1} Q_{\alpha,\beta'}$ for this case) so that the mode intensities $g_\beta^{[\Phi]}$ (Eq. 3-7b) and $g_\beta^{[\Psi]}$ (Eq. 3-8b) exactly coincide with each other. Since Φ^{un} and Ψ have the same relaxation times $1/\lambda_\beta$, this coincidence of g means that Φ^{un} and Ψ are rigorously proportional to each other and satisfy a relationship $\Phi^{un}(t) = \{m^2\nu/k_B T\}\Psi(t)$ at any t. This fact confirms the validity of the Green-Kubo theorem at equilibrium.

Under steady shear, the symmetry of $\mathbf{A}$ breaks because of the $\zeta\dot{\gamma}$ term contributing to the component $A_{3p-2,3q-1}$; cf. Eq. 3-9. For a case that the dynamics in the y and z directions are not coupled with that in the x direction, *i.e.*, for the case of $a_{p,q}^{yx} = a_{p,q}^{zx} = 0$, $A_{3p-1,3q-2}$ and $A_{3p,3q-2}$ vanishes and a subset of $\mathbf{A}$ specifying the dynamics in the y and z directions remains symmetric even under steady shear. For this case, $g_\beta^{[\Phi]}$ and $g_\beta^{[\Psi]}$ exactly coincide with

each other so that the Green-Kubo theorem is rigorously valid for Φ_{ss}^{un} and Ψ_{ss}. However, in a more general case where $A_{3p-1,3q-2} \neq 0$, the exact coincidence of g vanishes and the dielectric mode distribution measured under steady shear does not rigorously agree with the fluctuation mode distribution under the same condition. Nevertheless, even for this general case, an argument related to the shear symmetry can specify the dielectric mode distribution, as discussed below.

Obviously, the relaxation rate λ_β as well as $\Phi_{ss}^{un}(t;\dot{\gamma})$ and $\Psi_{ss}(t;\dot{\gamma})$ are invariant on inversion of the shear direction and thus even functions of $\dot{\gamma}$. Then, these quantities can be expanded as

$$\lambda_\beta(\dot{\gamma}) = \lambda_\beta^{(0)} + \dot{\gamma}^2\lambda_\beta^{(2)} + O(\dot{\gamma}^4) \tag{3-11a}$$

$$\Phi_{ss}^{un}(t;\dot{\gamma}) = \Phi^{un(0)}(t) + \dot{\gamma}^2\Phi_{ss}^{un(2)}(t) + O(\dot{\gamma}^4;t) \tag{3-11b}$$

$$\Psi_{ss}(t;\dot{\gamma}) = \Psi^{(0)}(t) + \dot{\gamma}^2\Psi_{ss}^{(2)}(t) + O(\dot{\gamma}^4;t) \tag{3-11c}$$

where the superscript "(0)" denotes the quantities at equilibrium ($\dot{\gamma} \to 0$), the subscript "(2)" stands for the second-order expansion coefficients of respective quantities, and $O(\dot{\gamma}^4)$ and $O(\dot{\gamma}^4;t)$ represent quantities of the order of $\dot{\gamma}^4$ (or higher) Some details of these coefficients can be examined with the aid of two types of correlation functions, $S_{yx}(n,n',t) \equiv \langle u_y(n,t)u_x(n',0)\rangle$ and $S_{yy}(n,n',t) \equiv \langle u_y(n,t)u_y(n',0)\rangle$, defined with respect to the y and x components of the bond vector of the subchain $\mathbf{u}(n,t)$ ($=\partial\mathbf{r}(n,t)/\partial n$) under steady shear. Clearly, $S_{yx}(n,n',t)$ changes its sign on inversion of the shear direction while $S_{yy}(n,n',t)$ is

invariant to this inversion, meaning that $S_{yx}(n,n',t)$ and $S_{yy}(n,n',t)$, respectively, are odd and even functions of $\dot{\gamma}$. From analysis of the perturbation coefficients of $S_{yx}(n,n',t)$ and $S_{yy}(n,n',t)$ as well as $\Phi_{ss}^{un}(t;\dot{\gamma})$ and $\Psi_{ss}(t;\dot{\gamma})$ on the basis of this shear symmetry, the validity of the Green-Kubo theorem (proportionality between $\Phi_{ss}^{un}(t;\dot{\gamma})$, and $\Psi_{ss}(t;\dot{\gamma})$) is deduced at least up to the order of $\dot{\gamma}^2$, as explained in Appendix 3B.

Apart from the above argument, Eq. 3-11 suggests that λ_β, Φ_{ss}^{un} and Ψ_{ss} are affected by the steady shear to the same order of $\dot{\gamma}$. Thus, in a semi-quantitative sense, the shear effect is expected to be insignificant for any two of λ_β, Φ_{ss}^{un}, Ψ_{ss} if the remaining one is not significantly affected by the shear in the range of $\dot{\gamma}$ examined. Experiments[5,6] indicated that the terminal dielectric relaxation time τ_ε of entangled linear PI chains, being identical to the terminal time for the end-to-end vector fluctuation (cf. Eqs. 3-7a and 3-8a), is quite insensitive to the shear rate $\dot{\gamma}$ in a range of $\dot{\gamma} < 30/\tau_\varepsilon^o$, with τ_ε^o being τ_ε at equilibrium (cf. Fig. 2-3 in Chapter 2). This fact means that the $\dot{\gamma}^2$-order term for λ_β (Eq. 3-11a) is actually negligible compared to the $\dot{\gamma}^0$-order term at those $\dot{\gamma}$. Thus, this should be the case also for Φ_{ss}^{un} (Eq. 3-11b) and Ψ_{ss} (Eq. 3-11c) of linear PI at $\dot{\gamma} < 30/\tau_\varepsilon^o$ and these Φ_{ss}^{un} and Ψ_{ss} should be satisfactorily approximated by the equilibrium functions.

From the above arguments, the Green-Kubo theorem should be valid at least up to the order of $\dot{\gamma}^2$ and, more importantly, in the range of $\dot{\gamma}$ actually examined for PI. Thus, the time evolution of the polarization under steady shear (in the shear gradient direction), P_{ss}(t),

can be satisfactorily described by an equation formally identical to the equation deduced from the Green-Kubo theorem at equilibrium,

$$P_{ss}(t) = -\frac{\nu m^2}{k_B T}\left\langle R_y^2 \right\rangle_{ss} \int_{-\infty}^{t} ds\, E(s)\, \frac{\partial \Phi_{ss}(t-s)}{\partial t} \tag{3-12}$$

with the normalized dielectric relaxation function $\Phi_{ss}(t)$ (= 1 at $t = 0$) being given by

$$\Phi_{ss}(t) = \frac{\left\langle R_y(t) R_y(0) \right\rangle_{ss}}{\left\langle R_y{}^2 \right\rangle_{ss}} \tag{3-13}$$

The corresponding dielectric intensity under steady shear, $\Delta\varepsilon_{ss}$, is written as

$$\Delta\varepsilon_{ss} = F\left(\frac{4\pi m^2}{k_B T}\right) \nu \left\langle R_y^2 \right\rangle_{ss} \tag{3-14}$$

In Eq. 3-14, the correction factor for the internal electric field, F, and the pre-factor of 4π (in MKSA units) have been introduced.

3-3. Literature Data and Simulation under Fast Steady Shear

The Green-Kubo theorem is satisfactorily valid under steady shear (at $\dot{\gamma} < 30/\tau_\varepsilon^{\circ}$), as explained in the previous section. However, this validity does *not* mean that the chain dynamics remains close to that at equilibrium. In fact, significant nonlinearities observed for viscoelastic quantities indicate that the chain dynamics under fast steady shear is far from that at equilibrium. As an example, unfilled symbols in Fig. 3-2 show data of the steady state viscosity η, the terminal dielectric relaxation time τ_ε ($\cong 1/\lambda_1$), and $\Delta\varepsilon_{ss}$ reported for an entangled PI solution with the molecular weight $M_{PI} = 1.2\times10^6$ and concentration $C_{PI} = 15$

wt% (in an oligomeric solvent).[6] These data are normalized by respective values at equilibrium and plotted against the normalized shear rate $\dot{\gamma}\tau_\varepsilon^\circ$. The dielectric τ_ε and $\Delta\varepsilon_{ss}$ data, related to the end-to-end vector fluctuation, are hardly dependent on $\dot{\gamma}$ ($< 30/\tau_\varepsilon^\circ$), whereas η strongly decreases with increasing $\dot{\gamma}$. Thus, the chains at those $\dot{\gamma}$ are in the prominently non-equilibrium state to exhibit the significant thinning of the viscosity, together with the $\dot{\gamma}$-insensitive dielectric behavior.

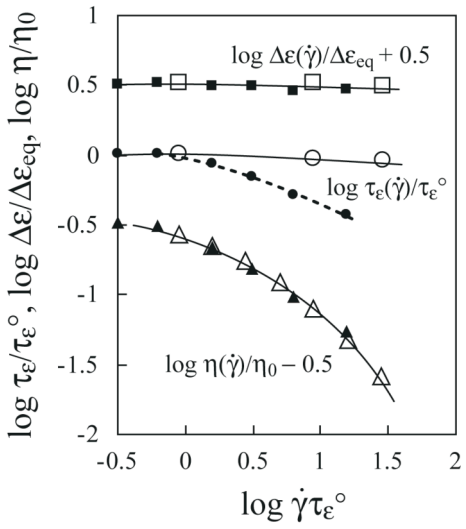

Fig. 3-2. Dielectric relaxation time $\tau_\varepsilon(\dot{\gamma})$, dielectric relaxation intensity $\Delta\varepsilon(\dot{\gamma})$, and the viscosity $\eta(\dot{\gamma})$ measured at 30°C for an entangled PI solution (in oligomeric butadiene; $M_{PI} = 1.2\times10^6$ and C_{PI} = 15 wt% for PI) under fast steady shear.[6] Filled symbols indicate the normalized $\tau_\varepsilon(\dot{\gamma})$, $\Delta\varepsilon(\dot{\gamma})$, $\eta(\dot{\gamma})$ obtained from the NAPLES simulation (cf. Appendix 3C).

The above results, in particular the general coincidence of the dielectric and end-to-end fluctuation relaxation times $1/\lambda_\beta$ (cf. Eqs. 3-7a and 3-8a), verify the expression of $\Phi_{ss}(t)$ (Eq. 3-13). This $\Phi_{ss}(t)$ decays monotonically with t and can be generally expressed as a sum of exponential terms, as similar to $\Phi(t)$ at equilibrium (cf. Eq. 2-14). Thus, the polarization $P_{ss}(t)$ (Eq. 3-12) against the oscillatory electric field, $E(t) = E_0 \sin \omega t$ (with $E_0 << 1$), oscillates with t only at the angular frequency ω of this field (cf. Eq. 2-10). Because of this feature, the rheo-dielectric behavior under steady shear is *fully* characterized with $\varepsilon'(\omega)$ and $\varepsilon''(\omega)$

that are related to $\Phi_{ss}(t)$ and $\Delta\varepsilon_{ss}$ through Eq. 2-12. It should be emphasized that the situation is different under LAOS, as explained in the next section.

In relation to the above verification, it is informative to examine results of a preliminary molecular simulation (NAPLES simulation) reported in literature.[7] The simulation was based on the primitive chain network model,[8] and positive and negative charges (m and $-m$; cf. Fig. 3-1) were placed at the chain ends.[7] In the simulation, a weak electric field was applied to an ensemble of the type-A chains and the macroscopic polarization $P_{ss}(t)$ due to this field was directly evaluated from the spatial distribution of the chain ends. The resulting macroscopic dielectric relaxation function was found to agree well with $\Phi_{ss}(t)$ defined by Eq. 3-13, lending support to the argument presented in the previous section.

The NAPLES simulation has been conducted also in this study, with the calculated results being statistically averaged for more chains and over a longer time scale compared to those in literature.[7] Details of the simulation is described in Appendix 3C. The simulation mimics the behavior of entangled linear PI considerably well, as shown with the filled symbols in Fig. 3-2. Although the simulated $\tau_\varepsilon(\dot{\gamma})$ decreases with $\dot{\gamma}$ more rapidly than the experimental $\tau_\varepsilon(\dot{\gamma})$ data and the dynamics considered in the simulation needs to be refined, a difference of the nonlinearities for $\tau_\varepsilon(\dot{\gamma})$ and $\eta(\dot{\gamma})$ (stronger for the latter) is qualitatively captured by the simulation.

3-4. Dielectric signal from PI under LAOS

3-4-1. *Green-Kubo analysis.*

The dielectric response of entangled linear PI chains under large amplitude oscillatory strain (LAOS) has been examined experimentally.[9,10] However, no analysis has been made for the fundamental molecular expression of the rheo-dielectric response under LAOS. Thus, this analysis is attempted in the remaining part of this Chapter.

In principle, the validity of the Green-Kubo theorem under LAOS needs to be examined at first through the Langevin analysis similar to that under the steady shear explained in the previous section. However, the analysis becomes much more complicated under LAOS because the shear rate tensor (cf. Eq. 3-5) oscillates with time for this case. Nevertheless, the Green-Kubo theorem is satisfactorily valid for PI under steady shear in a range of $\dot{\gamma} < 30/\tau_{\varepsilon}^{\circ}$, which suggests that the theorem should be also valid under LAOS to same level of accuracy, as long as the shear rate $\dot{\gamma}$ under LAOS stays in a similar range. Then, the analysis of the rheo-dielectric response under LAOS can be started with the Green-Kubo expression of polarization,[3,4,11]

$$P_{\mathrm{LAOS}}(t) = \frac{m^2}{k_{\mathrm{B}}T}\int_{-\infty}^{t} \mathrm{d}s\, E(s) \times \int \mathrm{d}\mathbf{p}\, \mathrm{d}\mathbf{q} \left\{ \{\Sigma_j R_{y,j}(t)\} \frac{\mathrm{d}}{\mathrm{d}s}\left\{\Sigma_j R_{y,j}(s)\right\}\right\} f_{\mathrm{LAOS}}(\mathbf{p},\mathbf{q},s) \tag{3-15}$$

Here, $E(s)$ represents a weak electric field at time s being superposed on the LAOS field, and $f_{\mathrm{LAOS}}(\mathbf{p},\mathbf{q},s)$ is the conformational distribution function in the phase space (with $\mathbf{p}$ and $\mathbf{q}$ being

the generalized momentum and coordinate) at time s under LAOS. This f_{LAOS} is defined in the absence of the electric field (which is a consequence of the Green-Kubo theorem).

For the rheo-dielectric response under *steady* shear, Eq. 3-15 is valid but $f_{\mathrm{LAOS}}(\mathbf{p},\mathbf{q},s)$ therein is replaced by a s-independent distribution function. For this case, Eq. 3-15 straightforwardly gives Eqs. 3-12 and 3-13. In contrast, under LAOS at an angular frequency Ω, $\gamma(t) = \gamma_0 \sin(\Omega t + \delta_0)$ with δ_0 being the phase difference from the electric field at time 0, $f_{\mathrm{LAOS}}(\mathbf{p},\mathbf{q},s)$ should be synchronized with LAOS to oscillate at the LAOS frequency Ω with some phase difference, $\delta(\Omega)$. ($\delta(\Omega)$ is not necessarily identical to δ_0.) In the simplest case, this $f_{\mathrm{LAOS}}(\mathbf{p},\mathbf{q},s)$ can be written in a form

$$f_{\mathrm{LAOS}}(\mathbf{p},\mathbf{q},s) = \frac{K^{\mathrm{base}}(\mathbf{p},\mathbf{q}) + K^{\mathrm{osc}}(\mathbf{p},\mathbf{q})\sin(\Omega s + \delta)}{I^{\mathrm{base}} + I^{\mathrm{osc}}\sin(\Omega s + \delta)} \tag{3-16}$$

Here, $K^{\mathrm{base}}(\mathbf{p},\mathbf{q})$ and $K^{\mathrm{osc}}(\mathbf{p},\mathbf{q})$ indicates the stationary (base) part of $f_{\mathrm{LAOS}}(\mathbf{p},\mathbf{q},s)$ and an amplitude of the oscillatory part, and I^{base} and I^{osc} are given by the following integrals.

$$I^{\mathrm{base}} = \int \mathrm{d}\mathbf{p}\,\mathrm{d}\mathbf{q}\,K^{\mathrm{base}}(\mathbf{p},\mathbf{q}),\quad I^{\mathrm{osc}} = \int \mathrm{d}\mathbf{p}\,\mathrm{d}\mathbf{q}\,K^{\mathrm{osc}}(\mathbf{p},\mathbf{q}) \tag{3-17}$$

The factor appearing in the denominator of Eq. 3-16, $I^{\mathrm{base}} + I^{\mathrm{osc}}\sin(\Omega s + \delta)$, guarantees the normalization condition, $\int \mathrm{d}\mathbf{p}\,\mathrm{d}\mathbf{q}\; f_{\mathrm{LAOS}}(\mathbf{p},\mathbf{q},s) = 1$ at any s.

If the LAOS effect on $f_{\mathrm{LAOS}}(\mathbf{p},\mathbf{q},s)$ is rather mild to give a ratio $r = I^{\mathrm{osc}}/I^{\mathrm{base}}$ being smaller than unity, Eq. 3-16 can be expanded as

$$f_{\mathrm{LAOS}}(\mathbf{p},\mathbf{q},s) = \left\{\frac{K^{\mathrm{base}}(\mathbf{p},\mathbf{q})}{I^{\mathrm{base}}} + \frac{K^{\mathrm{osc}}(\mathbf{p},\mathbf{q})}{I^{\mathrm{osc}}} r\sin(\Omega s + \delta)\right\} \times \sum_{\alpha \geq 0} (-r)^{\alpha} \sin^{\alpha}(\Omega s + \delta) \tag{3-18}$$

From Eqs. 3-15 and 3-18, P_{LAOS} is expressed as

$$P_{\mathrm{LAOS}}(t) = \frac{\nu m^2}{k_{\mathrm{B}}T}\int_{-\infty}^{t} \mathrm{d}s\, E(s) \left\{ \frac{\partial \Psi^{\mathrm{base}}(t,s)}{\partial \mathrm{s}} + \frac{\partial \Psi^{\mathrm{osc}}(t,s)}{\partial \mathrm{s}} r \sin(\Omega s + \delta) \right\} \times \sum_{\alpha \geq 0} (-r)^{\alpha} \sin^{\alpha}(\Omega s + \delta) \tag{3-19}$$

Here, ν is the chain number density, and $\Psi^{\mathrm{base}}(t,s)$ and $\Psi^{\mathrm{osc}}(t,s)$ denote correlation functions defined by

$$\Psi^{\mathrm{base}}(t,s) \equiv \left\langle R_y(t) R_y(s) \right\rangle_{\mathrm{LAOS}}^{\mathrm{base}} = \frac{\int \mathrm{d}\boldsymbol{p}\, \mathrm{d}\boldsymbol{q}\, \{R_y(t) R_y(s)\}\, K^{\mathrm{base}}(\boldsymbol{p},\boldsymbol{q})}{\int \mathrm{d}\boldsymbol{p}\, \mathrm{d}\boldsymbol{q}\, K^{\mathrm{base}}(\boldsymbol{p},\boldsymbol{q})} \tag{3-20a}$$

$$\Psi^{\mathrm{osc}}(t,s) \equiv \left\langle R_y(t) R_y(s) \right\rangle_{\mathrm{LAOS}}^{\mathrm{osc}} = \frac{\int \mathrm{d}\boldsymbol{p}\, \mathrm{d}\boldsymbol{q}\, \{R_y(t) R_y(s)\}\, K^{\mathrm{osc}}(\boldsymbol{p},\boldsymbol{q})}{\int \mathrm{d}\boldsymbol{p}\, \mathrm{d}\boldsymbol{q}\, K^{\mathrm{osc}}(\boldsymbol{p},\boldsymbol{q})} \tag{3-20b}$$

A stationary state, where a correlation of quantities at times t and s ($< t$) is dependent only on a time interval $t-s$, is not attained under LAOS because of the oscillation of f_{LAOS}, in particular when the time interval is shorter than the LAOS period, $2\pi/\Omega$. Thus, in a rigorous sense, both $\Psi^{\mathrm{base}}(t,s)$ and $\Psi^{\mathrm{osc}}(t,s)$ depend on t and s separately. However, the correlation of the chain conformation at two times t and s should decay, in general, on an increase of the interval $t-s$ beyond the LAOS period, in particular when the LAOS effect on f_{LAOS} is rather mild. Then, for examination of the slow dynamics, $\Psi^{\mathrm{base}}(t,s)$ and $\Psi^{\mathrm{osc}}(t,s)$ can be approximated as functions of $t-s$:

$$\Psi^{\mathrm{base}} \cong \Psi^{\mathrm{base}}(t-s) = \left\langle R_y(t-s) R_y(0) \right\rangle_{\mathrm{LAOS}}^{\mathrm{base}} = \left\langle R_y^2 \right\rangle_{\mathrm{LAOS}}^{\mathrm{base}} \sum_{\alpha \geq 1} h_{\mathrm{base},\alpha} \exp\left\{ -\frac{(t-s)}{\tau_{\mathrm{base},\alpha}} \right\} \tag{3-21a}$$

$$\Psi^{\rm osc} \cong \Psi^{\rm osc}(t-s) = \left\langle R_y(t-s)R_y(0)\right\rangle^{\rm osc}_{\rm LAOS}$$

$$= \left\langle R_y^2\right\rangle^{\rm osc}_{\rm LAOS} \sum_{\alpha\geq 1} h_{{\rm osc},\alpha} \exp\left\{-\frac{(t-s)}{\tau_{{\rm osc},\alpha}}\right\} \tag{3-21b}$$

with

$$\sum_{\alpha\geq 1} h_{{\rm base},\alpha} = \sum_{\alpha\geq 1} h_{{\rm osc},\alpha} = 1 \tag{3-22}$$

and

$$\left\langle R_y^2\right\rangle^{\rm base}_{\rm LAOS} = \frac{\int {\rm d}\mathbf{p}\,{\rm d}\mathbf{q}\, R_y^2\, K^{\rm base}(\mathbf{p},\mathbf{q})}{\int {\rm d}\mathbf{p}\,{\rm d}\mathbf{q}\, K^{\rm base}(\mathbf{p},\mathbf{q})}, \quad \left\langle R_y^2\right\rangle^{\rm osc}_{\rm LAOS} = \frac{\int {\rm d}\mathbf{p}\,{\rm d}\mathbf{q}\, R_y^2\, K^{\rm osc}(\mathbf{p},\mathbf{q})}{\int {\rm d}\mathbf{p}\,{\rm d}\mathbf{q}\, K^{\rm osc}(\mathbf{p},\mathbf{q})} \tag{3-23}$$

In Eq. 3-21, the correlation functions $\Psi^{\xi}(t-s)$ (ξ = base, osc) are factorized into an intensity part, $\left\langle R_y^2\right\rangle^{\xi}_{\rm LAOS}$, and a normalized time-dependent part, $\Sigma_\alpha h_{\xi,\alpha} \exp\{-(t-s)/\tau_{\xi,\alpha}\}$ (= 1 at $s = t$).

Substitution of Eq. 3-21 into Eq. 3-19 gives the final expression of $P_{\rm LAOS}(t)$ and/or the relaxational current $I_{\rm relax}(t) = {\rm d}P_{\rm LAOS}(t)/{\rm d}t$. Some characteristic features in this final expression are summarized below.

3-4-2. *Rheo-dielectric response for a constant electric field superposed on LAOS.*

For $E(s) = E$ (time-independent electric field), $I_{\rm relax}(t)$ obtained from Eqs. 3-19 and 3-21 is expressed as

$$I_{\rm relax}(t) = I^{[1]}_{\rm relax}(t) + I^{[2]}_{\rm relax}(t) \tag{3-24a}$$

with

$$I_{\text{relax}}^{[1]}(t) = -\frac{\nu m^2 E}{k_B T}\left[\frac{d\Psi^{\text{base}}(t)}{dt} + \left(\frac{d\Psi^{\text{base}}(t)}{dt} - \frac{d\Psi^{\text{osc}}(t)}{dt}\right)\sum_{\alpha\geq 1}(-r)^{\alpha} sin^{\alpha}\delta\right] \quad (3\text{-}24b)$$

and

$$I_{\text{relax}}^{[2]}(t) = -\frac{\nu m^2 E\Omega}{k_B T}\int_0^t ds'\left(\frac{d\Psi^{\text{base}}(s')}{ds'} - \frac{d\Psi^{\text{osc}}(s')}{ds'}\right)\times$$

$$\sum_{\alpha\geq 1}\alpha(-r)^{\alpha}\sin^{\alpha-1}\{\Omega(t-s')+\delta\}\cos\{\Omega(t-s')+\delta\} \quad (3\text{-}24c)$$

Eq. 3-24 indicates that $I_{\text{relax}}(t)$ under LAOS oscillates around its average that monotonically decays with t, $I_{\text{relax}}^{\text{ave}}(t) \equiv (\Omega/2\pi)\int_{t-\pi/\Omega}^{t+\pi/\Omega} I_{\text{relax}}(t')\,dt'$. This oscillation is contributed from $I_{\text{relax}}^{[2]}(t)$, and $I_{\text{relax}}^{\text{ave}}(t)$, from both $I_{\text{relax}}^{[1]}(t)$ and $I_{\text{relax}}^{[2]}(t)$. In principle, the oscillation includes all orders of LAOS harmonics having the angular frequencies Ω, 2Ω, 3Ω, …, as easily noted from Eq. 3-24c. However, for the case of mild LAOS effect on f_{LAOS}, the magnitude of this effect should be essentially determined by the invariance of the strain tensor and thus the leading term of this effect should scale as γ^2. For this reason, the main component of oscillation of $I_{\text{relax}}(t)$ due to the mild LAOS effect should be the oscillation of $\gamma^2 = \gamma_0^2 \sin^2 \Omega t = (\gamma_0^2/2)(1-\cos 2\Omega t)$ that occurs at the angular frequency 2Ω, or, the period time of π/Ω.

3-4-3. *Rheo-dielectric response for a sinusoidal electric field superposed on LAOS.*

For a sinusoidal electric field $E(s) = E_0 \sin \omega s$ superposed on LAOS, Eqs. 3-19 and 3-21 give

$$\frac{k_B T}{\nu m^2 E_0} P_{\mathrm{LAOS}}(t) = \left\langle R_y^2 \right\rangle_{\mathrm{LAOS}}^{\mathrm{base}} \left\{ \left(\sum_{\alpha \geq 1} h_{\mathrm{base},\alpha} \frac{1}{1+\omega^2 \tau_{\mathrm{base},\alpha}^2} \right) \sin \omega t - \left(\sum_{\alpha \geq 1} h_{\mathrm{base},\alpha} \frac{\omega \tau_{\mathrm{base},\alpha}}{1+\omega^2 \tau_{\mathrm{base},\alpha}^2} \right) \cos \omega t \right\}$$

$$- \left\langle R_y^2 \right\rangle_{\mathrm{LAOS}}^{\mathrm{base}} \frac{r}{2} \left\{ S_-^{\mathrm{base}}(\omega,\Omega) \sin(\omega-\Omega)t + C_-^{\mathrm{base}}(\omega,\Omega) \cos(\omega-\Omega)t \right\}$$

$$+ \left\langle R_y^2 \right\rangle_{\mathrm{LAOS}}^{\mathrm{base}} \frac{r}{2} \left\{ S_+^{\mathrm{base}}(\omega,\Omega) \sin(\omega+\Omega)t + C_+^{\mathrm{base}}(\omega,\Omega) \cos(\omega+\Omega)t \right\}$$

$$+ \left\langle R_y^2 \right\rangle_{\mathrm{LAOS}}^{\mathrm{osc}} \frac{r}{2} \left\{ S_-^{\mathrm{osc}}(\omega,\Omega) \sin(\omega-\Omega)t + C_-^{\mathrm{osc}}(\omega,\Omega) \cos(\omega-\Omega)t \right\}$$

$$- \left\langle R_y^2 \right\rangle_{\mathrm{LAOS}}^{\mathrm{osc}} \frac{r}{2} \left\{ S_+^{\mathrm{osc}}(\omega,\Omega) \sin(\omega+\Omega)t + C_+^{\mathrm{osc}}(\omega,\Omega) \cos(\omega+\Omega)t \right\}$$

$$+ O(r^\beta \sin(\omega \pm \beta\Omega); \beta \geq 2) \qquad (3\text{-}25)$$

with

$$S_-^\xi(\omega,\Omega) = \sum_{\alpha \geq 1} g_{\xi,\alpha} \frac{(\omega-\Omega)\tau_{\xi,\alpha} \cos\delta + \sin\delta}{1+(\omega-\Omega)^2 \tau_{\xi,\alpha}^2}, \quad C_-^\xi(\omega,\Omega) = \sum_{\alpha \geq 1} g_{\xi,\alpha} \frac{\cos\delta - (\omega-\Omega)\tau_{\xi,\alpha} \sin\delta}{1+(\omega-\Omega)^2 \tau_{\xi,\alpha}^2}$$

$$S_+^\xi(\omega,\Omega) = \sum_{\alpha \geq 1} g_{\xi,\alpha} \frac{(\omega+\Omega)\tau_{\xi,\alpha} \cos\delta - \sin\delta}{1+(\omega+\Omega)^2 \tau_{\xi,\alpha}^2}, \quad C_+^\xi(\omega,\Omega) = \sum_{\alpha \geq 1} g_{\xi,\alpha} \frac{\cos\delta + (\omega+\Omega)\tau_{\xi,\alpha} \sin\delta}{1+(\omega+\Omega)^2 \tau_{\xi,\alpha}^2}$$

(ξ = base, osc) (3-26)

Namely, $P_{\mathrm{LAOS}}(t)$ for the sinusoidal electric field splits into a series of components oscillating at the angular frequency of the electric field ω and at $\omega \pm \beta\Omega$ with β = 1, 2, ..., as clearly noted from Eq. 3-25. The components oscillating at $\omega \pm \beta\Omega$ emerge because of the interference between the sinusoidal electric and LAOS fields. This interference makes a contrast between the rheo-dielectric responses under LAOS and steady shear: As explained earlier, the response under steady shear oscillates only at the frequency of the electric field ω (and is more easily analyzed compared to that under LAOS) because the distribution function under steady shear is independent of time.

The information for the correlation function $\Psi^{\mathrm{base}}(t)$ under LAOS, *i.e.*, the mode

distribution $\{h_{\text{base},\alpha}, \tau_{\text{base},\alpha}\}$ and the intensity $\left\langle R_y^2 \right\rangle_{\text{LAOS}}^{\text{base}}$ (Eqs. 3-21a and 3-23), is included in the component of $P_{\text{LAOS}}(t)$ oscillating at ω, as can be easily noted in the first line in Eq. 3-25. On the other hand, the information for $\Psi^{\text{osc}}(t)$, $\{h_{\text{osc},,\alpha}, \tau_{\text{osc},\alpha}\}$ and $\left\langle R_y^2 \right\rangle_{\text{LAOS}}^{\text{osc}}$ (Eqs. 3-21b and 3-23), is included in the components oscillating at $\omega \pm \beta\Omega$ (β = 1, 2, …); cf. coefficients S and C given by Eq. 3-26. Namely, the full information for the chain dynamics under LAOS, being represented by a set of $\Psi^{\text{base}}(t)$ and $\Psi^{\text{osc}}(t)$, can be obtained only when the magnitudes of all these components are measured. However, in the rheo-dielectric studies under LAOS conducted so far,[9,10] only the component oscillating at ω was measured and converted to $\varepsilon_{\text{LAOS}}'(\omega)$ and $\varepsilon_{\text{LAOS}}''(\omega)$. Thus, the full information for the chain dynamics under LAOS was not obtained in those studies.

Nevertheless, it is still informative to examine the molecular consequence of the $\varepsilon_{\text{LAOS}}''(\omega)$ data in literature.[9,10] The second term in the first line of Eq. 3-25, gives

$$\varepsilon_{\text{LAOS}}''(\omega) = \Delta\varepsilon_{\text{LAOS}} \sum_{\alpha \geq 1} h_{\text{base},\alpha} \frac{\omega\tau_{\text{base},\alpha}}{1+\omega^2\tau_{\text{base},\alpha}^2} \tag{3-27}$$

with

$$\Delta\varepsilon_{\text{LAOS}} = F\left(\frac{4\pi m^2}{k_{\text{B}}T}\right) \nu \left\langle R_y^2 \right\rangle_{\text{LAOS}}^{\text{base}} \tag{3-28}$$

(In Eq. 3-28, F is a correction factor for a difference between the macroscopic and internal electric field intensities, and the pre-factor of 4π converts the dielectric intensity into MKSA units; cf. Eq. 3-14.) For well entangled linear PI, Höfl et al[9] and Capaccioli et al[10] reported that the ω dependence of the $\varepsilon_{\text{LAOS}}''(\omega)$ data (*i.e.*, relative dielectric mode distribution)

hardly changes under LAOS. This fact suggests that the mode distribution and terminal relaxation time of the unnormalized correlation function, $\Psi^{base}(t)$, are insensitive to LAOS. This result appears to be in harmony with the shear-rate insensitivity of the rheo-dielectric data of PI measured under steady shear (cf. Figs. 2-3 and 3-2).

For further examination of this insensitivity, the NAPLES simulation was conducted in this study for type-A chains (9.6 entanglements per chain on average) under the LAOS condition, as explained in Appendix 3C. The LAOS frequency, Ω, was set at $3/\tau_\varepsilon^o$ with τ_ε^o being the terminal dielectric relaxation time at equilibrium, which mimics the experimental condition by Höfl et al.[9] Each chain is polarized to have small charges m and $-m$ at its ends, as explained in the previous section. In the simulation, the macroscopic polarization and the corresponding $\varepsilon_{LAOS}''(\omega)$ were directly evaluated from the spatial distribution of the chain ends (distribution of these charges) without utilizing any correlation function. In Fig. 3-3, this $\varepsilon_{LAOS}''(\omega)$ is normalized by the dielectric intensity at equilibrium, $\Delta\varepsilon_{eq}$, and double-logarithmically plotted against the normalized frequency of the electric field, $\omega\tau_\varepsilon^o$. The simulated dielectric relaxation time $\tau_\varepsilon^o(\gamma_0;\Omega)$ (~ reciprocal of the peak frequency) decreases with increasing LAOS amplitude γ_0. Experiments indicated no significant decrease of $\tau_\varepsilon(\gamma_0;\Omega)$ with γ_0, which suggests necessity of refining the chain dynamics considered in the simulation. Nevertheless, the simulated dielectric mode distribution (seen as the shape of the ε_{LAOS}'' curve in the double-logarithmic plot) is not significantly affected

by LAOS, which is in harmony with the experiments.[9,10)]

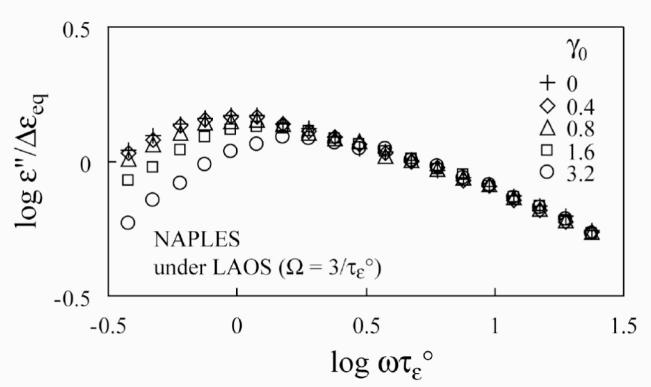

Fig. 3-3. Dielectric loss ε'' of entangled PI (9.6 entanglements per chain on average) under LAOS obtained from the NAPLES simulation; cf. Appendix 3c. The LAOS condition, γ_0 ($\leq$ 3.2) and Ω ($= 3/\tau_\varepsilon^\circ$), is similar to the experimental condition utilized by Höfl et al.[9)]

Höfl and coworkers[9)] also reported that the rheo-dielectric intensity $\Delta\varepsilon_{\mathrm{LAOS}}$ of well entangled bulk PI ($M_{\mathrm{PI}} = 55\times10^3$; ~ 10 entanglements per chain) decreased rather significantly with increasing γ_0. Specifically, at the LAOS angular frequency $\Omega \cong 3/\tau_\varepsilon^\circ$, $\Delta\varepsilon_{\mathrm{LAOS}}$ decreased by a factor of $\cong$ 30% with increasing LAOS amplitude to $\gamma_0 = 1.6$.[9)] (A decrease of $\Delta\varepsilon_{\mathrm{LAOS}}$, though weaker in magnitude, was also reported by Capaccioli et al.[10)]) This decrease is qualitatively captured by the NAPLES simulation shown in Fig. 3-3.

On the basis of Eq. 3-23, this decrease of $\Delta\varepsilon_{\mathrm{LAOS}}$ may appear to result from a decrease of the *average size* of a PI chain in the shear gradient direction. However, this assignment is not valid because the squared average of the chain size, $\left\langle R_y^2 \right\rangle_{\mathrm{LAOS}}$, is correctly defined as an average of R_y^2 over the distribution function $f_{\mathrm{LAOS}}(\mathbf{p},\mathbf{q},s)$ during one cycle of LAOS (for a time period of $2\pi/\Omega$), not as the average $\left\langle R_y^2 \right\rangle_{\mathrm{LAOS}}^{\mathrm{base}}$ defined just with respect to the

non-oscillatory component of this function, $K^{\text{base}}(\mathbf{p},\mathbf{q})$ (Eq. 3-23). From Eq. 3-16 together with a mathematical formula, $\int_0^{\pi} \mathrm{d}x \, \{1+\alpha\cos x\}^{-1} = \pi/\sqrt{1-\alpha^2}$ $(0 < \alpha < 1)$, $\left\langle R_y^2 \right\rangle_{\text{LAOS}}$ is obtained as

$$\begin{aligned} \left\langle R_y^2 \right\rangle_{\text{LAOS}} &\equiv \frac{\Omega}{2\pi}\int_0^{2\pi/\Omega} \mathrm{d}s \int \mathrm{d}\mathbf{p}\, d\mathbf{q}\, R_y^2 f_{\text{LAOS}}(\mathbf{p},\mathbf{q},s) \\ &= \left\langle R_y^2 \right\rangle_{\text{LAOS}}^{\text{base}} \left\{ \frac{1-\theta}{\sqrt{1-r^2}} \right\} + \left\langle R_y^2 \right\rangle_{\text{LAOS}}^{\text{osc}} \end{aligned} \tag{3-29}$$

with

$$\theta = \frac{\left\langle R_y^2 \right\rangle_{\text{LAOS}}^{\text{osc}}}{\left\langle R_y^2 \right\rangle_{\text{LAOS}}^{\text{base}}} \quad \text{and} \quad r = \frac{I^{\text{osc}}}{I^{\text{base}}} \;\; (0 < r < 1) \tag{3-30}$$

In general, the oscillatory component of the distribution function, $K^{\text{osc}}(\mathbf{p},\mathbf{q})$, would give a stronger rheo-dielectric effect and thus r $\left(= \left\{\int \mathrm{d}\mathbf{p}\, \mathrm{d}\mathbf{q}\, K^{\text{osc}}(\mathbf{p},\mathbf{q})\right\} / \left\{\int \mathrm{d}\mathbf{p}\, \mathrm{d}\mathbf{q}\, K^{\text{base}}(\mathbf{p},\mathbf{q})\right\}\right)$ would increase with increasing γ_0. On this increase of r, $\left\langle R_y^2 \right\rangle_{\text{LAOS}}$ would become considerably larger than $\left\langle R_y^2 \right\rangle_{\text{LAOS}}^{\text{base}}$ (cf. Eq. 3-29), suggesting that the decrease of $\Delta\varepsilon_{\text{LAOS}}$ $\left(\propto \left\langle R_y^2 \right\rangle_{\text{LAOS}}^{\text{base}}\right)$ is not equivalent to a decrease of $\left\langle R_y^2 \right\rangle_{\text{LAOS}}$.

The above difference between $\left\langle R_y^2 \right\rangle_{\text{LAOS}}$ and $\left\langle R_y^2 \right\rangle_{\text{LAOS}}^{\text{base}}$ can be further examined from the NAPLES simulation (cf. Appendix 3C) under the LAOS condition mimicking the experiment.[9] The simulation straightforwardly gave $\left\langle R_y^2 \right\rangle_{\text{LAOS}}$ as the squared end-to-end distance of the chain in the shear gradient direction averaged over many chains during one cycle of LAOS. It also gave the $\left\langle R_y^2 \right\rangle_{\text{LAOS}}^{\text{base}} / \left\langle R_y^2 \right\rangle_{\text{eq}}$ ratio as a ratio of the dielectric intensity $\Delta\varepsilon_{\text{LAOS}}$ under LAOS to $\Delta\varepsilon_{\text{eq}}$ at equilibrium. In Fig. 3-4, the $\left\langle R_y^2 \right\rangle_{\text{LAOS}} / \left\langle R_y^2 \right\rangle_{\text{eq}}$ and $\left\langle R_y^2 \right\rangle_{\text{LAOS}}^{\text{base}} / \left\langle R_y^2 \right\rangle_{\text{eq}}$ ratios are plotted against the LAOS amplitude, γ_0. Clearly, the

$\left\langle R_y^2 \right\rangle_{\mathrm{LAOS}}^{\mathrm{base}} / \left\langle R_y^2 \right\rangle_{\mathrm{eq}}$ ratio (squares) decreases considerably with increasing γ_0 to 3.2 but the $\left\langle R_y^2 \right\rangle_{\mathrm{LAOS}} / \left\langle R_y^2 \right\rangle_{\mathrm{eq}}$ ratio (circles) decreases less significantly. This result is in harmony with the above argument.

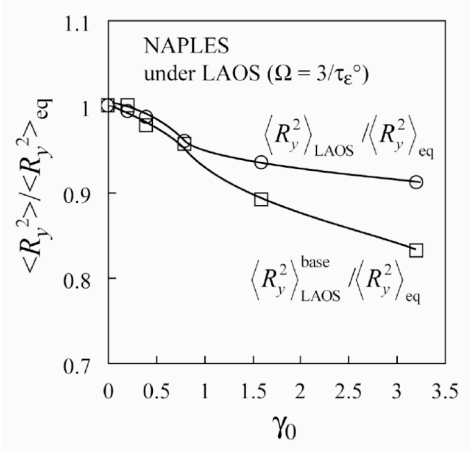

Fig. 3-4. $\left\langle R_y^2 \right\rangle_{\mathrm{LAOS}} / \left\langle R_y^2 \right\rangle_{\mathrm{eq}}$ and $\left\langle R_y^2 \right\rangle_{\mathrm{LAOS}}^{\mathrm{base}} / \left\langle R_y^2 \right\rangle_{\mathrm{eq}}$ ratios obtained from the NAPLES simulation for entangled PI (9.6 entanglements per chain on average) under LAOS; cf. Appendix 3C. The LAOS condition, γ_0 (≤ 3.2) and Ω ($= 3/\tau_\varepsilon^\circ$), is similar to the experimental condition utilized by Höfl et al.[9)]

3-5. Conclusion

This chapter has examined the molecular expression of rheo-dielectric response of PI having type-A dipoles. Up to a fairly high shear rate where rheological nonlinearity is clearly noted, the rheo-dielectric response under *steady shear* can be satisfactorily expressed as the end-to-end vector auto-correlation (in particular when the dielectric relaxation time is not much affected by the shear). Consequently, the rheo-dielectric intensity at those shear rates is proportional to the mean-square chain size in the shear gradient direction, $\left\langle R_y^2 \right\rangle$ (= average over the time-independent conformational distribution function).

In contrast, under large amplitude oscillatory strain $\gamma = \gamma_0 \sin \Omega t$ (LAOS), the distribution function f_{LAOS} is coupled with the LAOS field to oscillate with time, and the rheo-dielectric response detects this oscillation of f_{LAOS}. Thus, the response against a constant electric field exhibits an oscillatory decay (with the dominant oscillation period of π/Ω). The response against the sinusoidal electric field splits into a series of components oscillating at ω and $\omega \pm \beta\Omega$ (β = 1, 2, …), where ω is the angular frequency of electric field. The rheo-dielectric intensity under LAOS, evaluated from the component oscillating at ω, is no longer proportional to $\left\langle R_y^2 \right\rangle$.

Appendix 3A: Solution of Langevin Equation

The Langevin equation describing the time evolution of the subchain position $\mathbf{r}(n,t)$, Eq. 3-4 in the main text, can be rewritten as a series of time evolution equations for the amplitudes of the Rouse eigenmodes, $\{X_p(t), Y_p(t), Z_p(t)\}$ with $p \geq 0$, defined by Eq. 3-6 in the main text. Because of the independence of the internal motion of the chain and the center of mass motion, this series of equations can be compactly expressed with the use of extended amplitudes $\boldsymbol{\xi}$ having the components $\xi_{3p-2}(t) = X_p(t)$, $\xi_{3p-1}(t) = Y_p(t)$, and $\xi_{3p}(t) = Z_p(t)$ ($p \geq 1$):

$$\zeta \frac{\mathrm{d}}{\mathrm{d}t} \boldsymbol{\xi}(t) = \mathbf{A} \bullet \boldsymbol{\xi}(t) + \mathbf{B}(t) + \mathbf{D} \tag{3-31}$$

Here, ζ is the subchain friction coefficient, and $\mathbf{A}$ is the matrix defined by Eqs. 3-9 and 3-10 in the main text. $\mathbf{B}$ is a vector with its components being defined as the Fourier components

of the Brownian force in the α direction, $F_{B,\alpha}(n,t)$ ($\alpha = x, y, z$):

$$B_j(t) = \frac{2}{N}\int_0^N \mathrm{d}n\, F_{B,\alpha}(n,t)\, \cos\left(\frac{p\pi n}{N}\right)$$

with $j = 3p-2$, $3p-1$, and $3p$ for $\alpha = x$, y, and z, respectively (3-32)

D is a vector composed of Fourier components of the electrical force $\mathbf{F}^{\mathrm{E}}$ (cf. Eq. 3-3),

$$D_j = 0 \text{ for } j = 3p-2 \text{ and } 3p, \quad D_j = \frac{2mE}{N}\left(\cos p\pi - 1\right) \text{ for } j = 3p-1 \tag{3-33}$$

A matrix **Q** that diagonalizes **A** is helpful for solving Eq. 3-31. The solution, obtained for $Y_p(t)$ (= $\xi_{3p-1}(t)$) and $X_p(t)$ (= $\xi_{3p-2}(t)$), can be expressed in terms of **Q** and its inverse matrix $\mathbf{Q}^{-1}$ as

$$\begin{bmatrix} X_p(t) \\ Y_p(t) \end{bmatrix} = \sum_{\beta\geq 1} \begin{bmatrix} Q_{3p-2,\beta} \\ Q_{3p-1,\beta} \end{bmatrix} \times\left\{\eta_\beta^0 \exp[-\lambda_\beta t] + \frac{1}{\zeta}\sum_{\alpha\geq 1}\int_0^t \mathrm{d}t'\; \mathrm{Q}^{-1}_{\beta,\alpha}\left[B_\alpha(t) + D_\alpha\right] \exp[-\lambda_\beta (t-t')]\right\} \tag{3-34}$$

with

$$\eta_\beta^0 = \sum_{j\geq 1} \mathrm{Q}^{-1}_{\beta,j}\xi_j(0) \tag{3-35}$$

Here, $Q_{i,j}$ and $Q^{-1}_{i,j}$ are the i,j components of **Q** and $\mathbf{Q}^{-1}$, respectively, and λ_β is βth eigenvalue of **A** divided by ζ; Namely, $\{\mathbf{Q}^{-1}\mathbf{A}\mathbf{Q}\}_{\alpha\beta} = -\zeta\lambda_\beta\delta_{\alpha\beta}$.

Since the y component of the end-to-end vector is given by $R_{\mathrm{y}}(t) = \Sigma_{p\geq 1} Y_p(t)\{\cos p\pi - 1\}$ (cf. Eq. 3-6), the polarization $P_{\mathrm{ss}}(\mathrm{t})$ under steady shear at a time t after imposition of a small constant electric field, E, is straightforwardly obtained from Eq. 3-34 as

$$P_{\mathrm{ss}}(t;\dot\gamma) = \nu m\left\langle R_y(t+\tau)\right\rangle_{\tau\to\infty} = E\left\{\Phi^{\mathrm{un}}_{\mathrm{ss}}(0;\dot\gamma) - \Phi^{\mathrm{un}}_{\mathrm{ss}}(t;\dot\gamma)\right\} \tag{3-36}$$

Here, $\Phi^{\mathrm{un}}_{\mathrm{ss}}(t;\dot\gamma)$ is the unnormalized dielectric relaxation function given by

$$\Phi_{ss}^{un}(t;\dot{\gamma}) = \frac{2m^2\nu}{N\zeta}\sum_{\beta\geq 1} g_\beta^{[\Phi]}\exp\left(-\lambda_\beta t\right) \tag{3-37a}$$

with

$$g_\beta^{[\Phi]} = \frac{1}{\lambda_\beta}\left\{\sum_{p\geq 1}(\cos p\pi - 1)\; Q_{3p-1,\beta}\right\}\left\{\sum_{p'\geq 1}(\cos p'\pi - 1)\; Q^{-1}_{\beta',3p-1}\right\} \tag{3-37b}$$

A relationship deduced from the white noise character of the Brownian force, $\left\langle B_j(n,t)\right\rangle = 0$, has been utilized in derivation of Eq. 3-37.

Similarly, the other relationship deduced from this white noise character, $\left\langle B_i(t)B_j(t')\right\rangle = 4\zeta kTN^{-1}\delta_{ij}\delta(t-t')$, can be utilized in Eq. 3-34 with $D_\alpha = 0$ (in the absence of the electric field) to obtain an expression of the end-to-end vector correlation function,

$$\Psi_{ss}(t;\dot{\gamma}) \equiv \left\langle R_y(t)R_y(0)\right\rangle_{ss} = \frac{2k_BT}{N\zeta}\sum_{\beta\geq 1} g_\beta^{[\Psi]}\exp\left(-\lambda_\beta t\right) \tag{3-38a}$$

with

$$g_\beta^{[\Psi]} = \sum_{\beta'\geq 1}\frac{2}{\lambda_\beta + \lambda_{\beta'}}\left\{\sum_{\alpha\geq 1} Q^{-1}_{\beta,\alpha}Q^{-1}_{\beta',\alpha}\right\}$$

$$\times\left\{\sum_{p\geq 1}(\cos p\pi - 1)\; Q_{3p-1,\beta}\right\}\left\{\sum_{p'\geq 1}(\cos p'\pi - 1)\; Q^{-1}_{\beta',3p'-1}\right\} \tag{3-38b}$$

Eqs. 3-37 and 3-38, being identical to Eqs. 3-7 and 3-8 in the main text, clearly demonstrate that the dielectric modes and the end-to-end vector fluctuation modes have the identical relaxation times, $1/\lambda_\beta$, even under steady shear. In contrast, the mode intensities $g_\beta^{[\Phi]}$ and $g_\beta^{[\Psi]}$ do not exactly coincides with each other (cf. Eqs. 3-37b and 3-38b). Nevertheless, an argument related to the shear symmetry suggests the coincidence of $g_\beta^{[\Phi]}$ and $g_\beta^{[\Psi]}$ at least up to the order of $\dot{\gamma}^2$, as explained in Appendix 3B.

Appendix 3B: Perturbation Expansion

3B-1. *Expansion of matrix* **Q** *diagonalizing the interaction matrix A*

Because the matrix **A** defined by Eqs. 3-9 and 3-10 (with respect to the operator $\mathbf{\Lambda}$) depends on the shear rate $\dot{\gamma}$ in general, the diagonalizing matrix **Q** and its inverse matrix $\mathbf{Q}^{-1}$ introduced in Appendix 3A are also dependent on $\dot{\gamma}$. Thus, **Q** and $\mathbf{Q}^{-1}$ can be expanded, up to $O(\dot{\gamma}^2)$, as

$$\mathbf{Q} = \mathbf{Q}^{(0)} + \dot{\gamma}\mathbf{Q}^{(1)} + \dot{\gamma}^2\mathbf{Q}^{(2)}, \quad \mathbf{Q}^{-1} = \tilde{\mathbf{Q}}^{(0)} + \dot{\gamma}\tilde{\mathbf{Q}}^{(1)} + \dot{\gamma}^2\tilde{\mathbf{Q}}^{(2)} \tag{3-39}$$

Here, the superscripts "(0)", "(1)", and "(2)" stand for the zero-th, first-, and second-order expansion coefficients. The zero-th $\mathbf{Q}^{(0)}$ and $\tilde{\mathbf{Q}}^{(0)}$ are identical to **Q** and $\mathbf{Q}^{-1}$ at equilibrium, respectively, and satisfy an orthogonal relationship (because **A** is exactly symmetric at equilibrium),

$$\tilde{\mathbf{Q}}^{(0)} = \left[\mathbf{Q}^{(0)}\right]^{-1} = \left[\mathbf{Q}^{(0)}\right]^{+} \text{ (transpose of } \mathbf{Q}^{(0)}) \tag{3-40}$$

The first- and second-order coefficients for $\mathbf{Q}^{-1}$, $\tilde{\mathbf{Q}}^{(1)}$ and $\tilde{\mathbf{Q}}^{(2)}$, are not necessarily identical to the inverse matrices of the coefficients for **Q**, $\mathbf{Q}^{(1)}$ and $\mathbf{Q}^{(2)}$. Because $\mathbf{Q}\mathbf{Q}^{-1} = \mathbf{Q}^{-1}\mathbf{Q} = \mathbf{I}$, the matrices $\mathbf{Q}\mathbf{Q}^{-1}$ and $\mathbf{Q}^{-1}\mathbf{Q}$ are of the order of $\dot{\gamma}^0$. Thus, the coefficients should satisfy relationships,

$$\mathbf{Q}^{(0)}\tilde{\mathbf{Q}}^{(1)} + \mathbf{Q}^{(1)}\tilde{\mathbf{Q}}^{(0)} = \tilde{\mathbf{Q}}^{(0)}\mathbf{Q}^{(1)} + \tilde{\mathbf{Q}}^{(1)}\mathbf{Q}^{(0)} = \mathbf{0} \tag{3-41}$$

$$\mathbf{Q}^{(0)}\tilde{\mathbf{Q}}^{(2)} + \mathbf{Q}^{(1)}\tilde{\mathbf{Q}}^{(1)} + \mathbf{Q}^{(2)}\tilde{\mathbf{Q}}^{(0)} = \tilde{\mathbf{Q}}^{(0)}\mathbf{Q}^{(2)} + \tilde{\mathbf{Q}}^{(1)}\mathbf{Q}^{(1)} + \tilde{\mathbf{Q}}^{(2)}\mathbf{Q}^{(0)} = \mathbf{0} \tag{3-42}$$

3B-2. ***Symmetry of expansion coefficients of*** **Q**

It is convenient to introduce two correlation functions, $S_{yx}(n,n',t) \equiv \left\langle u_y(n,t)u_x(n',0)\right\rangle$ and $S_{yy}(n,n',t) \equiv \left\langle u_y(n,t)u_y(n',0)\right\rangle$ defined with respect to the y and x components of the bond vector $\mathbf{u}(n,t)$ ($=\partial\mathbf{r}(n,t)/\partial n$) under steady shear, for examining the relationship between the dielectric relaxation function $\Phi_{ss}^{un}(t;\dot\gamma)$ (Eq. 3-37) and end-to-end vector auto-correlation function $\Psi_{ss}(t;\dot\gamma)$ (Eq. 3-37): $\Psi_{ss}(t;\dot\gamma)$ is identical to $\int_0^N \mathrm{d}n\,\mathrm{d}n'\, S_{yy}(n,n',t)$ and has the same symmetry as $S_{yy}(n,n',t)$ with respect to $\dot\gamma$. Specifically, Ψ_{ss} and S_{yy} should be even functions of $\dot\gamma$, because they remain the same on reversal of shear direction. In contrast, $S_{yx}(n,n',t)$ should change its sign on the shear reversal and is an odd function of $\dot\gamma$. This S_{xy} is introduced as a reference for expansion of S_{yy}.

The steady state is already achieved at time 0 (when the electric field is applied). Then, from Eq. 3-34, S_{yx} and S_{yy} are easily calculated as

$$S_{yx}(n,n',t) = \sum_{p,p'} \frac{pp'\pi^2}{N^2}\sin\left(\frac{p\pi n}{N}\right)\sin\left(\frac{p'\pi n'}{N}\right)\left\langle Y_p(t+\tau)X_{p'}(\tau)\right\rangle_{\tau\to\infty} \tag{3-43a}$$

with

$$\left\langle Y_p(t+\tau)X_{p'}(\tau)\right\rangle_{\tau\to\infty} = \frac{4k_BT}{N\zeta}\sum_{\beta,\beta'\ge 1} Q_{3p-1,\beta}Q_{3p'-2,\beta'}\left\{\sum_{\alpha\ge 1} Q^{-1}_{\beta,\alpha}Q^{-1}_{\beta',\alpha}\right\}\frac{\exp(-\lambda_\beta t)}{\lambda_\beta+\lambda_{\beta'}} \tag{3-43b}$$

and

$$S_{yy}(n,n',t) = \sum_{p,p'} \frac{pp'\pi^2}{N^2}\sin\left(\frac{p\pi n}{N}\right)\sin\left(\frac{p'\pi n'}{N}\right)\left\langle Y_p(t+\tau)Y_{p'}(\tau)\right\rangle_{\tau\to\infty} \tag{3-44a}$$

with

$$\left\langle Y_p(t+\tau)Y_{p'}(\tau)\right\rangle_{\tau\to\infty} = \frac{4k_BT}{N\zeta}\sum_{\beta,\beta'\geq 1} Q_{3p-1,\beta}Q_{3p'-1,\beta'}\left\{\sum_{\alpha\geq 1} Q^{-1}_{\beta,\alpha}Q^{-1}_{\beta',\alpha}\right\}\frac{\exp(-\lambda_\beta t)}{\lambda_\beta+\lambda_{\beta'}} \quad (3\text{-}44b)$$

Because S_{yx} is an odd function of $\dot{\gamma}$, the terms of the order of $\dot{\gamma}^{2k}$ (k = 0, 1,...) obtained after expansion of $\left\langle Y_p(t+\tau)X_{p'}(\tau)\right\rangle_{\tau\to\infty}$ (Eq. 3-43b) should vanish at any time t and for any indices p and p'. Similarly, the terms of the order of $\dot{\gamma}^{2k+1}$ (k = 0, 1,...) obtained after expansion of $\left\langle Y_p(t+\tau)Y_{p'}(\tau)\right\rangle_{\tau\to\infty}$ (Eq. 3-44b for the even function S_{yy}) should vanish at any time t and for any indices. The $\left\langle Y_p(t+\tau)X_{p'}(\tau)\right\rangle_{\tau\to\infty}$ and $\left\langle Y_p(t+\tau)Y_{p'}(\tau)\right\rangle_{\tau\to\infty}$ terms include the relaxation rate λ_β and the components of the matrices, $\mathbf{Q}$ and $\mathbf{Q}^{-1}$. Thus, these terms can be straightforwardly expanded with respect to $\dot{\gamma}$, with the aid of Eq. 3-11a ($\lambda_\beta = \lambda_\beta^{(0)} + \dot{\gamma}^2\lambda_\beta^{(2)} + O(\dot{\gamma}^4)$; even function of $\dot{\gamma}$) and Eq. 3-39 (expansion of $\mathbf{Q}$ and $\mathbf{Q}^{-1}$) as well as the orthogonal feature of $\mathbf{Q}^{(0)}$ (Eq. 3-40). The results in turn give useful information for $\mathbf{Q}$ and $\mathbf{Q}^{-1}$, as explained below.

(i) The $O(\dot{\gamma}^0)$ term for $\left\langle Y_p(t+\tau)X_{p'}(\tau)\right\rangle_{\tau\to\infty}$:

This term, given by $\{2k_BT/N\zeta\}\Sigma_{\beta\geq 1} Q^{(0)}_{3p-1,\beta}Q^{(0)}_{3p'-2,\beta}\{\lambda^{(0)}_\beta\}^{-1}\exp\{-\lambda^{(0)}_\beta t\}$ (cf. Eq.3-43b), is required to vanish for any p, p' and at any t. This requirement is satisfied when the following relationship is valid.

$$Q^{(0)}_{3p-1,\beta}Q^{(0)}_{3p'-2,\beta} = 0 \quad \text{for } \textit{any} \quad p, p', \text{ and } \beta \quad (3\text{-}45)$$

Namely, $Q^{(0)}_{3p-1,\beta}$ and $Q^{(0)}_{3p'-2,\beta}$ at equilibrium cannot simultaneously have non-zero values when their second indices (β) are the same. In fact, this feature of $Q^{(0)}_{3p-1,\beta}$ and $Q^{(0)}_{3p'-2,\beta}$ is necessary to guarantee the Gaussian conformation of the chain at equilibrium.

(ii) The $O(\dot{\gamma}^1)$ term for $\left\langle Y_p(t+\tau)Y_{p'}(\tau)\right\rangle_{\tau\to\infty}$:

This term is given by $\{2k_{\mathrm{B}}T/N\zeta\}\Sigma_{\beta\geq 1} w^{(1)}_{p,p',\beta}\{\lambda^{(0)}_\beta\}^{-1}\exp(-\lambda^{(0)}_\beta t)$, with the coefficient $w^{(1)}_{p,p',\beta}$ being specified as

$$w^{(1)}_{p,p',\beta} = Q^{(0)}_{3p-1,\beta}Q^{(1)}_{3p'-1,\beta} + Q^{(1)}_{3p-1,\beta}Q^{(0)}_{3p'-1,\beta} + \sum_{\beta'\geq 1}\frac{2Q^{(0)}_{3p-1,\beta}Q^{(0)}_{3p'-1,\beta'}}{1+\{\lambda^{(0)}_{\beta'}/\lambda^{(0)}_\beta\}}\left\{\sum_{\alpha\geq 1}\left(\tilde{Q}^{(0)}_{\beta,\alpha}\tilde{Q}^{(1)}_{\beta',\alpha} + \tilde{Q}^{(1)}_{\beta,\alpha}\tilde{Q}^{(0)}_{\beta',\alpha}\right)\right\} \tag{3-46}$$

Because $\left\langle Y_p(t+\tau)Y_{p'}(\tau)\right\rangle_{\tau\to\infty}$ is an even function of $\dot{\gamma}$, this $w^{(1)}_{p,p',\beta}$ is required to vanish for *any* set of the indices, p, p', and β. This is a strong requirement when combined with Eq. 3-45, and a "sufficient condition" to meet this requirement is given by

$$Q^{(0)}_{3p-1,\beta}Q^{(1)}_{3p'-1,\beta} + Q^{(1)}_{3p-1,\beta}Q^{(0)}_{3p'-1,\beta} = 0 \quad \text{for any } p,\ p' \text{ and } \beta. \tag{3-47}$$

and

$$\sum_{\alpha\geq 1}\left(\tilde{Q}^{(0)}_{\beta,\alpha}\tilde{Q}^{(1)}_{\beta',\alpha} + \tilde{Q}^{(1)}_{\beta,\alpha}\tilde{Q}^{(0)}_{\beta',\alpha}\right) = 0 \quad \text{for any } \beta \text{ and } \beta' \tag{3-48}$$

Furthermore, combination of Eq. 3-48 with Eqs. 3-40 and 3-42 gives

$$\tilde{\mathbf{Q}}^{(1)} = \left[\mathbf{Q}^{(1)}\right]^+ \ \text{(transpose of } \mathbf{Q}^{(1)}) \tag{3-49}$$

Namely, $\tilde{\mathbf{Q}}^{(1)}$ is an orthogonal matrix. Eqs. 3-47 and 3-48 are not identical but close to the "sufficient and necessary" condition for the requirement, $w^{(1)}_{p,p',\beta} = 0$ for any p, p' and β.

(iii) The $O(\dot{\gamma}^2)$ term for $\left\langle Y_p(t+\tau)X_{p'}(\tau)\right\rangle_{\tau\to\infty}$:

This term is expressed as $\{2k_{\mathrm{B}}T/N\zeta\}\Sigma_{\beta\geq 1} w^{(2)}_{p,p',\beta}\{\lambda^{(0)}_\beta\}^{-1}\exp(-\lambda^{(0)}_\beta t)$ (cf. Eqs. 3-40, 3-45, and 3-48), with the coefficient $w^{(2)}_{p,p',\beta}$ being given by

$$w^{(2)}_{p,p',\beta} = Q^{(0)}_{3p-1,\beta}Q^{(2)}_{3p'-2,\beta} + Q^{(1)}_{3p-1,\beta}Q^{(1)}_{3p'-2,\beta} + Q^{(2)}_{3p-1,\beta}Q^{(0)}_{3p'-2,\beta}$$

$$+ \sum_{\beta'\geq 1} \frac{2Q^{(0)}_{3p-1,\beta}Q^{(0)}_{3p'-2,\beta'}}{1+\{\lambda^{(0)}_{\beta'}/\lambda^{(0)}_{\beta}\}} \left\{ \sum_{\alpha\geq 1} \left(\tilde{Q}^{(0)}_{\beta,\alpha}\tilde{Q}^{(2)}_{\beta',\alpha} + \tilde{Q}^{(1)}_{\beta,\alpha}\tilde{Q}^{(1)}_{\beta',\alpha} + \tilde{Q}^{(2)}_{\beta,\alpha}\tilde{Q}^{(0)}_{\beta',\alpha} \right) \right\} \qquad (3\text{-}50)$$

Because $\left\langle Y_p(t+\tau)X_{p'}(\tau)\right\rangle_{\tau\to\infty}$ is an odd function of $\dot{\gamma}$, this $w^{(2)}_{p,p',\beta}$ is required to vanish for *any* set of the indices, p, p', and β. This is again a strong requirement when combined with Eqs. 3-45 and 3-47, and the "sufficient" condition for this requirement (close to the "sufficient and necessary" condition) is specified by $Q^{(0)}_{3p-1,\beta}Q^{(2)}_{3p'-2,\beta} + Q^{(1)}_{3p-1,\beta}Q^{(1)}_{3p'-2,\beta} + Q^{(2)}_{3p-1,\beta}Q^{(0)}_{3p'-2,\beta} = 0$ (for any p, p' and β) and

$$\sum_{\alpha\geq 1} \left(\tilde{Q}^{(0)}_{\beta,\alpha}\tilde{Q}^{(2)}_{\beta',\alpha} + \tilde{Q}^{(1)}_{\beta,\alpha}\tilde{Q}^{(1)}_{\beta',\alpha} + \tilde{Q}^{(2)}_{\beta,\alpha}\tilde{Q}^{(0)}_{\beta',\alpha} \right) = 0 \quad \text{for any } \beta \text{ and } \beta' \qquad (3\text{-}51)$$

Combination of Eq. 3-51 with Eqs. 3-40 and 3-42 gives

$$\tilde{\mathbf{Q}}^{(2)} = \left[\mathbf{Q}^{(2)}\right]^{+} \quad \text{(transpose of } \mathbf{Q}^{(2)}\text{)} \qquad (3\text{-}52)$$

Namely, $\tilde{\mathbf{Q}}^{(2)}$ is an orthogonal matrix.

3B-3. *Relationship between mode intensities of* $\mathbf{\Phi}^{\mathbf{un}}_{\mathbf{ss}}$ and $\mathbf{\Psi}_{\mathbf{ss}}$

The above results can be utilized to examine the relationship between the dielectric relaxation function $\Phi^{\mathrm{un}}_{\mathrm{ss}}(t;\dot{\gamma}) = \Phi^{\mathrm{un}(0)}(t) + \dot{\gamma}\Phi^{\mathrm{un}(1)}_{\mathrm{ss}}(t) + \dot{\gamma}^2\Phi^{\mathrm{un}(2)}_{\mathrm{ss}}(t)$ and the end-to-end vector auto-correlation function, $\Psi_{\mathrm{ss}}(t;\dot{\gamma}) = \Psi^{(0)}(t) + \dot{\gamma}\Psi^{(1)}_{\mathrm{ss}}(t) + \dot{\gamma}^2\Psi^{(2)}_{\mathrm{ss}}(t)$. From Eqs. 3-37 and 3-38 combined with Eqs. 3-39 and 3-40, the zero-th order terms of these functions, $\Phi^{\mathrm{un}(0)}(t)$ and $\Psi^{(0)}(t)$ (at equilibrium), are expressed as

$$\Phi^{\mathrm{un}(0)}(t) = \frac{2\tilde{\mu}^2\nu}{N\zeta}\sum_{\beta\geq 1} g_\beta^{(0)} \exp\left(-\lambda_\beta^{(0)} t\right) \quad \text{and} \quad \Psi^{(0)}(t) = \frac{2k_{\mathrm{B}}T}{N\zeta}\sum_{\beta\geq 1} g_\beta^{(0)} \exp\left(-\lambda_\beta^{(0)} t\right) \qquad \text{(3-53a)}$$

with

$$g_\beta^{(0)} = \frac{1}{\lambda_\beta^{(0)}}\left\{\sum_{p\geq 1}(\cos p\pi - 1) Q_{3p-1,\beta}^{(0)}\right\}^2 \qquad \text{(3-53b)}$$

Namely, $\Phi^{\mathrm{un}(0)}(t) = \{\tilde{\mu}^2\nu/k_{\mathrm{B}}T\}\Psi^{(0)}(t)$ at any t, and these functions are rigorously proportional to each other (which confirms the validity of Green-Kubo theorem at equilibrium).

For $\Psi_{\mathrm{ss}}(t;\dot{\gamma})$, the first order expansion coefficient $\Psi_{\mathrm{ss}}^{(1)}(t)$ vanishes because of Eqs. 3-47 and 3-48 (because $\Psi_{\mathrm{ss}}(t;\dot{\gamma})$ is an even function of $\dot{\gamma}$). The first order expansion coefficient should vanish also for $\Phi_{\mathrm{ss}}^{\mathrm{un}}(t;\dot{\gamma})$ (an even function of $\dot{\gamma}$). This fact can be confirmed from Eqs. 3-37 that give

$$\Phi_{\mathrm{ss}}^{\mathrm{un}(1)}(t) = \{2m^2\nu/N\zeta\}\Sigma_{\beta\geq 1} g_\beta^{[\Phi](1)} \exp\left(-\lambda_\beta^{(0)} t\right) \qquad \text{(3-54a)}$$

with

$$g_\beta^{[\Phi](1)} = \frac{1}{\lambda_\beta^{(0)}}\sum_{p,p'\geq 1}(\cos p\pi - 1)(\cos p'\pi - 1)\left(Q_{3p-1,\beta}^{(0)} Q_{3p'-1,\beta}^{(1)} + Q_{3p-1,\beta}^{(1)} Q_{3p'-1,\beta}^{(0)}\right) \qquad \text{(3-54b)}$$

As seen from Eq. 3-47, this $g_\beta^{[\Phi](1)}$ vanishes and thus $\Phi_{\mathrm{ss}}^{\mathrm{un}(1)}(t) = 0$ at any t. It should be also noted that $g_\beta^{[\Phi](1)} = \{2/\lambda_\beta^{(0)}\}\left\{\Sigma_{p\geq 1}(\cos p\pi - 1) Q_{3p-1,\beta}^{(0)}\right\} \times \left\{\Sigma_{p'\geq 1}(\cos p'\pi - 1) Q_{3p'-1,\beta}^{(1)}\right\}$ and thus the relationship $g_\beta^{[\Phi](1)} = 0$ is equivalent to a relationship

$$\sum_{p'\geq 1}(\cos p'\pi - 1) Q_{3p'-1,\beta}^{(1)} = 0 \quad \text{for any } \beta \qquad \text{(3-55)}$$

Finally, from Eqs. 3-40, 3-47, 3-48, 3-51, 3-52, and 3-55, the second order expansion coefficients for $\Psi_{\mathrm{ss}}(t;\dot{\gamma})$ and $\Phi_{\mathrm{ss}}^{\mathrm{un}}(t;\dot{\gamma})$ are obtained as

$$\Psi_{ss}^{(2)}(t) = \frac{2k_BT}{N\zeta}\sum_{\beta\geq 1} g_\beta^{(2)}(t)\ \exp\left(-\lambda_\beta^{(0)}t\right) \quad \text{and} \quad \Phi_{ss}^{un(2)}(t) = \frac{2\tilde{\mu}^2\nu}{N\zeta}\sum_{\beta\geq 1} g_\beta^{(2)}(t)\ \exp\left(-\lambda_\beta^{(0)}t\right)$$

with

$$g_\beta^{(2)} = \frac{2}{\lambda_\beta^{(0)}}\left\{\sum_{p\geq 1}(\cos p\pi - 1)Q_{3p-1,\beta}^{(0)}\right\}\left\{\sum_{p'\geq 1}(\cos p'\pi - 1)Q_{3p'-1,\beta}^{(2)}\right\}$$

$$- \frac{1}{\lambda_\beta^{(0)}}\left\{\frac{\lambda_\beta^{(2)}}{\lambda_\beta^{(0)}} + \lambda_\beta^{(2)}t\right\}\left\{\sum_{p\geq 1}(\cos p\pi - 1)Q_{3p-1,\beta}^{(0)}\right\}^2 \qquad (3\text{-}56)$$

Thus, $\Phi_{ss}^{un(2)}(t;\dot{\gamma}) = \{\tilde{\mu}^2\nu/k_BT\}\Psi_{ss}^{(2)}(t;\dot{\gamma})$ at any t. This result, combined with eq. 3-53, strongly suggests that the Green-Kubo theorem, $\Phi_{ss}^{un}(t;\dot{\gamma}) = \{\tilde{\mu}^2\nu/k_BT\}\Psi_{ss}(t;\dot{\gamma})$, is valid at least up to the order of $\dot{\gamma}^2$ (or higher).

Appendix 3C: NAPLES Simulation

Masubuchi et al[7] developed a method of coarse-grained molecular simulation (NAPLES) for entangled chains based on the primitive chain network model. In this model, the network is composed of Gaussian chains that are pair-wisely connected at temporary sliplinks (that represent entanglements), and the chains are allowed to slide along the array of sliplinks according to a balance of forces acting on each portion of the chains between sliplinks (this portion is referred as a strand); the forces considered are the frictional force from a medium, the elastic force due to the conformational entropy of a strand, the Brownian force activating diffusion, and the thermodynamic force reducing any spatial gradient of segment density (a force due to chemical potential). The segment number in each strand is allowed to

fluctuate according to a similar force balance. The sliplink fluctuates/moves in space following the force balance for the strands. In addition, the sliplink penetrated by a strand at the chain end is occasionally removed/created on decrease/increase of the segment number in this strand below/above critical values. Mathematical formulation of these kinetic changes has been fully explained in literature.[7,8,12-14)]

Masubuchi et al[7,8,12-14)] demonstrated that the NAPLES simulation describes considerably well the linear and nonlinear viscoelastic behavior of entangled homopolymers including PI (and the dielectric behavior of linear PI at equilibrium). For PI under *steady shear*, they also conducted a preliminary NAPLES simulation[7)] incorporating the convective constraint release (CCR) mechanism and the so-called hidden entanglement appearance (HEA)[16)] mechanism to calculate the rheo-dielectric response. The CCR mechanism represents the release of the entanglement for a given chain due to contraction of surrounding chains under the shear, and the HEA mechanism considers that a chain that was neighboring to but not entangled with the given chain before occurrence of CCR is hooked by that chain after CCR. In the rheo-dielectric simulation, Masubuchi et al[7)] put positive and negative charges at respective ends of the entangled linear chains and directly evaluated, by monitoring the spatial distribution of these charges, the macroscopic polarization $P_{ss}(t)$ induced by a weak electric field E. These charges are equivalent to a sum of type-A dipoles of the chain. Thus, the simulation well mimicked the actual rheo-dielectric experiments for PI under steady shear.

In the simulation, the macroscopic dielectric relaxation function directly obtained from this $P_{ss}(t)$ agreed with the auto-correlation function of the end-to-end vector R_y in the shear gradient direction,[7] lending support to Eqs. 3-12 and 3-13 in the main text.

In this study, the NAPLES simulation incorporating the CCR and HEA mechanisms was conducted again (but with better statistics) for the rheo-dielectric behavior of entangled linear PI under steady shear as well as LAOS. The HEA parameter l_c^2, specifying a spatial range where the entanglement can be created, was set at 2.0, as done in the previous study.[7]

The simulation was made for monodisperse linear chains each having 9.6 entanglement segments on average at equilibrium. The simulation box size and segment density were $(16a)^3$ and $10a^{-3}$, respectively, with a being an average length of entanglement segment. This box was subjected to steady shear and/or LAOS, both being generated with SLLOD and Lees-Edwards boundary condition.[7] The steady shear rate as well as the LAOS frequency and amplitude in the simulation mimicked the actual experimental conditions. For each chain in the box, a positive charge m was attached to one end, and a negative charge $-m$ to the other end. (These charges are equivalent to the type-A dipoles summed along the chain backbone.) The chains under steady shear or LAOS were also subjected to a small oscillatory electric field ($E(t) = E_0 \sin \omega t$) in the shear gradient direction. The resulting, macroscopic polarization $P(t)$ was directly evaluated from the spatial distribution of the chain ends, and the dielectric loss was calculated from this $P(t)$. The mean-square end-to-end

distance $\left\langle R_y^2 \right\rangle_{\mathrm{LAOS}}$ was also evaluated under steady shear and LAOS. The simulated results are shown in Figs. 3-2, 3-3, and 3-4 in the main text.

References

1) H. Watanabe, Progress in Polymer Science, 24, 1253 (1999).

2) T. C. B. McLeish, Advances in Physics, 51, 1379 (2002).

3) R. Kubo, Journal of Physical Society Japan, 12, 570 (1957).

4) D. Evans and P. Morris, Statistical Mechanics of Nonequilibrium Liquids, Academic Press: London, 1990.

5) Y. Matsumiya, H. Watanabe, T. Inoue, K. Osaki, and M. L. Yao, Macromolecules, 31, 7973 (1998).

6) H. Watanabe, S. Ishida, and Y. Matsumiya, Macromolecules, 35, 8802 (2002).

7) Y. Masubuchi, H. Watanabe, G. Ianniruberto, F. Greco, and G. Marrucci, Nihon Reoroji Gakkaishi (Journal of the Society of Rheology, Japan), 32, 197 (2004).

8) Y. Masubuchi, J. Takimoto, K. Koyama, G. Ianniruberto, F. Greco, and G. Marrucci, Journal of Chemical Physics, 115, 4387 (2001).

9) S. Höfl, F. Kremer, H. W. Spiess, M. Wilhelm, and S. Kahle, Polymer, 47, 7282 (2006).

10) S. Capaccioli, D. Prevosto, A. Best, A. Hanewald, and T. Pakula, Journal of Non-Crystalline Solids, 353, 4267 (2007).

11) R. Cole, Journal of Chemical Physics, 42, 637 (1965).

12) Y. Masubuchi, G. Ianniruberto, G. Marrucci, F. Greco, Journal of Chemical Physics, 119, 6925 (2003).

13) Y. Masubuchi, G. Ianniruberto, F. Greco, and G. Marrucci, Journal of Non-Newtonian Fluid Mechanics, 149, 87 (2008).

14) Y. Masubuchi, Nihon Reoroji Gakkaishi (Journal of the Society of Rheology, Japan), 34, 275 (2006).

15) G. Ianniruberto and G. Marrucci, Journal of Non-Newtonian Fluid Mechanics, 65, 241 (1996).

16) G. Ianniruberto and G. Marrucci, Journal of Non-Newtonian Fluid Mechanics, 95, 363 (2000).

Chapter 4. Dynamical Model with Anisotropic Mobility Tensor for Polymers under Shear

4-1. Introduction

As briefly shown in previous Chapters, the linear response theory states that the linear responses of a system to weak external (perturbation) fields can be expressed by the Green-Kubo formula. Namely, the response function $K_{AB}(t\text{-}t')$ of a physical quantity A at time t to a perturbation, which is conjugate to a physical quantity B, at time t' ($\leq t$), becomes[1,2)]

$$K_{AB}(t) = \frac{1}{k_B T}\frac{d}{dt'}\left\langle A(t)B(t')\right\rangle_{\text{eq}} \qquad (4\text{-}1)$$

Here, k_B is the Boltzmann constant, T is the temperature of the system, and $\left\langle \cdots \right\rangle_{\text{eq}}$ represents the *equilibrium* statistical average. Eq. 4-1 is useful because it relates an *experimentally observed macroscopic* linear response function and the time correlation function of *microscopic, molecular-level* physical quantities. For example, one can validate theoretical models, or obtain molecular scale dynamic information from experiments, on the basis of Eq. 4-1. Actually, the linear viscoelasticity and the dielectric response have been successfully analyzed on the basis of the Green-Kubo theorem.[3-7)]

However, it should be also noted that the Green-Kubo theorem at equilibrium is generally *invalid* in non-equilibrium systems (even if the system is in steady state). Therefore, in general, a blind use of the Green-Kubo formula, Eq. 4-1, for the analysis of some response

functions in a non-equilibrium state, will lead to *qualitatively* incorrect results. For some limited cases such as the rheo-dielectric response of polymers with type-A dipoles[8-11], fortunately, the Green-Kubo theorem (approximately) holds even in non-equilibrium sheared states, as demonstrated in Chapter 3. However, the rheo-dielectric data by themselves poses a serious question about the chain dynamics; the dielectric intensity and relaxation time are hardly affected by the shear, whereas the shear viscosity exhibits strong shear thinning (cf. Fig. 3-2). The conventional idea such as the "convective constrain release" (CCR)[12] cannot explain this apparent inconsistency observed experimentally.

The dynamic equations of coarse-grained molecular models are often cast in a form of Langevin equations.[1] Formulation of the Langevin equation requires the mobility (or the friction coefficient) as well as the potential energy (or the free energy). According to the fluctuation-dissipation relation,[1] the mobility is formally given as the correlation function of the physical quantity in equilibrium. If the system is *near equilibrium* (if the applied perturbation is weak), the Langevin equation reproduces the correct Maxwell-Boltzmann distribution and describes the dynamics. Conversely, the validity of the Langevin equation is generally *not guaranteed* in non-equilibrium systems. Indeed, the simple extrapolation of the equilibrium dynamics models of entangled polymers into polymer systems under fast shear cannot describe experimental data such as rheo-dielectric responses. To model the non-equilibrium dynamics of polymers, the non-equilibrium version of the Langevin

equation[13] will be required.

Besides, recently new linear response theories have been proposed for non-equilibrium steady states, some of which give generalized Green-Kubo type relations.[14-19] Thus, rigorous analysis will be possible with the tools developed in the field of non-equilibrium statistical mechanics. Combination of the non-equilibrium Langevin equation and the generalized Green-Kubo formula will be helpful to understand the dynamics of polymers under fast shear.

In this chapter, the non-equilibrium version of the Langevin equation for weakly entangled polymers under fast shear is constructed, on the basis of the non-equilibrium statistical physics and simulation data. Then, the linear response against a weak field superposed on the steady shear is calculated. The concept of the *"anisotropic mobility",* which naturally arises from the physical arguments, plays an important role for the dynamics of weakly entangled polymers under shear.

4-2. Model

In equilibrium, the dynamics of a weakly entangled polymer chain is expected to be described by the Langevin equation. The required degrees of freedom depend on the target phenomena. For the long-time dynamics, detailed conformation of a polymer chain is not important, and a simple Langevin equation for the end-to-end vector **R** can be employed:

$$\frac{d\mathbf{R}(t)}{dt} = -\frac{1}{\zeta_0}\frac{\partial F(\mathbf{R}(t))}{\partial \mathbf{R}(t)} + \boldsymbol{\xi}_0(t) \tag{4-2}$$

Here, ζ_0 is the effective friction coefficient, and F is the (effective) free energy being expressed as

$$F(\mathbf{R}(t)) = \frac{3k_BT}{2\langle R^2\rangle_{\mathrm{eq}}}\mathbf{R}^2 \tag{4-3}$$

$\boldsymbol{\xi}_0(t)$ is the Gaussian white noise that satisfies the following fluctuation-dissipation relation.[1)]

$$\langle \boldsymbol{\xi}_0(t)\rangle = \mathbf{0}, \quad \langle \boldsymbol{\xi}_0(t)\boldsymbol{\xi}_0(t')\rangle = \frac{2k_BT}{\zeta_0}\delta(t-t')\mathbf{I} \tag{4-4}$$

($\langle\cdots\rangle$ represents the statistical average and $\mathbf{I}$ is the unit tensor in three dimensions.)

If the system is subjected to a weak shear flow, of which the velocity gradient tensor $\boldsymbol{\kappa}$ is given as

$$\kappa_{\alpha\beta} = \begin{cases} \dot{\gamma} & (\alpha = x, \beta = y) \\ 0 & (\text{otherwise}) \end{cases} \tag{4-5}$$

with $\dot{\gamma}$ being the shear rate, the Langevin equation for a sheared system is obtained by simply adding a convection term to Eq. 4-2:

$$\frac{d\mathbf{R}(t)}{dt} = -\frac{1}{\zeta_0}\frac{\partial F(\mathbf{R}(t))}{\partial \mathbf{R}(t)} + \boldsymbol{\kappa}\cdot\mathbf{R}(t) + \boldsymbol{\xi}_0(t) \tag{4-6}$$

Eq. 4-6 holds *near or in equilibrium*, and rheological properties such as the zero shear viscosity and the shear relaxation modulus can be calculated by Eq. 4-6. However, it is *not justified for a polymer under fast shear* and thus the construction of a Langevin equation for non-equilibrium state is required.

McPhie *et al*[13)] considered the non-equilibrium Langevin equation for Lennard-Jones particles under shear. They employed the projection operator method[1)] together with the

diffusion coefficient tensor obtained by the molecular dynamics (MD) simulations. They proposed the Langevin equation involving the anisotropic friction tensor as the dynamic equation under shear. Hunt and Todd[20] performed MD simulations of polymers under shear flow at various shear rates, and reported that the diffusion behavior becomes highly anisotropic under fast shear. These results imply that the dynamics of polymers under fast shear can be modeled with an *anisotropic mobility* tensor, as follows.

$$\frac{d\mathbf{R}(t)}{dt} = -\mathbf{M}(\dot{\gamma}) \cdot \frac{\partial F(\mathbf{R}(t))}{\partial \mathbf{R}(t)} + \boldsymbol{\kappa} \cdot \mathbf{R}(t) + \boldsymbol{\xi}(\dot{\gamma};t) \qquad (4\text{-}7)$$

Here, $\mathbf{M}(\dot{\gamma})$ is the (anisotropic) mobility tensor that depends on the shear rate, and $\boldsymbol{\xi}(\dot{\gamma};t)$ is the Gaussian white noise that also depends on the shear rate. Although the fluctuation-dissipation relation is not required to hold under shear, it may be reasonable to assume validity of this relation under shear. Then, the noise and the mobility tensor can be related as

$$\langle \boldsymbol{\xi}(\dot{\gamma};t) \rangle = 0, \quad \langle \boldsymbol{\xi}(\dot{\gamma};t)\, \boldsymbol{\xi}(\dot{\gamma};t') \rangle = 2k_B T \delta(t-t') \mathbf{M}(\dot{\gamma}) \qquad (4\text{-}8)$$

The explicit form of the mobility tensor $\mathbf{M}(\dot{\gamma})$ is not trivial. The symmetry argument and some physically natural requirements limit the form of the mobility tensor. The diffusion data obtained from MD simulation is also helpful to consider the explicit form of the mobility tensor (because the mobility tensor is proportional to the diffusion coefficient tensor). These information limits the possible form of the mobility tensor. The mobility tensor should satisfy the following requirements.

(1) The mobility tensor should be positive definite (all the eigenvalues should be positive), to make the steady state under shear thermally stable.

(2) The eigenvalues of the mobility tensor should be unchanged on reversal of shear, $\dot{\gamma} \to -\dot{\gamma}$.

(3) The *xx*-component of the mobility tensor should increase as the shear rate increases, whereas the shear rate dependence of the *yy*- and *zz*-components should be weak.

(4) The *xy*-component should be independent or just weakly dependent on the shear rate.

(5) The *xz*- and *yz*-components of the mobility tensor should be zero.

(6) The mobility tensor should reduce to the equilibrium mobility tensor in the limit of $\dot{\gamma} = 0$.

A simple form which satisfies these requirements is

$$\mathbf{M}(\dot{\gamma}) = \frac{1}{\zeta_0}\begin{bmatrix} \tilde{\lambda}(\dot{\gamma}) & 0 & 0 \\ 0 & 1 & 0 \\ 0 & 0 & 1 \end{bmatrix} \tag{4-9}$$

where $\tilde{\lambda}(\dot{\gamma})$ is an even function of $\dot{\gamma}$ that monotonically decreases with increasing $\dot{\gamma}$. The following phenomenological power-law type form for $\tilde{\lambda}(\dot{\gamma})$ will be useful.

$$\tilde{\lambda}(\dot{\gamma}) = [1 + (\tau_c \dot{\gamma})^2]^{\alpha/2} \tag{4-10}$$

Here, τ_c is the characteristic crossover time and $\alpha < 1$ is the characteristic exponent. The

crossover time is expected to be comparable to the relaxation time of the end-to-end vector, $\tau_0 \equiv \zeta_0 \langle R^2 \rangle_{eq} / 3k_B T$. As shown later, the exponent α is related to the exponent of the shear thinning. If the shear rate is sufficiently larger than τ_c^{-1}, Eq. 4-10 reduces to $\tilde{\lambda}(\dot{\gamma}) \approx (\tau_c \dot{\gamma})^{\alpha}$ and dynamics becomes anisotropic. On the other hand, if the shear rate is sufficiently small, Eq. 4-10 becomes $\tilde{\lambda}(\dot{\gamma}) \cong 1$ and the equilibrium Langevin equation (Eq. 4-2) is recovered. Eqs. 4-7 to 4-10 give the explicit form of the dynamic equation for **R**. The resulting dynamic equation is linear in **R**, and thus is analytically solvable. (The Fokker-Planck equation[2)] and the path integral formalism can be utilized to solve the Langevin equation.) Thus the "*anisotropic mobility model*" shown above can give the analytic forms of experimentally observable quantities such as the rheo-dielectric response function.

4-3. Results

4-3-1. Steady state shear viscosity

Following the stress-optical rule, the microscopic stress tensor is expressed as

$$\boldsymbol{\sigma}(\mathbf{R}) = \frac{3\nu_0 k_B T}{\langle R^2 \rangle_{eq}} \mathbf{RR} \tag{4-11}$$

Here, ν_0 is the average number density of polymer chain. The steady state shear viscosity and the first normal stress difference are calculated to be

$$\eta(\dot{\gamma}) = \frac{\langle \sigma_{xy} \rangle_{ss}}{\dot{\gamma}} = \frac{3\nu_0 k_B T}{\dot{\gamma} \langle R^2 \rangle_{eq}} \langle R_x R_y \rangle_{ss} = \eta_0 \frac{2}{1 + \tilde{\lambda}(\dot{\gamma})} \tag{4-12}$$

$$\Psi_1(\dot{\gamma}) = \frac{\langle \sigma_{xx} - \sigma_{yy} \rangle_{ss}}{\dot{\gamma}^2} = \frac{3\nu_0 k_B T}{\dot{\gamma}^2 \langle R^2 \rangle_{eq}} \langle R_x^2 - R_y^2 \rangle_{ss} = \Psi_{1,0} \frac{2}{\tilde{\lambda}(\dot{\gamma})[1 + \tilde{\lambda}(\dot{\gamma})]} \qquad (4\text{-}13)$$

where $\langle \ldots \rangle_{ss}$ represents the statistical average under steady shear, $\eta_0 = \nu_0 k_B T \tau_0 / 2$ and $\Psi_{1,0} = \nu_0 k_B T \tau_0^2 / 2$ are the zero shear viscosity and first normal stress coefficient, respectively. Fig. 4-1 shows the steady state shear viscosity and first normal stress coefficient calculated from the anisotropic mobility model (Eqs. 4-12 and 4-13) with $\alpha = 9/11$. Under fast shear ($\tau_c \dot{\gamma} >> 1$), Eqs. 4-12 and 4-13 reduce to $\eta(\dot{\gamma}) \propto \dot{\gamma}^{-\alpha}$ and $\Psi_1(\dot{\gamma}) \propto \dot{\gamma}^{-2\alpha}$, which are consistent with experimentally observed behavior.[21)]

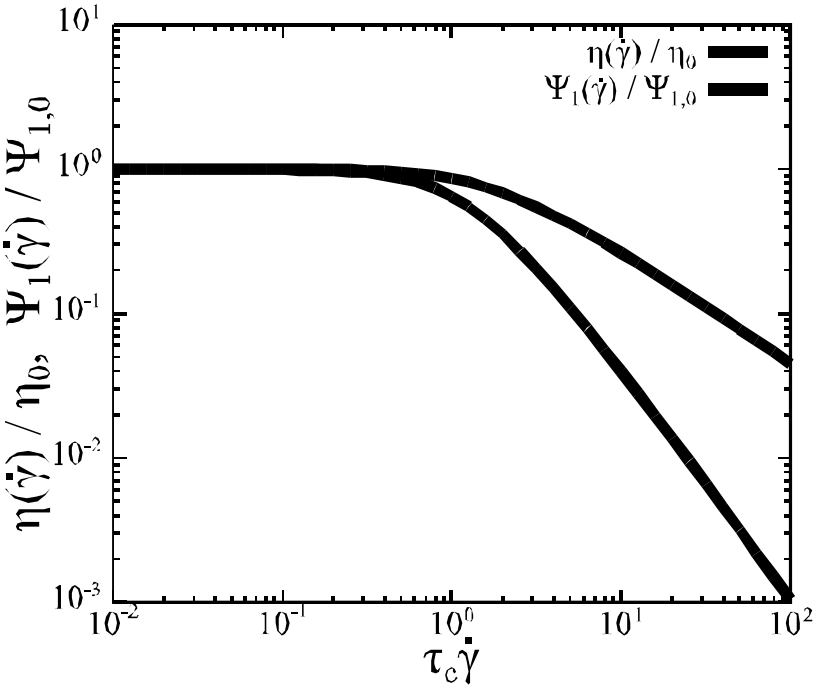

Fig. 4-1. The steady state shear viscosity and first normal stress coefficient, $\eta(\dot{\gamma})$ and $\Psi_1(\dot{\gamma})$, by the anisotropic mobility model for $\alpha = 9/11$ (an experimentally observed α value[21)]). η_0 and $\Psi_{0,1}$ represents the zero-shear viscosity and first normal stress coefficient, respectively.

4-3-2. Rheo-dielectric response

The rheo-dielectric response of the anisotropic mobility model can be calculated by using the Baiesi-Maes-Wynants formula,[16,17] a generalization of the Green-Kubo formula for non-equilibrium steady states. Baiesi-Maes-Wynants formula states that the response function in non-equilibrium steady state is expressed by the sum of two terms; the Green-Kubo term (which has the same form as the equilibrium case) and the frenetic term. At equilibrium, the frenetic term coincides to the Green-Kubo term and the equilibrium Green-Kubo formula is recovered.

The dielectric response function is the response of the electric flux density to the applied electric field. The electric flux density of a polymer with the type-A dipole in the *y*-direction is

$$D_y = 4\pi\nu m R_y \tag{4-14}$$

with m being the magnitude of effective dipole *per* unit segment, and ν, the chain number density. (For simplicity, the instantaneous response due to the fast dynamics and the Onsager correction factor are ignored here.) The physical quantity conjugate to the perturbation (the electric field) is the dipole in the *y*-direction, $P_y = mR_y$. Then, the Baiesi-Maes-Wynants formula gives the following expression of the rheo-dielectric function.

$$\varphi(t-t';\dot{\gamma}) = \frac{4\pi\nu m^2}{k_B T}\left[\frac{1}{2}\frac{d}{dt'}\left\langle R_y(t)P_y(t')\right\rangle_{\mathrm{ss},E=0} + \frac{1}{2}\frac{d}{dt'}\left\langle R_y(t)\frac{1}{\zeta_0}\frac{\partial F(\mathbf{R}(t'))}{\partial R_y(t')}\right\rangle_{\mathrm{ss},E=0}\right] \tag{4-15}$$

where the average $\langle\ldots\rangle_{\mathrm{ss},E=0}$ is taken under steady shear in the absence of the electric field.

This $\varphi(t-t';\dot{\gamma})$ can be evaluated as

$$\varphi(t';\dot{\gamma}) = \Delta\varepsilon_0 \frac{1}{\tau_0}\exp(-t/\tau_0) \tag{4-16}$$

where $\Delta\varepsilon_0 \equiv 4\pi\nu_0 m^2 \left\langle R^2 \right\rangle_{\mathrm{eq}} / k_B T$. The Fourier transform of eq (4-16) gives the dielectric response in the frequency domain, which is the single Debye form.

$$\varepsilon'(\omega;\dot{\gamma}) = \Delta\varepsilon_0 \frac{1}{1+(\omega\tau_0)^2}, \quad \varepsilon''(\omega;\dot{\gamma}) = \Delta\varepsilon_0 \frac{\omega\tau_0}{1+(\omega\tau_0)^2} \tag{4-17}$$

Eq. 4-16 means that *both the rheo-dielectric intensity and the rheo-dielectric relaxation time are independent of the shear rate*. Namely, the anisotropic mobility model predicts the insensitivity of the rheo-dielectric response to the shear rate, which is consistent with the experimental data for an entangled linear polyisoprene (PI) solution.[8] This is because the dynamic equation of R_y does not contain R_x, and thus it does not depend on the shear rate. It should be noted that the anisotropic mobility model predicts the shear thinning under fast shear; cf. Fig. 4-1. Thus, it can reproduce *the shear thinning of the shear viscosity and the shear rate independent rheo-dielectric response* simultaneously, without introducing further artificial mechanisms.

4-3-3. Parallel and perpendicular moduli

The parallel modulus is the linear response of the *xy*-component of the stress tensor to the *xy*-component of the strain tensor.[22-24] Similarly, the perpendicular modulus is the linear response of the *zy*-component of the stress tensor to the *zy*-component of the strain

tensor.[22-24] Because the perturbations in these cases cannot be expressed as the perturbation potentials, the Baiesi-Maes-Wynants formula cannot be utilized to calculate the parallel and perpendicular moduli. For such cases, the Seifert-Speck formula[18] can be utilized instead. The Seifert-Speck formula, being a generalization of the Baiesi-Maes-Wynants formula, states that the linear response function in the non-equilibrium steady state is expressed as the correlation function which involves the time derivative and the convection velocity.

For the anisotropic mobility model, the Seifert-Speck formula gives the following expressions for the parallel and perpendicular moduli (in the time domain).

$$G_{//}(\dot{\gamma};t-t') = \frac{1}{k_BT}\left\langle \hat{\sigma}_{xy}(\mathbf{R}(t))\left[R_y(t')\frac{1}{M_{xx}(\dot{\gamma})}\left[\frac{dR_x(t')}{dt'} + M_{xx}(\dot{\gamma})\frac{\partial F(\mathbf{R}(t'))}{\partial R_x(t')} - \dot{\gamma}R_y(t')\right]\right]\right\rangle_{ss} \tag{4-18}$$

$$G_{\perp}(\dot{\gamma};t-t') = \frac{1}{k_BT}\left\langle \hat{\sigma}_{zy}(\mathbf{R}(t))\left[R_y(t')\frac{1}{M_{zz}(\dot{\gamma})}\left[\frac{dR_z(t')}{dt'} + M_{zz}(\dot{\gamma})\frac{\partial F(\mathbf{R}(t'))}{\partial R_z(t')}\right]\right]\right\rangle_{ss} \tag{4-19}$$

Here, $\langle\cdots\rangle_{ss}$ stands for the average in the absence of the superposed sinusoidal strain. Eqs. 4-18 and 4-19 can be evaluated to give the following simple forms.

$$G_{//}(\dot{\gamma};t-t') = G_0\exp[-(1+\tilde{\lambda}(\dot{\gamma}))t/\tau_0] \tag{4-20}$$

$$G_{\perp}(\dot{\gamma};t-t') = G_0\exp[-2t/\tau_0] \tag{4-21}$$

Here, $G_0 \equiv \nu k_BT$ is the characteristic modulus, and τ_0 is the dielectric relaxation time appearing in Eq. 4-16. Eqs. 4-20 and 4-21 means that *the perpendicular modulus of the anisotropic*

mobility model is independent of the shear rate, while the parallel modulus depends on the shear rate rather strongly. The parallel and perpendicular relaxation times are given as $\tau_{//}(\dot{\gamma}) \equiv \tau_0/[1+\tilde{\lambda}(\dot{\gamma})]$ and $\tau_{\perp}=\tau_0/2$, respectively. The parallel relaxation time reduces as the shear rate increases, as the same way in the steady state shear viscosity. The Fourier transforms of Eqs. 4-20 and 4-21 give the storage and loss parallel and perpendicular moduli (in the frequency domain),

$$G_{//}'(\dot{\gamma};\omega) = G_0 \frac{\omega\tau_{//}(\dot{\gamma})}{1+[\omega\tau_{//}(\dot{\gamma})]^2}, \quad G_{//}''(\dot{\gamma};\omega) = G_0 \frac{[\omega\tau_{//}(\dot{\gamma})]^2}{1+[\omega\tau_{//}(\dot{\gamma})]^2} \tag{4-22}$$

$$G_{\perp}'(\dot{\gamma};\omega) = G_0 \frac{\omega\tau_0/2}{1+[\omega\tau_0/2]^2}, \quad G_{\perp}''(\dot{\gamma};\omega) = G_0 \frac{[\omega\tau_0/2]^2}{1+[\omega\tau_0/2]^2} \tag{4-23}$$

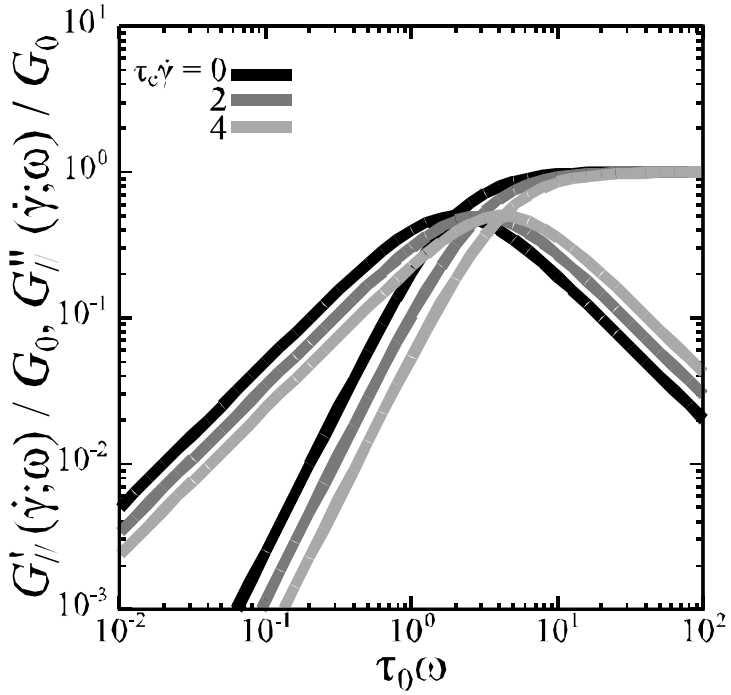

Fig. 4-2. The parallel storage and loss moduli, $G_{//}'(\dot{\gamma};\omega)$ and $G_{//}''(\dot{\gamma};\omega)$, by the anisotropic mobility model for $\alpha = 9/11$ (an experimentally observed α value[21]). G_0 and τ_0 are the characteristic modulus and equilibrium relaxation time. The shear rates are $\tau_c\dot{\gamma}$=0 (equilibrium), 2, and 4.

Fig. 4-2 shows the storage and loss parallel moduli of the anisotropic mobility model for $\alpha = 9/11$ and several different $\tau_c\dot{\gamma}$. (The characteristic time τ_c is taken to be identical to the dielectric τ_0.) The experimental studies showed that the parallel relaxation time is largely accelerated as increasing the shear rate, while the perpendicular relaxation time is only mildly accelerated.[22-24] Although the anisotropic mobility model cannot perfectly explain the experimental data, it can at least reproduce the different shear rate dependence for the parallel and perpendicular moduli, which is one of the essential points of the experimental data.

4-4. Discussion

4-4-1. Anisotropic mobility tensor

As shown above, the anisotropic mobility model can qualitatively explain experimental data, whereas the conventional convective CCR model fails. The CCR model assumes that the effective relaxation time of a chain is accelerated by applied shear flow,[12] and is similar to the anisotropic mobility model in a sense. However, the CCR model leads to the *isotropic* acceleration and is quite different from the anisotropic mobility model. This difference can be easily noted by rewriting the Langevin equation with the CCR effect in a form similar to that for the anisotropic mobility model. The original CCR model by Marrucci[12] reduces to the following mobility tensor model, together with Eqs. 4-7 and 4-8.

$$\mathbf{M}(\dot{\gamma}) = \left[\frac{1}{\zeta_0} + \frac{\beta_{\mathrm{CCR}}}{k_B T}\boldsymbol{\kappa}:\langle\mathbf{RR}\rangle\right]\mathbf{I} = \frac{1}{\zeta_0}\left[1 + \frac{\beta_{\mathrm{CCR}}\zeta_0\dot{\gamma}}{k_B T}\langle R_x R_y\rangle\right]\mathbf{I} \qquad (4\text{-}24)$$

where β_{CCR} is a parameter of the order of unity. (In the steady state under shear, $\langle R_x R_y \rangle$ is an odd function of $\dot{\gamma}$ which monotonically increases with $\dot{\gamma}$, and thus the mobility tensor **M** is an even function of $\dot{\gamma}$.) It is clear from Eq. 4-24 that the CCR model *isotropically accelerates* the dynamics of **R**.

From the viewpoint of the symmetry, such isotropic acceleration is possible. The symmetry argument requires that the mobility tensor is unchanged under certain transforms. If the shear rate is not large, the symmetry argument gives the following general form for the mobility tensor.

$$\mathbf{M}(\dot{\gamma}) = \frac{1}{\zeta_0}\left[\mathbf{I} + \tilde{L}_1(\boldsymbol{\kappa} + \boldsymbol{\kappa}^t) + \tilde{L}_2 \mathrm{tr}(\boldsymbol{\kappa}\cdot\boldsymbol{\kappa}^t) + \tilde{L}_3 \boldsymbol{\kappa}\cdot\boldsymbol{\kappa}^t + \tilde{L}_4 \boldsymbol{\kappa}^t\cdot\boldsymbol{\kappa} + ...\right] \qquad (4\text{-}26)$$

Here $\{\tilde{L}_k\}$ is the set of expansion coefficients. The anisotropic mobility model introduced in this Chapter is obtained by setting $\tilde{L}_1 = \tilde{L}_2 = \tilde{L}_4 = 0$, whereas the CCR model is obtained by setting $\tilde{L}_1 = \tilde{L}_3 = \tilde{L}_4 = 0$. Both models may belong to special cases of the non-equilibrium Langevin equation. Different forms may be also possible. For example, if $\tilde{L}_1$ is non-zero, the resulting Langevin equation has a kinetic coupling between the *x*- and *y*-components, which leads mild acceleration of the dielectric relaxation. The rheo-dielectric behavior of a star PI solution,[10] which show mild acceleration of the dielectric relaxation time, may be modeled by tuning the isotropic acceleration and/or the kinetic coupling. From these discussions, the anisotropic mobility tensor appears to be essential in non-equilibrium systems. By incorporating the anisotropic mobility into the detailed molecular models such as the tube

and sliplink models, and tuning the mobility tensor, the quantitative description for the dynamics of entangled polymers under shear may be possible.

4-4-2. Different shear rate dependence of linear response functions

The anisotropic mobility model predicts *anisotropic* acceleration of the relaxation dynamics of a polymer chain under fast shear. This is qualitatively different from the CCR model, which predicts the *isotropic* acceleration of the relaxation. The difference between the anisotropic and isotropic acceleration effects is worth detailed discussion.

The anisotropic acceleration of the dynamics might be suspected to be not realistic and physically inappropriate, even if it is allowed by the symmetry. Although the anisotropic acceleration may not be popular in the molecular models of polymers, it has been employed widely in the constitutive equation models to successfully reproducing various rheological properties of complex fluids. For example, the Giesekus model[25] and the Johnson-Segalman model[26] can be interpreted as the kinetic models that incorporate the conformation-dependent anisotropic mobility, and thus they predict the anisotropic acceleration. Although the molecular basis of the mobility in these constitutive models is not so clear, they can reproduce, at least qualitatively, the macroscopic rheological properties of complex fluids including polymer solutions. The success of the constitutive models with anisotropic mobility lends support to the validity of the anisotropic mobility tensor and the anisotropic acceleration.

Recently, Suzuki *et al*[27] reported the nonlinear rheological properties of an associating telechelic polymer aqueous solution. They measured the steady state shear viscosity and first normal stress coefficient of a telechelic polymer solution, reported that only the shear viscosity shows the shear thickening behavior, and proposed that the reassociation kinetics of telechelic polymers becomes anisotropic under fast shear. This result implies the universality of the anisotropic acceleration of polymer dynamics under shear and may support the validity of the anisotropic mobility model.

In the non-equilibrium statistical mechanics, the linear response function is considered to contain the information about the entropy production, which is a measure of the distance from the equilibrium.[14,15,19] Some generalized Green-Kubo relations contain terms which are directly related to the non-equilibrium entropy production characteristic to non-equilibrium systems. For example, the Lagrangian moving frame picture interprets the violation of the equilibrium Green-Kubo form as the result of the non-equilibrium entropy production. However, the rheo-dielectric response function of the anisotropic mobility model does not violate the equilibrium Green-Kubo form, and thus one *cannot analyze the non-equilibrium entropy production from the rheo-dielectric response function*. This is because the expression of the generalized Green-Kubo type relation strongly depends on the type of the applied perturbation. The situation becomes especially serious if the dynamics is anisotropic.

This example demonstrates that one linear response function is not sufficient to

understand the non-equilibrium polymer dynamics. Combination of several physical quantities such as various linear response functions and steady state viscosity is required.[3-7] As mentioned, the anisotropic mobility model is qualitatively consistent with the experimental data of a linear PI solution, and thus the situation is common for the analysis of experimental rheo-dielectric data.

4-5. Conclusion

In this Chapter, the non-equilibrium Langevin equation model for weakly entangled polymers, incorporating *anisotropic* mobility tensor (the anisotropic mobility model), was constructed and analyzed. The anisotropic mobility tensor was phenomenologically constructed with the symmetry argument and the diffusion data by simulations. In the anisotropic mobility model, the dynamics of a polymer is *anisotropically* accelerated, and both the shear thinning of the steady state viscosity and the shear rate insensitive rheo-dielectric response function are naturally reproduced. This is in contrast to the conventional CCR model, which incorporates the *isotropic* acceleration. The anisotropic mobility model can also reproduce the different shear rate dependence of the parallel and perpendicular moduli. These results suggest that the anisotropic acceleration is one of the essential features in the dynamics of polymers under fast shear.

References

1) D. J. Evans and G. P. Morris, Statistical Mechanics of Nonequilibrium Liquids, 2nd ed. (Cambridge University Press, Cambridge, 2008).

2) H. Risken, The Fokker-Planck Equation, 2nd ed. (Springer, Berlin, 2008).

3) H. Watanabe, Progress in Polymer Science, 24, 1253 (1999).

4) Y. Matsumiya, H. Watanabe, and K. Osaki, Macromolecules, 33, 499 (2000).

5) H. Watanabe, Y. Matsumiya, and K. Osaki, Journal of Polymer Science B: Polymer Physics, 38, 1024 (2000).

6) Y. Matsumiya and H. Watanabe, Macromolecules, 35, 2339 (2002).

7) H. Watanabe, Y. Matsumiya, and T. Inoue, Macromolecules, 35, 2339 (2002).

8) Y. Matsumiya, H. Watanabe, T. Inoue, K. Osaki, and M.-I. Yao, Macromolecules, 31, 7973 (1998).

9) H. Watanabe, T. Sato, Y. Matsumiya, T. Inoue, and K. Osaki, Nihon Reoroji Gakkaishi (Journal of the Society of Rheology, Japan) 27, 121 (1999).

10) H. Watanabe, S. Ishida, and Y. Matsumiya, Macromolecules, 35, 8803 (2002).

11) H. Watanabe, Y. Matsumiya, and T. Inoue, Journal of Physics: Condensed Matter, 15, S909 (2003).

12) G. Marrucci, Journal of Non-Newtonian Fluid Mechanics, 65, 241 (1996).

13) M. G. McPhie, P. J. Evans, I. K. Snook, J. Ennis, and D. J. Evans, Physica A 299, 412

(2000).

14) T. Harada and S. I. Sasa, Physical Review Letters, 95, 130602 (2005).

15) T. Speck and U. Seifert, Europhysical Letters, 74, 391 (2006).

16) M. Baiesi, C. Maes, and B. Wynants, Physical Review Letters, 103, 010602 (2009).

17) M. Baiesi, C. Maes, and B. Wynants, Journal of Statistical Physics, 137, 1094 (2009).

18) U. Seifert and T. Speck, Europhysical Letters, 89, 10007 (2010).

19) R. Chetrite, and G. Gawedzki, Journal of Statistical Physics, 137, 809 (2009).

20) T. A. Hunt and B. D. Todd, Journal of Chemical Physics, 131, 054904 (2009).

21) W. W. Graessley, Journal of Chemical Physics, 47, 1942 (1967).

22) K. Osaki, M. Tamura, M. Kurata, and T. Kotaka, Journal of Chemical Physics, 69, 4183 (1965).

23) J. Vermant, L. Walker, P. Moldenaers, and J. Mewis, Journal of Non-Newtonian Fluid Mechanics, 79, 173 (1999).

24) E. Somma, O. Valentino, G. Titomanlio, and G. Ianniruberto, Journal of Rheology, 51, 987 (2007).

25) H. Giesekus, Journal of Non-Newtonian Fluid Mechanics, 11, 69 (1982).

26) M. W. Johnson and D. Segalman, Journal of Non-Newtonian Fluid Mechanics, 2, 255 (1977).

27) S. Suzuki, T. Uneyama, T. Inoue, and H. Watanabe, Macromolecules, 45, 888 (2012).

Chapter 5. Rheo-Dielectric Responses of Entangled *cis*-Polyisoprene under Uniform Steady Shear and LAOS

5-1. Introduction

Nonlinear viscoelastic features of entangled polymers, for example, shear-thinning of viscosity under fast steady shear and nonlinear damping of relaxation modulus under large step strain, have been attributed to large orientation/stretch of the chain due to the flow/deformation and successive chain contraction, and dynamic models have been developed on the basis of this molecular picture,[1-11] as explained in Chapters 1 and 2. In the context of the widely utilized tube model, this nonlinear relaxation due to the contraction of convectively stretched chain is modeled as "convective constraint release (CCR)".[6-8] The nonlinear viscoelastic behavior, including the shear thinning of viscosity, is considerably well described by the refined tube model(s) incorporating the CCR mechanism.[7-9]

However, a problem(s) still remains for this description. The CCR mechanism itself accelerates the large-scale (global) motion/relaxation of the chain isotropically in all directions, but the rheo-dielectric behavior of the linear polyisoprene (PI) chains, detecting the end-to-end fluctuation in the shear gradient direction, is hardly affected by the shear flow in the thinning regime for the viscosity;[12] cf. Figs. 2-3 and 3-2. This fact suggests that the non-linear thinning of viscosity (and the other nonlinear features explained above) is not so straightforwardly related to the CCR mechanism, as discussed in Chapter 4.

In fact, the problem is more complicated *if* the steady shear is not uniform due to shear-banding and/or secondary flow. Such non-uniformity of flow has been reported for highly entangled melts/solutions at the shear rate $\dot{\gamma}$ exceeding the terminal relaxation frequency ω_G at equilibrium,[13-15] but the flow profile was not examined in the previous rheo-dielectric study[12] (reported earlier than Refs. 13-15). *If* the shear-banding occurs in the shear gradient direction, the rheo-dielectric data detect the harmonic average of the responses from PI in the fast and slow bands weighed by the volume fraction of respective bands. Then, the observed lack of the shear-induced acceleration of the data did not necessarily mean the lack of acceleration of the global motion *if* the fast band had just a small volume fraction and the chain dynamics in the slow band was close to the equilibrium dynamics. The same problem arises if the wall slippage occurs and/or a slipping place is formed in the material.

This problem of flow uniformity is revisited in this Chapter. Specifically, both rheo-dielectric behavior and flow profile were examined for an entangled solution of linear PI, and also for an entangled solution of star-branched PI for comparison. It turned out that the flow remained homogeneous (no shear-banding) in the shear-thinning regime examined ($\dot{\gamma} < 8.5/\tau_G$), but the shear effect on the rheo-dielectric behavior was less significant (negligible and just mild acceleration for linear and star PI, respectively, as noted previously[12]) compared to the effect on the viscosity. This Chapter presents details of these results and discusses the difference between the linear and star PI.

In addition, the rheo-dielectric behavior and flow profile of the linear and star PI solutions were also examined under large amplitude oscillatory strain (LAOS). The data for both linear and star PI suggested that the conformational distribution of the chains is coupled with LAOS and thus the rheo-dielectric response against a constant electric field is composed of a monotonically decaying part and an oscillating part. This result lends support to the analysis made in Chapter 3. The monotonic part of the rheo-dielectric response was rather insensitive to LAOS, which was consistent with the results obtained under steady shear. Details of these results are also presented in this Chapter.

5-2. Experimental

5-2-1. Materials.

Linear and 6-arm star-branched PI samples having high molecular weights (M) were utilized. The star PI sample was synthesized/fractionated/characterized in a previous study.[12] This sample, containing a small amount (~ 0.1 % to PI) of antioxidant, butylhydroxytoluene (BHT), has been sealed in Ar and kept in a deep freezer until use.

The linear PI sample was living-anionically polymerized in this study. Benzene and *s*-butyllithium were utilized as the polymerization solvent and initiator. The polymerized sample was fractionated twice from benzene/methanol mixtures, and a final benzene solution was dried in high vacuum at 50˚C for 2 days to recover the purified sample. A small amount

of BHT (~0.02 wt% to the PI sample) was added to the final benzene solution.

The linear PI sample thus obtained was characterized with GPC (CO-8020 and DP-8020; Tosoh) equipped with a refractive index (RI) monitor (RI-8020, Tosoh) and a low-angle laser light scattering (LALLS) detector (Viscotek 270, Malvern) connected in series: Its weight-average molecular weight M_w and polydispersity index M_w/M_n were evaluated from the LALLS/RI signal ratio measured at respective sections of elution volume. The elution solvent was tetrahydrofuran (THF), and monodisperse linear PI samples synthesized/characterized in the previous studies[16-18] were utilized as the RI/LALLS standards. The GPC trace was also examined for the previously synthesized star PI sample[12] to confirm lack of degradation during the storage.

Table 5-1 summarizes the molecular characteristics of the linear and star PI samples thus determined. The materials subjected to rheo-dielectric measurements under steady shear and large amplitude oscillatory strain (LAOS) were solutions of linear and star PI samples in an oligomeric butadiene (oB2; Nisseki PB2000 obtained from Nisseki Co; 1,2-vinyl:1,4-cis/trans = 83:17, $M_w = 2\times10^3$, $M_w/M_n \cong 2$).[12,19] The PI concentration was 5 and 20 wt% for the linear and star PI solutions, respectively. These solutions were prepared by firstly dissolving prescribed masses of PI and oB2 samples in benzene (at a concentration ~ 5 wt%) and then allowing benzene to thoroughly evaporate, firstly in ambient condition for 1 day and then in high vacuum at 50˚C for 2 days. In addition to the neat PI/oB2 solutions, solutions

containing a small amount (600 ppm wt/wt in the solution) of hollow silica particles with the diameter of ≅ 10 μm (HGS-10, Deantec Dynamic) were also prepared with the same method. These particles served as the tracer for detecting the shear velocity profile in the samples, as in the experiment by Wang et al.[14)]

Table 5-1. Molecular characteristics of PI samples

	$10^{-4}M_w$	M_w/M_n
Linear PI	144	1.12
Star PI[a]	17.9 (for arm)	1.03

a: synthesized/characterized in Ref.12.

5-2-2. Measurements.

5-2-2a. dielectric measurements.

For the linear and star PI solutions in oB2 containing *no* tracer particles, dielectric measurements were conducted with an impedance analyzer/dielectric interface system (1260 and 1296; Solartron) and a homemade circuit, the latter being comprising of a function generator (1941, Wave Factory), an electrometer (6485 Picoammeter, Keithley), and a digital recorder (DL708E, Yokogawa). (No dielectric measurement was attempted for the solution containing the particles because the particles introduced ionic impurities to disturb the measurements.) The former system was utilized for measurements under a sinusoidal electric field (at angular frequencies $\omega = 0.1\text{-}10^5$ s^{-1}), and the latter circuit, for measurements under rectangular electric field on the basis of the adsorption current (AdC) method reported

in literature.[12,20-22)]

The measurements utilized cone and plate electrodes mounted on a laboratory rheometer (ARES, TA Instruments). Fig. 5-1 schematically shows the structure of the electrodes. The electrodes, made with stainless steel, were designed/machined in the previous study.[12)] The plate radius was r_p = 2.5 cm, and the gap angle between the cone and plate was θ_{cp} = 2.0°. The cone had a truncated head to avoid contact with the plate electrode (counter electrode). The cone and plate electrodes were attached to the driving shaft and the torque detector of the rheometer, respectively. Thus, the cone electrode rotated during the rheo-dielectric measurements under steady shear, whereas the plate electrode was fixed. The inner part and outer edge of the cone, mutually insulated by a teflon block, served as the main and guard electrodes, and the inner (main) electrode was connected to a metallic contact ring immersed in a mercury reservoir so that the rotation of this electrode did not disturb the measurement: The impedance analyzer/dielectric interface system and the homemade circuit explained above were connected to the mercury reservoir, and the rotation of the contact ring in this reservoir gave negligibly small electrical noise for

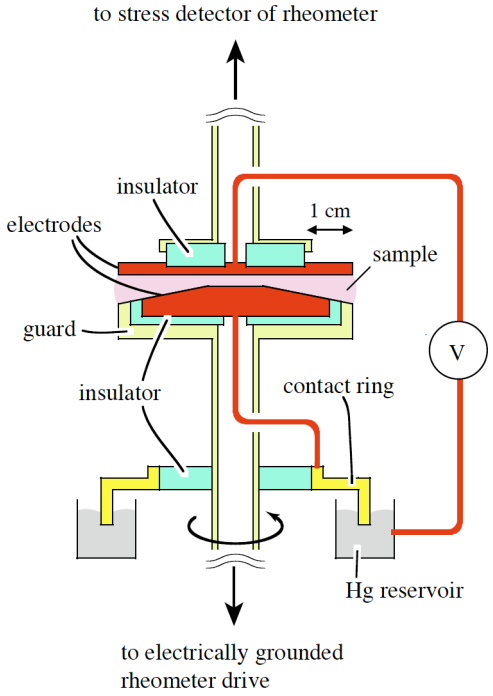

Fig. 5-1. Schematic illustration of cone and plate electrodes mounted on a rheometer.[12)]

the signal from the sheared samples. The electrical contact to the counter electrode (plate electrode) was made with a thin coaxial wire that did not disturb the stress measurement (for the stress > 10 Pa).

The rheo-dielectric measurements under steady shear flow and large amplitude oscillatory shear strain (LAOS) were conducted with the AdC method for the linear and star PI solutions at reference temperatures T_r = 23˚C and 18˚C (room temperature), respectively.

The measurements at equilibrium (no flow/LAOS) were made with the AdC method at these T_r and also with the standard method (utilizing the sinusoidal electric field) at several temperatures including those T_r. Time-temperature superposition was valid, and the data obtained with the standard method were reduced at T_r.

***5-2-2b. particle tracking velocimetry*:**[14] The PI/oB2 solutions containing the tracer particles were subjected to the steady shear/LAOS in the cone-and-plate geometry (electrodes) explained above. The local velocity profile therein was determined by tracing the particles with a high-speed video camera (VW-6000, Keyence Corporation). The camera was set just beside the cone-and-plate geometry, and its focus was placed on the geometry edge to record the trajectories of the particles nearby the edge. The video images of those particles were digitized to determine the particle position h (height in the cone-and-plate gap measured from the plate surface) and the velocity υ in the shear direction. The viscoelastic data explained

below were indistinguishable for the solutions with and without particles because the particles were dilute. Thus, the velocity profile of the particles was utilized as the flow profile in the particle-free solutions.

***5-2-2c. rheological measurements*:** For the linear and star PI/oB2 solutions at respective reference temperatures, T_r = 23 and 18˚C, steady shear and LAOS measurements were conducted with the cone-and-plate geometry (electrodes) mounted on the rheometer. These rheological measurements were made for the solutions with and without the tracer particles, and the rheo-dielectric measurement was simultaneously conducted for the particle-free solutions. The rheological data agreed for the solutions with and without the particles. Thus, the dilute tracer particles had no detectable effect on the rheological behavior of the solutions, and quite possibly no effect on the flow profile as well. For this reason, the velocity profile of the particles was utilized as the flow profile in the particle-free solutions for which the rheo-dielectric behavior was examined.

For comparison, the above rheological measurements were made also with a smaller cone-plate geometry (standard accessory of ARES) having the radius r_p = 1.25 cm and the gap angle θ_{cp} =5.73˚ (0.1 rad). The rheological data obtained with this geometry agreed with those from the large geometry utilized for the rheo-dielectric measurements, confirming accuracy of the data obtained with the latter geometry. In addition, dynamic viscoelastic

measurements at a small strain amplitude (γ_0 = 0.1 in the linear response regime) were made for the particle-free solutions at several temperatures including the reference temperature T_r explained above. The time-temperature superposition was valid for the storage and loss moduli G' and G'' thus measured, and the shift factor a_T was identical to that obtained for the dielectric data. These moduli data were reduced/compared at T_r.

5-3. Analysis of Data in Linear Regime.

Under small strain and weak electric field, any material (including the PI solutions examined in this Chapter) exhibits linear responses. In particular, under a small-amplitude sinusoidal strain oscillating at an angular frequency ω, $\gamma(t) = \gamma_0 \sin \omega t$, the linear viscoelastic responses are characterized with the storage and loss moduli $G'(\omega)$ and $G''(\omega)$ explained in Chapter 2 (cf. Eqs. 2-9 and 2-11). Similarly, the linear responses against a weak sinusoidal electric field $E(t) = E_0 \sin \omega t$ are characterized with the decrease of dynamic dielectric constant $\Delta\varepsilon'(\omega)$ $(= \varepsilon'(0) - \varepsilon'(\omega))$ and dielectric loss $\varepsilon''(\omega)$ (cf. Eqs. 2-10 and 2-12). These linear responses are intimately related to the relaxation spectra (cf. Eqs. 2-13 and 2-14), and they exhibit the characteristic power-law behavior at low ω where all relaxation processes are completed; $G'(\omega)$, $\Delta\varepsilon'(\omega) \propto \omega^2$ and $G''(\omega)$, $\varepsilon''(\omega) \propto \omega$ at such low ω (cf. Eqs. 2-15 and 2-16). The terminal viscoelastic and dielectric relaxation times τ_G and τ_ε, defined as the second-moment average relaxation times,[23] are evaluated from the

data in this power-law regime (flow regime), as explained for Eq. 2-17:

$$\tau_G = \left[\frac{G'(\omega)}{\omega G''(\omega)}\right]_{\omega\to 0}, \quad \tau_\varepsilon = \left[\frac{\Delta\varepsilon'(\omega)}{\omega\varepsilon''(\omega)}\right]_{\omega\to 0} \tag{5-1}$$

In contrast, under fast shear at a rate $\dot{\gamma}$ well above the linear viscoelastic relaxation frequency $1/\tau_G$, the molecular motion in the liquid is highly disturbed and significant nonlinearity prevails. This nonlinearity is characterized, for example, by the steady state viscosity defined in terms of the steady state stress σ_{ss} as

$$\eta(\dot{\gamma}) = \frac{\sigma_{ss}(\dot{\gamma})}{\dot{\gamma}} \tag{5-2}$$

5-4. Analysis of Rheo-dielectric Data in Nonlinear Regime.

Either in the absence or presence of fast steady shear flow, any material (including PI) exhibits "linear" dielectric responses against a weak electric field (superposed on the steady flow). It should be noted, however, that those linear dielectric responses do not reflect the equilibrium dynamics if the dielectric data are obtained under fast steady shear, as discussed in Chapters 3 and 4.

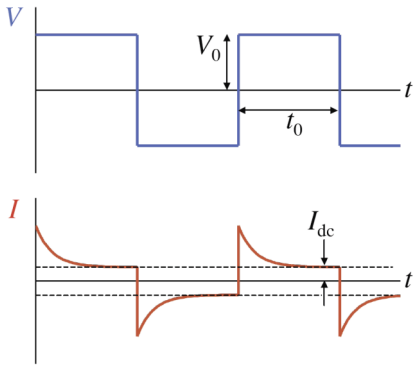

Fig. 5-2. Schematic illustration of voltage and current in AdC method.

In the experiments with the adsorption current (AdC) method,[12,20-22] a rectangular voltage $V(t)$ is applied to a material, and the resulting current $I(t)$ is measured, as schematically shown in Fig. 5-2. The voltage has the Fourier components specified by[20]

$$V(t) = V_0 \sum_{p=\text{odd}} \frac{4}{p\pi} \sin\omega_p t \qquad (5\text{-}3)$$

where $\omega_p = p\pi/t_0$ is the angular frequency of pth component determined by the half-period t_0 of the voltage; cf. Fig. 5-2. The linear response to this $V(t)$ is the current $I(t)$ that is contributed from motion of ionic impurities giving the dc current I_{dc} and from motion of dipoles in the system giving the relaxational current $I_{relax}(t)$. (In this study, a method of ion removal through adsorption on a freshly baked glass wall[24] was employed to minimize I_{dc}.)

The $I_{relax}(t)$ data (= $I(t)$ - I_{dc}), given by a convolution of the electric field ($\propto V(t)$) and the normalized dielectric relaxation function $\Phi(t)$, are compactly written as[20]

$$I_{relax}(t) = \frac{4V_0C_0}{t_0}\left[\varepsilon_\infty \sum_{p=\text{odd}} \cos\omega_p t - \Delta\varepsilon \int_0^\infty \frac{d\Phi(t')}{dt'} \sum_{p=\text{odd}} \cos\omega_p (t-t') dt'\right] \qquad (5\text{-}4)$$

where C_0 is the vacant capacitance of the dielectric cell (cone and plate electrodes; cf. Fig. 5-1), ε_∞ is the high-frequency dielectric constant, and $\Delta\varepsilon$ is the dielectric relaxation intensity. (This $I_{relax}(t)$ corresponds to the time-derivative of the polarization, $dP(t)/dt$, discussed in Chapter 3.) On the basis of Eq. 5-4, the dynamic dielectric constant (permittivity) $\varepsilon'(\omega)$ and dielectric loss $\varepsilon''(\omega)$, that are usually measured with a standard method utilizing the sinusoidal voltage, can be obtained through the Fourier integral of $I_{relax}(t)$:[20]

$$\varepsilon'(\omega_p) = \frac{1}{2V_0C_0} \int_0^{t_0} I_{relax}(t) \cos\omega_p t \, dt \qquad (5\text{-}5a)$$

$$\varepsilon''(\omega_p) = \frac{1}{2V_0C_0} \int_0^{t_0} I_{relax}(t) \sin\omega_p t \, dt \qquad (5\text{-}5b)$$

The same information can be obtained by measuring the $I_{\mathrm{relax}}(t)$ data for sufficiently long time (until it decays below the experimental resolution and $I(t)$ coincides with the t-independent I_{dc}) and then decomposing the $I_{\mathrm{relax}}(t)$ data into exponential relaxation modes as[20)]

$$I_{\mathrm{relax}}(t) = 2V_0 C_0 \Delta\varepsilon \sum_{p\geq 1} \frac{h_p}{\tau_{\varepsilon,p}} \exp\left(-\frac{t}{\tau_{\varepsilon,p}}\right) = Q_{\mathrm{relax}} \sum_{p\geq 1} \frac{h_p}{\tau_{\varepsilon,p}} \exp\left(-\frac{t}{\tau_{\varepsilon,p}}\right) \tag{5-6}$$

with

$$Q_{\mathrm{relax}} = \int_0^{t_0} I_{\mathrm{relax}}(t)\,\mathrm{d}t \left(= \int_0^{\infty} I_{\mathrm{relax}}(t)\,\mathrm{d}t\right) \tag{5-7}$$

The mode relaxation time $\tau_{\varepsilon,p}$ and the normalized mode intensity h_{p} (satisfying $\Sigma_p h_p = 1$) obtained from the above decomposition coincide with those defined in Chapter 2 (cf. Eqs. 2-14), so that $\varepsilon'(\omega)$ and $\varepsilon''(\omega)$ are expressed as

$$\{\varepsilon'(0) - \varepsilon'(\omega)\} + i\varepsilon''(\omega) = \Delta\varepsilon \sum_{p\geq 1} h_p \frac{\omega^2\tau_{\varepsilon,p}^2 + i\omega\tau_{\varepsilon,p}}{1+\omega^2\tau_{\varepsilon,p}^2} \quad (i=\sqrt{-1}) \tag{5-8}$$

(In this study, $\varepsilon'(\omega)$ and $\varepsilon''(\omega)$ at equilibrium/under steady shear flow were evaluated on the basis of either Eq. 5-5 or Eq. 5-8. The data obtained with these two methods were found to coincide with each other.)

The situation is a little different under large amplitude oscillatory strain (LAOS). The analysis in Chapter 3 suggested that the relaxational current $I_{\mathrm{relax}}(t)$ against a constant electric field exhibits oscillatory decay. Indeed, this oscillatory decay was confirmed from experiments. Thus, the $I_{\mathrm{relax}}(t)$ data under LAOS could not be decomposed into the

exponentially decaying modes in a way shown in Eq. 5-6. Such features of the $I_{relax}(t)$ data are discussed in more detail later in section 5-5-4a.

5-5. Results and Discussion

5-5-1. Overview of data in linear regime

In the PI/oB2 solutions examined, the number of entanglements *per* linear PI chain and/or span (two arms) of the star PI are evaluated as[3)]

$$N = M/(M_e^\circ/\phi^{1.3}) \cong 5.9 \text{ for linear PI (in 5 wt\% solution)} \quad (5\text{-}9a)$$

$$N_{span} = 2M_{arm}/(M_e^\circ/\phi^{1.3}) \cong 8.8 \text{ for star PI (in 20 wt\% solution)} \quad (5\text{-}9b)$$

where M_e° denotes the entanglement molecular weight of bulk PI (= 5×10^3)[25)] and ϕ is the volume fraction of PI in the solution. Thus, in the solutions the linear and star PI chains were in a moderately entangled state.

For these linear and star PI solutions at T_r = 23 and 18˚C, respectively, Figs. 5-3 and 5-4 show double logarithmic plots of the linear viscoelastic storage and loss moduli, $G'(\omega)$ and $G''(\omega)$, the decrease of the dynamic dielectric constant from the static permittivity, $\Delta\varepsilon'(\omega) \equiv \varepsilon'(0)-\varepsilon'(\omega)$, and the dielectric loss $\varepsilon''(\omega)$ against the angular frequency ω. The filled and unfilled circles, respectively, indicate the dielectric data obtained with the standard method (utilizing the sinusoidal electric field) and with the adsorption current (AdC) method (utilizing the rectangular electric field) explained earlier. With the latter method, the

relaxational current $I_{relax}(t)$, obtained by subtracting a direct current contribution due to ionic impurities, was Fourier-transformed to give $\Delta\varepsilon'(\omega)$ and $\varepsilon''(\omega)$. (The $I_{relax}(t)$ data are later shown in Figs. 5-15 and 5-16.) These $\Delta\varepsilon'(\omega)$ and $\varepsilon''(\omega)$ data agree well with the data obtained with the standard method.

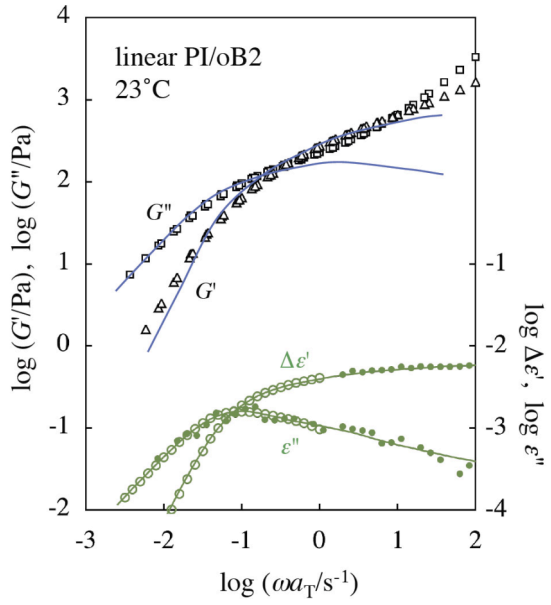

Fig. 5-3. Viscoelastic and dielectric behavior of linear PI/oB2 solution (5 wt%) at 23˚C. Thin blue curves indicate the viscoelastic moduli calculated from the dielectric data on the basis of full-DTD relationship.

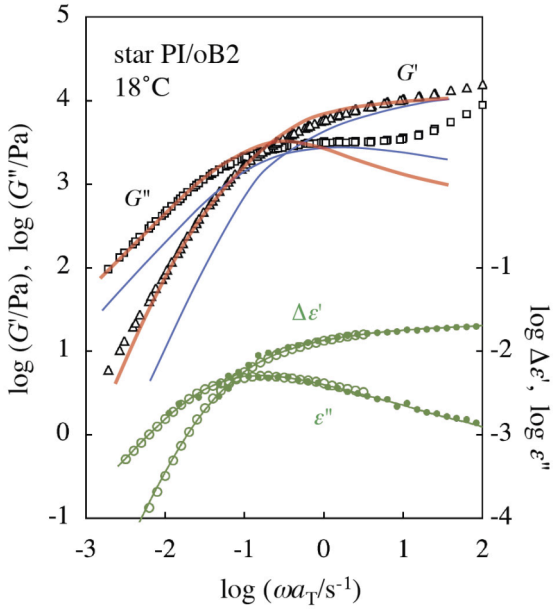

Fig. 5-4. Viscoelastic and dielectric behavior of star PI/oB2 solution (20 wt%) at 18˚C. Thin blue and thick red curves, respectively, indicate the viscoelastic moduli calculated from the dielectric data on the basis of full-DTD and partial-DTD relationships.

As explained in section 5-3, the linear viscoelastic and dielectric data shown in Figs. 5-3 and 5-4 exhibit the flow behavior characterized with the power-law behavior at sufficiently low ω, $G'(\omega), \Delta\varepsilon'(\omega) \propto \omega^2$ and $G''(\omega), \Delta\varepsilon''(\omega) \propto \omega$. The second-moment average viscoelastic relaxation time (cf. Eq. 5-1) is evaluated from these power-law tails as

$$\tau_G(0) = 22 \text{ s for linear PI}, \quad \tau_G(0) = 34 \text{ s and star PI} \qquad (5\text{-}10)$$

where "(0)" explicitly shows that the relaxation time was evaluated in the linear regime. If the steady shear is applied at rates $\dot{\gamma} > 1/\tau_G(0)$, the dynamics of the PI chains deviates from equilibrium to prevail significantly nonlinear viscoelastic behavior, as discussed later Fig. 5-9.

5-5-2. Test of molecular picture of dynamic tube dilation for data in linear regime

Because the PI chains have type-A dipoles parallel along the chain backbone, their normalized dielectric relaxation $\Phi(t)$ in the linear regime is given by the auto-correlation functions, as explained in Chapters 2-4:[23,26,27)]

$$\Phi(t) = \frac{\left\langle R_y(t)R_y(0)\right\rangle_{eq}}{\left\langle R_y^2\right\rangle_{eq}} \quad \text{(for linear PI)} \tag{5-11}$$

$$\Phi(t) = \frac{\sum_{\alpha,\alpha'=1}^{q}\left\langle R_{arm,y}^{[\alpha]}(t)R_{arm,y}^{[\alpha']}(0)\right\rangle_{eq}}{q\left\langle R_{arm,y}^2\right\rangle_{eq}} \quad \text{(for } q\text{-arm star PI)} \tag{5-12}$$

Here, $R_y(t)$ indicates the component of the end-to-end vector of the linear chain in the direction of the electric field (chosen to be y direction), and $<\cdots>_{eq}$ specifies the ensemble average at equilibrium (in the absence of the electric field). $R_{arm,y}^{[\alpha]}(t)$ denotes the y component of the end-to-branching point vector of αth arm of the star chain (composed of q arms). The terminal viscoelastic relaxation reflects the decay of the orientational anisotropy throughout the chain backbone (cf. Eq. 2-1). Thus, the large-scale motion of linear/star PI chains activates the dielectric relaxation in the same range of frequency as that for the viscoelastic relaxation, as confirmed in Figs. 5-3 and 5-4.

Despite this similarity in the relaxation time scale of the viscoelastic and dielectric data, there is an important difference between these data. Namely, the normalized viscoelastic relaxation function $\mu(t)$ (= $G(t)/G_0$) reflects the *isochronal* orientational anisotropy of the subchains (cf. Eq. 2-1), whereas the dielectric $\Phi(t)$ detects orientational correlation of all subchains at two times (t and 0; cf. Eqs. 5-11 and 5-12). Thus, the chain motion is differently averaged in $\mu(t)$ and $\Phi(t)$, which leads to lack of a unique relationship between $\mu(t)$ and $\Phi(t)$.[16,17,28-30)]

This lack of uniqueness in turn means that the chain dynamics can be characterized through a particular relationship between $\mu(t)$ and $\Phi(t)$ experimentally observed for PI chains. Specifically, for entangled chains, a simple analysis of chain conformation specifies several characteristic relationships according to magnitudes of the dynamic tube dilation (DTD) considered in the tube model:[16,17,28-30)]

(i) *For no DTD:* $\mu(t) = \Phi(t)$ (5-13)

(ii) *For full DTD*: $\mu(t) = \{\varphi'(t)\}^{1+d} \cong \{\Phi(t)\}^2$ ($d \cong 1.3$ for PI) (5-14a)

with $\varphi'(t) = \Phi(t) + \frac{1}{N'}\left[\{\varphi'(t)\}^{-d/2} - 1\right]^2$ (5-14b)

($N' = 4N$ and $8N_{\rm arm}$ for linear and star PI)

(iii) *For partial DTD*:

$\mu(t) = \varphi'(t)/\beta(t)$ (5-15a)

with $\varphi'(t) = \Phi(t) + \frac{1}{N'}\left[\{\beta(t)\}^{1/2} - 1\right]^2$ (5-15b)

($N' = 4N$ and $8N_{\rm arm}$ for linear and star PI)

The viscoelastic $\mu(t)$ and dielectric $\Phi(t)$ coincide with each other if the constraint release

(CR) mechanism is quenched to activate no DTD; cf. Eq. 5-13. The dynamics of dilute probe chains in a matrix of much longer chain is known to fall in this case.[28)]

On the other hand, the DTD process is undoubtedly activated if the CR mechanism is not quenched. Specifically, the relaxed portions of the chains behave as a "solvent" to fully loosen the entanglement constraint to a level expected for a solution in this "solvent", *if* the chain rapidly explores all local conformations within a length scale of the dilated tube diameter $a_{\text{full-DTD}}$ in this solution. For this case of full-DTD, the tube survival fraction $\varphi'(t)$ determines the dilated tube diameter as $a_{\text{full-DTD}} = a\{\varphi'(t)\}^{-d/2}$ (with a being the diameter of undilated tube), thereby giving $\mu(t) = \{\varphi'(t)\}^{1+d}$ (Eq. 5-14a) with the dilation exponent $d \cong 1.3$ for PI. $\varphi'(t)$ is in turn related to the dielectric $\Phi(t)$ through Eq. 5-14b. The second term in RHS of Eq. 5-14b, involving the number of entanglements *per* linear chain N and/or *per* arm of the star chain N_{arm}, represents a minor correction for the dielectric relaxation activated by the chain fluctuation at the edges of the surviving portion of the dilated tube.[16,17,29)] This correction becomes important only in the terminal relaxation regime at long t, and $\varphi'(t)$ essentially coincides with $\Phi(t)$. Consequently, $\mu(t)$ is numerically close to $\{\Phi(t)\}^2$ (cf. Eq. 5-14a) in the entire range of t, as shown later in Fig. 5-5.

If the chain cannot explore, in time, all local conformations within the length scale of $a_{\text{full-DTD}}$, the tube diameter does not effectively increase to $a_{\text{full-DTD}}$. For this case of partial-DTD, the tube dilates to $a_{\text{partial-DTD}} = a\{\beta(t)\}^{1/2}$ ($< a_{\text{full-DTD}}$), where the number of

entanglement segments $\beta(t)$ corresponding to $a_{\text{partial-DTD}}$ is determined by competition of the CR mechanism with the other mechanisms of chain motion along the tube such as reptation/arm retraction. In general, $\beta(t)$ specifies the upper bound of spatial coarse-graining in a given time scale, and $\beta(t)$ coincides with $\{\varphi'(t)\}^{-d}$ if the CR mechanism allows the tube to fully dilate to $a_{\text{full-DTD}}$ in the sense explained above. The viscoelastic $\mu(t)$ for partial-DTD is given by Eq. 5-15a, where the tube survival fraction $\varphi'(t)$ is evaluated from $\beta(t)$ and the dielectric $\Phi(t)$ (cf. Eq. 5-15b). The second term in RHS of Eq. 5-15b gives the minor correction explained above, and $\varphi'(t)$ essentially coincides with $\Phi(t)$ also in the case of partial-DTD.

$G^*(\omega)$ and $\Delta\varepsilon^*(\omega)$ in the frequency domain are equivalent to the relaxation functions $\mu(t)$ and $\Phi(t)$ in the time domain. Thus, the dynamics of the linear and star PI chains in the oB2 solutions can be assigned to one of the three cases explained above through comparison of the $G^*(\omega)$ and $\Delta\varepsilon^*(\omega)$ data. Figs. 5-3 and 5-4 clearly show differences in the ω dependence of the $G^*(\omega)$ and $\Delta\varepsilon^*(\omega)$ data. Thus, without any further analysis, the data lead to a conclusion that the DTD process activated by the CR mechanism contributes to the relaxation of both linear and star PI chains.

The $\Delta\varepsilon^*(\omega)$ data shown in Figs. 5-3 and 5-4 were subjected to inverse Fourier transformation to give $\Phi(t)$. $\Delta\varepsilon^*(\omega)$ re-calculated from this $\Phi(t)$, shown in Figs. 5-3 and 5-4 with the thin green curves, agree well with the $\Delta\varepsilon^*(\omega)$ data (green plots), indicating a

satisfactory accuracy of $\Phi(t)$ thus obtained. This $\Phi(t)$ was utilized in Eq.5-14b to calculate $\varphi'(t)$ for the case of full-DTD through the iteration method reported in literature.[16] Furthermore, $\varphi'(t)$ is utilized in Eq. 5-14a to evaluate $\mu_{\text{f-DTD}}(t)$ (= $\{\varphi'(t)\}^{1+d}$). As an example, $\mu_{\text{f-DTD}}(t)$ for star PI is shown in Fig. 5-5 (small blue dots). This $\mu_{\text{f-DTD}}(t)$ is numerically close to the squared dielectric relaxation function (large green squares), as already explained for Eq. 5-14a.

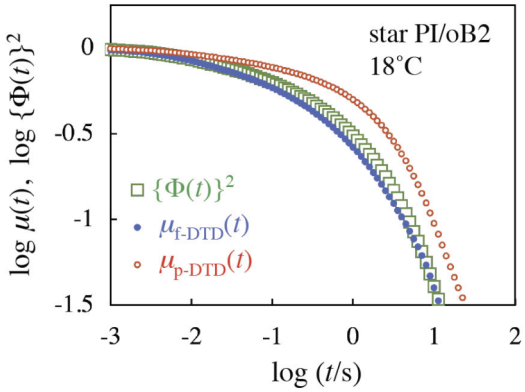

Fig. 5-5. Comparison of normalized viscoelastic relaxation function for the cases of full- and partial-DTD, $\mu_{\text{f-DTD}}(t)$ and $\mu_{\text{p-DTD}}(t)$, with squared dielectric relaxation function, $\{\Phi(t)\}^2$, for star PI (20 wt%) in the oB2 solution at 18°C.

In Figs. 5-3 and 5-4, $G_{\text{f-DTD}}^*(\omega)$ for the case of DTD, calculated from $\mu_{\text{f-DTD}}(t)$ (Eq. 2-11 with G_0 being replaced by the entanglement modulus G_N), are shown with the thin blue curves. For linear PI (Fig. 5-3), $G_{\text{f-DTD}}^*(\omega)$ is close to the $G^*(\omega)$ data, except at high ω (> 1 s^{-1}) where the local Rouse relaxation within the entanglement segment (not considered in Eq. 5-14) significantly contributes to the data. In contrast, for star PI (Fig. 5-4), $G_{\text{f-DTD}}^*(\omega)$ significantly deviates from the $G^*(\omega)$ data in the dominant part of the terminal relaxation at low ω (< 1 s^{-1}). Thus, the full-DTD relationship is valid for linear PI but not for star PI, which is in harmony with the conclusion for bulk PI reported in literature.[16,17,28-30]

A test of partial-DTD relationship (eq. 5-15) requires data for the dielectric CR relaxation

time $\tau_{CR}^{[\varepsilon]}$. The $\tau_{CR}^{[\varepsilon]}$ data for monodisperse systems, to be evaluated from extrapolation of $\tau_{CR}^{[\varepsilon]}$ data for binary blends, are not available for the 20 wt% solution of star PI in oB2. Nevertheless, the viscoelastic $\tau_{CR}^{[G]}$ data for monodisperse star PI in bulk suggest that $\tau_{CR}^{[G]}$ is close to twice of the measured terminal viscoelastic relaxation time τ_G for star PI having $N_{span} = 2N_{arm} \cong 9$, as noted from Fig. 9 of Ref. 30. For the Rouse CR process, the viscoelastic and dielectric CR times satisfy a relationship $\tau_{CR}^{[\varepsilon]} = 2\tau_{CR}^{[G]}$, as explained in Chapter 2. Thus, for the star PI chain in the oB2 solution having $N_{span} \cong 8.8$, the best estimate was obtained as $\tau_{CR}^{[\varepsilon]} \cong 4\tau_G(0) \cong 136$ s (cf. Eq. 5-10). With this estimate of $\tau_{CR}^{[\varepsilon]}$, the Rouse-CR function $\psi_{CR}(t)$ and the maximum possible number of CR-equilibrated entanglement segments $\beta_{CR}(t)$ (= $1/\psi_{CR}(t)$) were calculated for the star PI solution, as did in literature.[29] (For simplicity, the intrinsic Rouse fluctuation considered in literature[29] was not involved in the current calculation.) Fig. 5-6 compares this $\beta_{CR}(t)$ with $\beta_{full\text{-}DTD}(t)$ (= $\{\varphi'(t)\}^{-d}$), the latter being obtained in the calculation of $\mu_{f\text{-}DTD}(t)$ for the case of full-DTD. Clearly, $\beta_{full\text{-}DTD}(t)$ exceeds $\beta_{CR}(t)$ in the entire range of t up to $\tau_G(0)$, meaning that the CR mechanism does not allow the tube for the star PI chain to dilate up to the diameter assumed in the full-DTD picture.

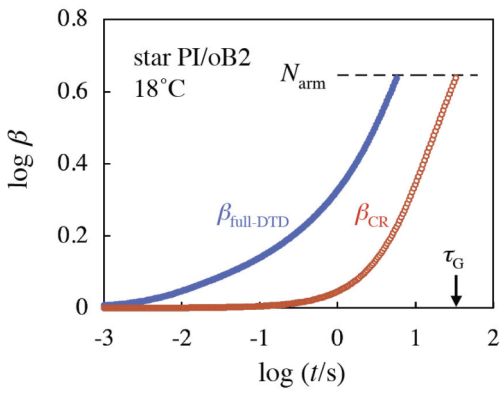

Fig. 5-6. Comparison of the maximum possible number of entanglement segments of star PI that can be CR-equilibrated in time, $\beta_{CR}(t)$, and the number of segments coarse-grained in the case of full-DTD, $\beta_{full\text{-}DTD}(t)$.

This result explains why the full-DTD relationship fails for star PI (cf. thin blue curves in Fig. 5-4). In contrast, for linear PI, $\beta_{\text{full-DTD}}(t)$ did not exceed $\beta_{\text{CR}}(t)$ (results not shown here) to ensure validity of the full-DTD relationship.

For star PI, $\mu_{\text{p-DTD}}(t)$ for the partial-DTD process was obtained from Eq. 5-15a with $\beta(t)$ therein being replaced by $\beta_{\text{CR}}(t)$ shown in Fig. 5-6. ($\varphi'(t)$ was re-evaluated from this $\beta_{\text{CR}}(t)$ and the dielectric $\Phi(t)$ data; cf. Eq. 5-15b.) This $\mu_{\text{p-DTD}}(t)$, shown in Fig. 5-5 with red circles, relaxes slowly compared to $\mu_{\text{f-DTD}}(t)$. This slow relaxation of $\mu_{\text{p-DTD}}(t)$ partly results from rather slow growth of $\beta_{\text{CR}}(t)$ (that reaches the number of entanglements per arm, N_{arm}, at $t \sim \tau_{\text{G}}(0)$; cf. Fig. 5-6.) In Fig. 5-4, $G_{\text{p-DTD}}^*(\omega)$ calculated from $\mu_{\text{p-DTD}}(t)$ is shown with the thick red curves. This $G_{\text{p-DTD}}^*(\omega)$ agrees well with the $G^*(\omega)$ data, except at high ω (> 1 s^{-1}) where the local Rouse relaxation (not considered in Eq. 5-15) significantly contributes to the data. Thus, the partial-DTD relationship is valid for star PI, which again confirms the conclusion for bulk PI reported in literature.[29,30)]

In summary, the validity and invalidity of the full-DTD picture have been confirmed for the linear and star PI in the solutions. This result suggests that an *extra* room for tube dilation remains for the star PI but not for linear PI in the linear viscoelastic regime (at equilibrium). This difference between the linear and star PI at equilibrium could be one of the key factors for understanding a difference in their rheo-dielectric behavior under fast shear flow, as discussed in the following sections.

5-5-3. Rheo-dielectric behavior under steady shear.

5-5-3a. experimental observation.

Figs. 5-7 and 5-8, respectively, show the $\Delta\varepsilon'(\omega)$ and $\varepsilon''(\omega)$ data of the linear and star PI solutions under steady shear flow at the rates $\dot{\gamma}$ as indicated. (The data were obtained with the AdC method and the relaxational current was Fourier transformed to obtain $\Delta\varepsilon'(\omega)$ and $\varepsilon''(\omega)$, as explained for Figs. 5-3 and 5-4.) The Weissenberg number $\dot{\gamma}\tau_G(0)$ defined with respect to the terminal viscoelastic relaxation time in the linear regime, $\tau_G(0)$ (Eq. 5-10), ranges from 0.7 to 6.7 for linear PI and from 1.0 to 8.5 for star PI. For comparison, the data at equilibrium ($\dot{\gamma}$ = 0; already shown in Figs. 5-3 and 5-4) are reproduced with the solid curves.

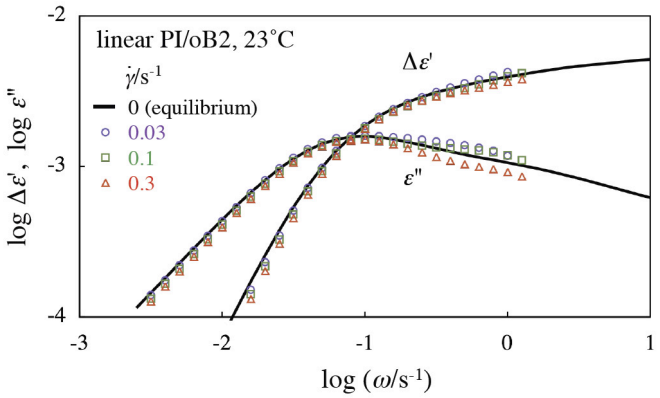

Fig. 5-7. Rheo-dielectric behavior of linear PI/oB2 solution (5 wt%) at 23˚C.

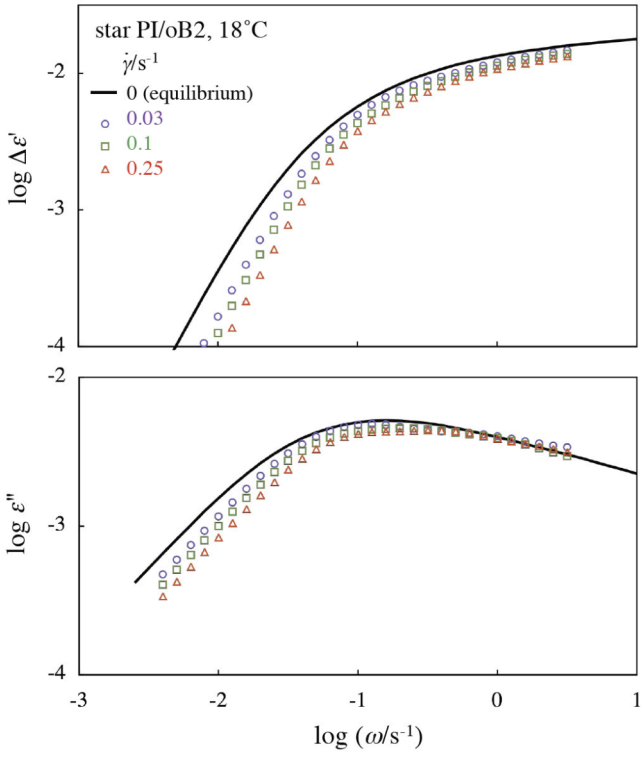

Fig. 5-8. Rheo-dielectric behavior of star PI/oB2 solution (20 wt%) at 18˚C.

The Green-Kubo (GK) theorem, relating the dielectric signal of PI to the end-to-end (or

end-to-branching point) fluctuation, is satisfactorily valid under steady shear, at least up to the order of $\dot{\gamma}^2$, as discussed in Chapter 3. Consequently, the dielectric relaxation function under steady shear, $\Phi_{ss}(t)$, is safely described by Eqs. 5-11 and 5-12 with the average $\langle \cdots \rangle$ being taken under the steady shear. Thus, the data presented in Figs. 5-7 and 5-8 serve as a rigid basis for discussing the fluctuation in the shear-gradient direction (the direction of the electric field).

This fluctuation is rather insensitive to the steady shear for linear PI but moderately accelerated for star PI, as noted in Figs. 5-7 and 5-8. This behavior can be quantitatively examined in Fig. 5-9 where the terminal dielectric relaxation time τ_ε (defined by Eq. 5-1) under steady shear is normalized by its equilibrium value $\tau_\varepsilon(0)$ and plotted against the Weissenberg number defined with respect to the terminal relaxation time, $\dot{\gamma}\tau_G(0)$. For comparison, the viscosity η measured simultaneously with the $\Delta\varepsilon'$ and ε'' data are also shown

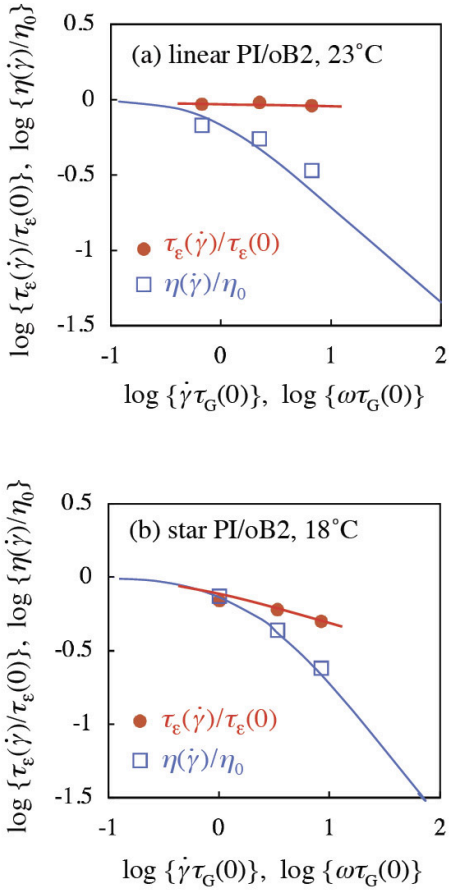

Fig. 5-9. Shear rate dependence of the rheo-dielectric relaxation time (filled red circles) of the linear and star PI solutions. For comparison, plots are shown also for the non-Newtonian viscosity (η; blue squares) and the dynamic viscosity in the linear regime (η'; blue curves).

in a normalized form ($\eta(\dot{\gamma})$ data reduced by the zero-shear viscosity η_0). The thin blue curves indicate the normalized dynamic viscosity $\eta'(\omega)/\eta_0$ (with $\eta'(\omega) = G''(\omega)/\omega$) plotted against the normalized frequency, $\omega\tau_G(0)$. The viscosity $\eta(\dot{\gamma})$ exhibits considerable thinning, and its $\dot{\gamma}$ dependence is close to the ω dependence of the linear viscoelastic $\eta'(\omega)$ (namely, the empirical Cox-Merz rule[2,3] is valid). Despite this nonlinear feature of $\eta(\dot{\gamma})$, the rheo-dielectric τ_ε of linear PI hardly decreases (by ~10% at the maximum) in the range of $\dot{\gamma}$ examined. For star PI, τ_ε exhibits a detectable decrease (by ~50%) but this decrease is considerably milder compared to the thinning of $\eta(\dot{\gamma})$. All these features are similar to those explained in Chapter 2.

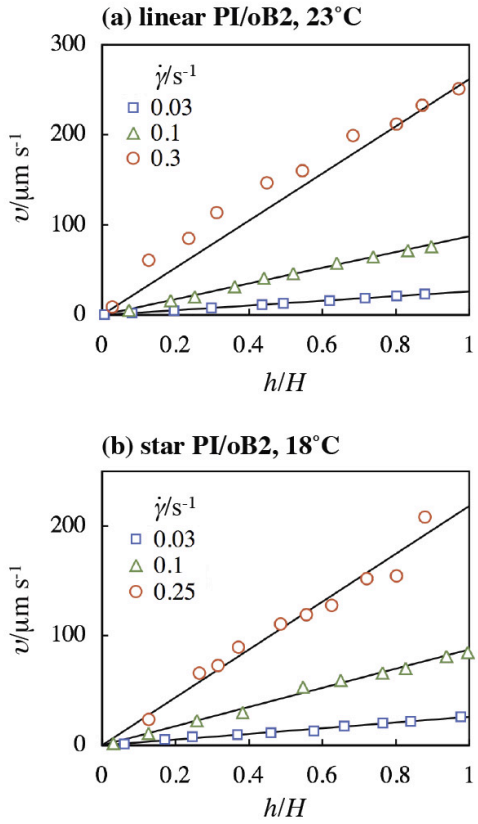

Fig. 5-10. Flow velocity profile in the PI solutions determined with particle tracking velocimetry. The particle velocity in the shear direction, υ, is plotted against the particle height h from the fixed plate normalized by the gap H. Solid lines show the profile for uniform flow (no shear banding/no secondary flow).

The flow velocity profile determined by tracing the dilute particles dispersed in the PI solutions is shown in Fig. 5-10, where the particle velocity υ is plotted against the particle height h from the fixed part of the rheometer (plate) normalized by the gap H between the cone and plate. The particles did not

affect the viscoelastic data, as explained earlier. For the shear rates examined in Fig. 5-10, the measured profiles (plots) agree, within experimental resolution, with the solid lines that represent the profile for uniform flow associated with no shear banding/no secondary flow. Flow instability due to the edge fracture (partly similar to the shear banding reported in literature[13-15]) was observed for the linear PI solution at $\dot{\gamma}$ = 0.6 s^{-1}. The mild deviation of the plot from the line seen in Fig. 5-10a for $\dot{\gamma}$ = 0.3 s^{-1} might be attributed to a weak heterogeneity in the flow profile (a pre-effect of such flow instability). However, the lowest local rate evaluated from the least steep part of the plot for $\dot{\gamma}$ = 0.3 s^{-1}, $\dot{\gamma}_{local} \cong 0.22$ s^{-1}, is well above $1/\tau_G(0)$ (= 0.045 s^{-1}) so that the weak heterogeneity, *if any*, hardly affects the plot of τ_ε in Fig. 5-9a. Thus, the weak $\dot{\gamma}$ dependence of τ_ε (in particular for linear PI) associated with strong thinning of η reflects a real feature of the chain dynamics under *uniform* flow.

5-5-3b. origin of weak shear effect on the rheo-dielectric behavior

The weak $\dot{\gamma}$ dependence of τ_ε of linear and star PI is the real feature under *uniform* flow, as confirmed in the previous section. This weak dependence could be attributable to several different mechanisms.

The first mechanism to be considered is the convective constraint release (CCR) mechanism[6-9] that is incorporated in the current tube model as the key mechanism to suppress unphysical decrease of the stress on an increase of $\dot{\gamma}$ ($> 1/\tau_G(0)$). This mechanism

unavoidably results in a decrease of τ_ε that is similar, in magnitude, to the decrease of η, as explained in Chapter 4. More specifically, this strong $\dot{\gamma}$ dependence of τ_ε is directly found in the expression of the relaxation time in the CCR model firstly proposed by Ianniruberto and Marrucci,[6] $1/\tau_G(\dot{\gamma}) = 1/\tau_G(0) + K\dot{\gamma}$ with the factor K being determined by the chain orientation. Furthermore, detailed calculation based on the current tube model(s) results in a strong acceleration of the dielectric relaxation under fast shear. An example is shown in Fig. 5-11 for the Graham-Likhtman-McLeish-Milner (GLaMM) model.[9] The model calculation, kindly made by Dr. R. Graham at University of Nottingham, targets an entangled linear PI/oB2 solution ($M_{PI} = 1.19\times10^6$ and $w_{PI} =$ 15 wt%) examined in literature.[12] He calculated the local correlation function $C(n,t;m)$ defined by Eq. 2-31 with the closure approximation similar (through not identical) to that in the original GLaMM model, and further evaluated the dielectric relaxation function by integrating $C(n,t;m)$ with respect to the subchain indices n and m.

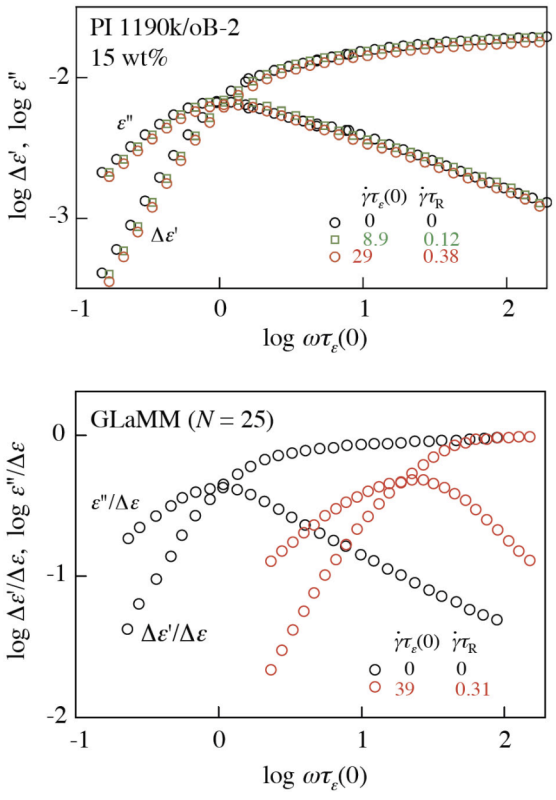

Fig. 5-11. Comparison of rheo-dielectric data of entangled linear PI solution[8] (top panel) with calculation of GLaMM model[9] (bottom panel).

(This evaluation method is valid because the Green-Kubo theorem holds satisfactorily for the

end-to-end fluctuation under steady shear flow.)

Fig. 5-11 clearly shows that the calculated rheo-dielectric relaxation exhibits an order-of-magnitude acceleration under the fast shear at the terminal-time-based Weissenberg number $\dot{\gamma}\tau_\varepsilon(0)$ = 39 (Rouse-time-based Weissenberg number $\dot{\gamma}\tau_R$ = 0.31), whereas the data[12] show much less acceleration (by a factor of ~30% even at $\dot{\gamma}\tau_\varepsilon(0)$ = 29). Thus, even the GLaMM model, the most elaborated tube model available now, does not reproduce the rheo-dielectric behavior (that reflects the orientational memory of the chain between two times, 0 and *t*), although this model excellently describes the viscoelastic data as well as the small angle neutron scattering data[31] (both detect the *isochronal* segment distribution or orientation). Furthermore, the multi-chain sliplink simulation based on the primitive chain network model (NAPLES), that automatically exhibits the CCR behavior, describes the η data very well but overestimates the $\dot{\gamma}$ dependence of τ_ε, as already shown in Fig. 3-2. Thus, some factor is still missing in the current tube model(s) and sliplink simulations.

One possible hypothesis to explain the weak shear effect on the rheo-dielectric behavior can be found in the concept of "hidden entanglement appearance" (HEA) proposed by Ianniruberto and Marrucci.[32] Namely, if the CCR-induced removal of entanglements of a given chain (probe) is compensated by rapid, *isotropic* reformation of entanglements with the surrounding chains, the orientational anisotropy/stress of the probe chain does not change, in principle, thereby retaining the strong thinning of η, whereas the path length for

reptation/arm retraction increases (toward the length at equilibrium) on this reformation to reduce the shear effect on τ_ε.

This isotropic entanglement reformation under flow would occur for both linear and star chains. However, at equilibrium, the full-DTD relationship is valid for the linear chain but not for the star chain (cf. Figs. 5-3 and 5-4). This result suggests that the star chain at equilibrium has an *extra* room for tube dilation compared to the linear chain. Then, under the steady shear, the CCR effect competing with the isotropic entanglement reformation could be stronger for the star chain than for the linear chain to give the mild $\dot{\gamma}$ dependence of τ_ε for the star chain (that is still weaker than the dependence of η).

The above hypothesis sounds reasonable but does not complete the whole molecular story. First of all, a recent experiment[28] for binary PI/PI blends composed of dilute short probe chains in a matrix of much longer chains suggests that monodisperse linear PI chains at equilibrium exhibit reptation along a partially dilated tube that wriggles in the fully dilated tube. In other words, the full-DTD picture valid for those chains at equilibrium just specifies the relation between the tube survival fraction and the modulus, *i.e.*, the stress level, but does not predict the relaxation time (that is determined by the reptation path length). No corresponding data are available for star PI blends containing dilute short probes, and it remains unknown if the retraction path length of the star arm at equilibrium is shortened by the CR/DTD mechanism more significantly compared to the reptation path length of the

linear chain. Thus, the above argument for the difference of τ_ε of the linear and star chains under flow, being based on the validity/invalidity of the full-DTD picture at equilibrium, needs to be further tested experimentally.

The second possible hypothesis is the anisotropy of the subchain mobility under shear flow, as discussed in Chapter 4. If the chain is highly oriented under shear flow, the mobility in the shear (*x*) direction may become enhanced whereas that in the shear gradient (*y*) direction could remain unaffected. If this is the case, the chain motion in the *x* direction is accelerated to reduce the orientational anisotropy/stress thereby providing the viscosity with strong $\dot{\gamma}$ dependence, whereas the motion in the *y* direction is less accelerated to give $\dot{\gamma}$-insensitive τ_ε, as verified for the anisotropic mobility model in Chapter 4. Nevertheless, the difference in the $\dot{\gamma}$ dependence of τ_ε was noted for the linear and star PI in essentially the same range of the Weissenberg number $\dot{\gamma}\tau_G(0)$ where η decreases similarly for linear and star PI (Fig. 5-9). This fact suggests that the anisotropy in the mobility is not determined only by the chain orientation but could depend on the mode of chain motion. This point is to be further examined with the aid of dynamic models and/or simulation.

5-5-4. Rheo-dielectric behavior under LAOS.

5-5-4a. behavior detected with constant electric field:

For the linear and star PI solutions, respectively, Figs. 5-12a and 5-12b show the stationary

Lissajou's patterns (stress-strain patterns) obtained under LAOS at the angular frequencies Ω = 1 and 0.1 s^{-1}, respectively. These Ω values were chosen to be well above the terminal viscoelastic relaxation frequency of the solutions, $\omega_G(0) = 1/\tau_G(0)$ = 0.045 and 0.029 s^{-1} for linear and star PI, respectively (cf. Eq. 5-10). The LAOS amplitude γ_0 was varied from 0.1 (in the linear regime) to 2 or 4, and the stress $\sigma(t)$ and strain $\gamma(t)$ (= $\gamma_0 \sin \Omega t$) shown in the Lissajou's patterns are normalized by γ_0. The patterns are distorted from ellipsoid on an increase of $\gamma_0 > 0.5$. This distortion corresponds to contribution of higher order odd harmonics to $\sigma(t)$ for large γ_0.[33,34]

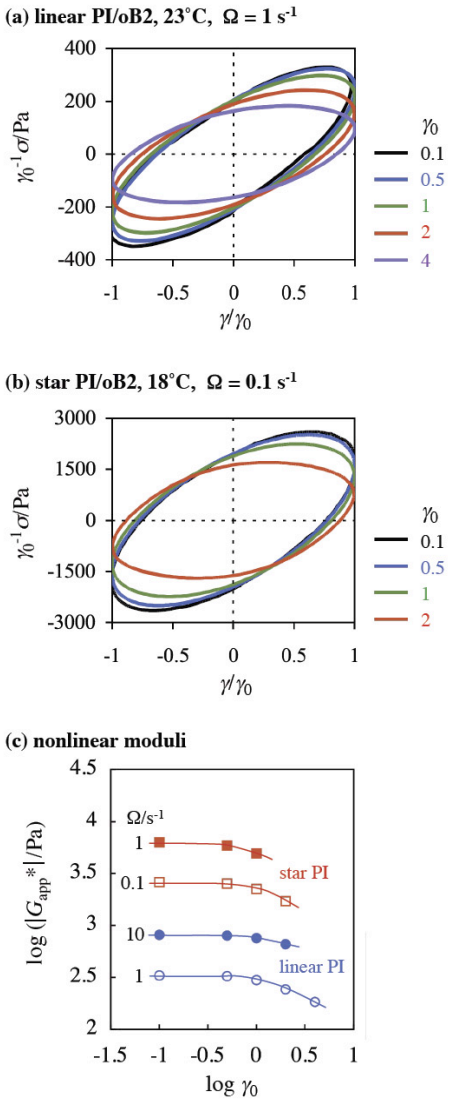

Fig. 5-12. Lisssajou's patterns obtained for linear and star PI solutions under LAOS at the frequency Ω and amplitude γ_0 as indicated (panels a and b). In panel c, the magnitude of apparent modulus is plotted against γ_0.

Nonlinearity under LAOS provides the Lissajou's pattern with not only the distortion but also a decrease of the maximum value of the normalized stress, $\sigma(t)/\gamma_0$, that can be defined as the magnitude of apparent modulus $|G_{app}^*|$. ($|G_{app}^*|$ reduces to the magnitude of the well-defined linear viscoelastic modulus $|G^*|$ under small strains.) In Fig. 5-12c, $|G_{app}^*|$

evaluated from the Lissajou's patterns (a) and (b) is plotted against the LAOS amplitude γ_0 (unfilled symbols). For comparison, $|G_{app}^*|$ of the linear and star PI solutions obtained at higher Ω are also shown (filled symbols). For both solutions, the decrease of $|G_{app}^*|$ becomes significant for $\gamma_0 > 0.5$. The decrease in this range of γ_0 and at $\Omega > \omega_G$ is well known for entangled polymers. [33,34)]

Uniformity of the strain field under the above LAOS condition was examined by tracing particles in the samples. For the linear PI solution, the particles were clearly observed for all Ω and γ_0 values examined and the particle positions were digitalized/analyzed as explained earlier. This was the case also for the star PI solution (except at $\Omega = 1$ s^{-1} and $\gamma_0 = 1$ where the sample surface became wavy and the particles were not clearly observed; no analysis was attempted for this case). It turned out that the oscillation of the particle position was in phase with the macroscopic oscillation of the moving part (cone) of the rheometer, and the maximum velocity υ_{max} of the particles (in the shear direction) was observed when the particles were located at the center of oscillation.

For the linear and star PI solutions, υ_{max} thus determined is shown in Figs. 5-13 and 5-14, respectively. υ_{max} is plotted against the particle height h from the fixed part of the rheometer (plate) normalized by the gap H between the cone and plate. The solid lines indicate the relationship realized for uniform oscillatory strain field without shear-banding and/or secondary flow,

$$\upsilon_{max} = \frac{h}{H}\gamma_0\theta_{cp}r_p\Omega \qquad (5\text{-}16)$$

where r_p and θ_{cp} denote the plate radius and the gap angle between the cone and plate, respectively. The data (plots) coincide, within experimental uncertainty, with the lines, confirming the uniformity of the LAOS field.

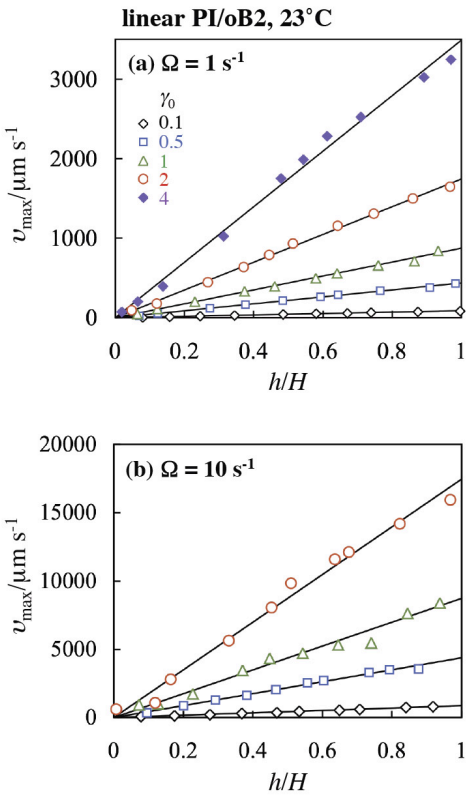

Fig. 5-13. Maximum velocity υ_{max} of particles dispersed in the linear PI solution. υ_{max} is plotted against the particle height h from the fixed plate normalized by the gap H. Solid lines show υ_{max} realized for uniform oscillatory strain field.

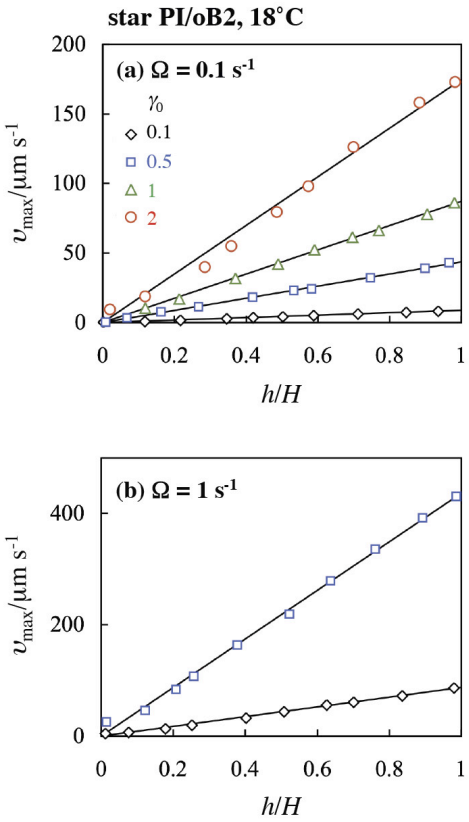

Fig. 5-14. Maximum velocity υ_{max} of particles dispersed in the star PI solution. υ_{max} is plotted against the particle height h from the fixed plate normalized by the gap H. Solid lines show υ_{max} realized for uniform oscillatory strain field.

The adsorption current (AdC) method explained earlier was utilized to obtain the relaxational current $I_{relax}(t)$ under the rectangular electric field. Figs. 5-15 and 5-16 show the $I_{relax}(t)$ data obtained for the linear and star PI solutions, respectively. For comparison, the $I^{eq}_{relax}(t)$ data at

equilibrium (without LAOS) are shown with the thick solid curves. (Those $I_{\mathrm{relax}}^{\mathrm{eq}}(t)$ data were utilized to evaluate $\Delta\varepsilon'(\omega)$ and $\varepsilon''(\omega)$ shown in Figs. 5-3 and 5-4.) Clearly, the $I_{\mathrm{relax}}^{\mathrm{eq}}(t)$ data decays monotonically with time, whereas $I_{\mathrm{relax}}(t)$ under LAOS oscillates around $I_{\mathrm{relax}}^{\mathrm{eq}}(t)$. This oscillation never vanished even at long $t >> \tau_{\mathrm{G}}(0)$ (= $1/\omega_{\mathrm{G}}(0)$) where $I_{\mathrm{relax}}^{\mathrm{eq}}(t)$ fully decayed to zero. $I_{\mathrm{relax}}^{\mathrm{eq}}(t)$ oscillates with a period of π/Ω in most cases, although the oscillation is not perfectly sinusoidal and thus contributed from harmonics oscillating with different periods (for the higher harmonics of LAOS).

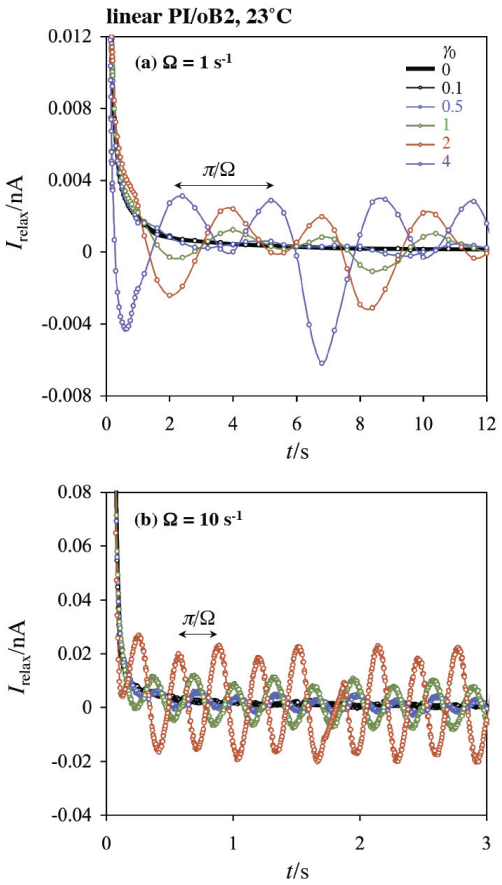

Fig. 5-15. Relaxational current $I_{\mathrm{relax}}(t)$ measured for the linear PI solution under the LAOS condition as indicated. Thick solid curve shows the $I_{\mathrm{relax}}(t)$ data at equilibrium (without LAOS).

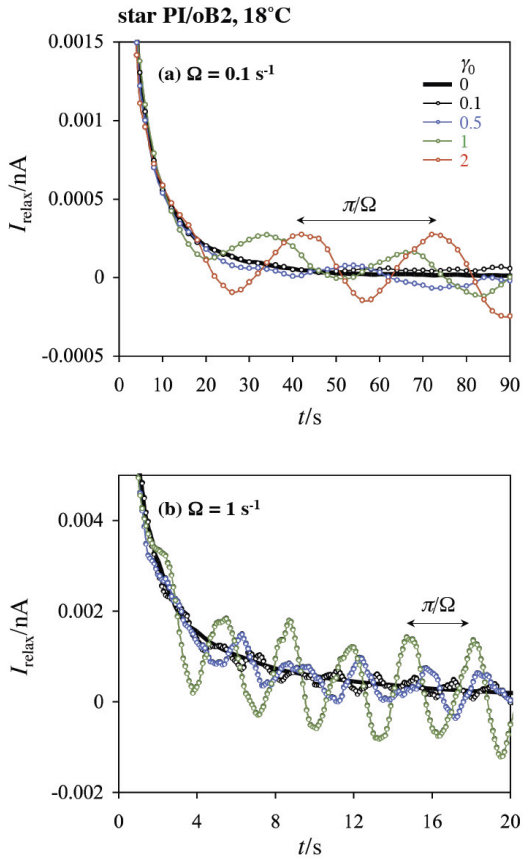

Fig. 5-16. Relaxational current $I_{\mathrm{relax}}(t)$ measured for the star PI solution under the LAOS condition as indicated. Thick solid curve shows the $I_{\mathrm{relax}}(t)$ data at equilibrium (without LAOS).

The oscillation of $I_{\mathrm{relax}}(t)$ observed under LAOS is intimately related to the oscillation of the conformational distribution function f_{LAOS} coupled with LAOS, as analyzed in Chapter 3. Specifically, the analysis indicates that this oscillation of f_{LAOS} forces $I_{\mathrm{relax}}(t)$ to oscillate around a monotonically decaying average, $I_{\mathrm{relax}}^{\mathrm{ave}}(t) \equiv (\Omega/2\pi)\int_{t-\pi/\Omega}^{t+\pi/\Omega} I_{\mathrm{relax}}^{\mathrm{ave}}(t')\,\mathrm{d}t'$. This oscillatory feature of $I_{\mathrm{relax}}(t)$ is consistent with the data in Figs. 5-15 and 5-16, lending support to the analysis in Chapter 3.

The analysis in Chapter 3 also suggests that the oscillation includes, in principle, all harmonics of LAOS (having periods of $2\pi/p\Omega$ with p = 1, 2, 3,…) because of the normalization condition for f_{LAOS} (cf. Eqs. 3-16 and 3-18), but the oscillation dominantly occurs with the period π/Ω (p = 2) accompanying the squared strain, γ^2 ($= \gamma_0^2 \sin^2 \Omega t = \{\gamma_0^2/2\}\{1-\cos 2\Omega t\}$) if the LAOS effect on f_{LAOS} is rather mild. This theoretical argument is also consistent with the experiments, as noted in Fig. 5-17 where the Fourier power spectra $J(\omega)$ of the $\Delta I_{\mathrm{relax}}(t) = I_{\mathrm{relax}}(t) - I_{\mathrm{relax}}^{\mathrm{eq}}(t)$ data ($\cong I_{\mathrm{relax}}(t) - I_{\mathrm{relax}}^{\mathrm{ave}}(t)$; oscillatory component of I_{relax}) are shown for the linear and star PI solutions subjected to fast LAOS (at Ω = 10 and 1 s^{-1}, respectively).

In a very *qualitative* sense, the decay of the average $I_{\mathrm{relax}}^{\mathrm{ave}}(t)$ becomes faster if the end-to-end fluctuation is accelerated by LAOS, and *vice versa*, as noted from the analysis in Chapter 3. The data in Figures 5-15 and 5-16 suggest no significant acceleration of the decay of $I_{\mathrm{relax}}^{\mathrm{ave}}(t)$ under LAOS, which is in harmony with the results obtained under steady shear (Figs. 5-7 and 5-8).

It may look tempting to make detailed analysis of the $I_{relax}(t)$ data under LAOS (and their power spectra) for extracting quantitative molecular information from those data. Such analysis is interesting and important but, unfortunately, highly complicated to be achieved rigorously, because the conformational distribution function f_{LAOS} is coupled with LAOS to oscillate with time, as explained in Chapter 3. This oscillation leads to oscillatory decay of the I_{relax} data, but the oscillatory parts of f_{LAOS} and I_{relax} are not in proportion to each other and a relationship between these parts depends on the functional form of f_{LAOS}. In other words, f_{LAOS} cannot be straightforwardly and uniquely determined from the I_{relax} data, unless some approximation is made. For this reason, this Chapter attempts no detailed/molecular analysis of the data shown in Figs. 5-15 and 5-16.

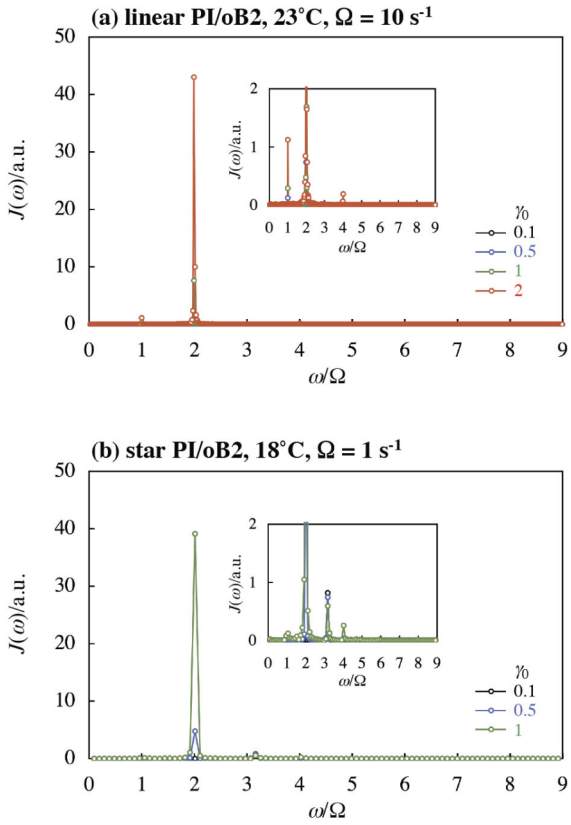

Fig. 5-17. Fourier power spectra $J(\omega)$ calculated from the relaxational current $I_{relax}(t)$ data for the linear and star PI solutions (Figs. 5-14 and 5-15) at the highest LAOS frequencies Ω examined for respective solutions. $J(\omega)$ is plotted against a normalized angular frequency ω/Ω. The inset magnifies the weak but detectable harmonics.

5-5-4b. comment for measurements with sinusoidal electric field:

In relation to the above complication in the analysis of the data obtained for the constant (rectangular) electric field, one might consider that the apparent dielectric loss $\varepsilon''(\omega)$ under LAOS is to be measured with the standard method utilizing the sinusoidal electric field. In fact, such $\varepsilon''(\omega)$ data have been reported and discussed in literature.[35,36] However, those $\varepsilon''(\omega)$ data are equivalent to the Fourier transformation of $I_{\text{relax}}(t)$ that exhibits the oscillatory decay (cf. Figs. 5-15 and 5-16) and are affected by the interference between the LAOS and electric fields, as explained in Chapter 3. (No similar interference occurs under steady shear): This interference provides $\varepsilon''(\omega)$ with an *artificial* relaxation process that is in a sense similar to the resonance at $\omega = p\Omega$ with p = 1, 2, ...; cf. Eq. 3-25 in Chapter 3 (where the relaxational current $I_{\text{relax}}(t)$ corresponds to the time derivative of polarization, dP_{LAOS}/dt.) Furthermore, $\left\langle R_y^2 \right\rangle$ evaluated from the relaxation intensity of $\varepsilon''(\omega)$ under LAOS deviates from the real $\left\langle R_y^2 \right\rangle$ averaged during the LAOS period (cf. Fig. 3-4), meaning that the $\varepsilon''(\omega)$ data under LAOS do not include the full/straightforward molecular information of the chain dynamics under LAOS. Analysis of such $\varepsilon''(\omega)$ data is extremely complicated even compared to the analysis of the $I_{\text{relax}}(t)$ data under the constant electric field. This analysis, if made for the data under LAOS, should result in a physically unreasonable molecular picture. For this reason, this Chapter did not attempt to measure/analyze $\varepsilon''(\omega)$ under LAOS.

5-6. Conclusion

This Chapter examined the rheo-dielectric behavior of entangled solutions of linear and star PI chains subjected to steady shear. The particle tracking velocimetry confirmed uniformity of the flow field (lack of shear banding/secondary flow) in the range of Weissenberg number Wi (= $\dot{\gamma}\tau_G(0)$) examined. For linear PI examined at $Wi < 7$, the dielectric behavior was hardly affected by the steady shear, whereas the viscosity η exhibited considerable thinning. In contrast, for star PI, the dielectric relaxation was mildly accelerated by the steady shear in a similar range of Wi (< 8.5), but this acceleration was less significant compared to the thinning of η. These rheo-dielectric features were observed under *uniform* steady shear, which suggests that the linear and star PI chains exhibit essentially different dynamics under steady fast shear. This difference possibly reflects a difference of the constraint release effect for those chains at equilibrium/under flow and is also related to anisotropy of the subchain mobility (cf. Chapter 4) that would emerge if the chains are highly oriented.

The rheo-dielectric behavior of the linear and star PI chains was examined also under LAOS. The uniformity of the LAOS field was confirmed from the particle tracking velocimetry. The relaxational current under a constant (rectangular) electric field exhibited oscillation around the monotonically decaying average current, and the main period of oscillation was close to π/Ω with Ω being the LAOS angular frequency. This behavior lent

support to the analysis made in Chapter 3 on the basis of the Green-Kubo theorem. The decay of the average current was not significantly affected by LAOS, which was in harmony with the behavior observed under steady shear.

References

1) M. Doi and S. F. Edwards, S. The Theory of Polymer Dynamics; Clarendon: Oxford, 1986.

2) T. C. B. McLeish, Advances in Physics, 51, 1379 (2002).

3) H. Watanabe, Progress in Polymer Science, 24, 1253 (1999).

4) A. E. Likhtman, Viscoelasticity and molecular rheology, in Polymer Science: A Comprehensive Reference, 1st Ed., Volume 1: Basic Concepts and Polymer Properties, M. Möeller and K. Matyjaszewski Eds., Elsevier: Amsterdam, 2012.

5) D. S. Pearson, E. Herbolzheimer, N. Grizzuti, and G. Marrucci, Journal of Polymer Science Part B, Polymer Physics, 29, 1589 (1991).

6) G. Ianniruberto and G. Marrucci, Journal of Non-Newtonian Fluid Mechanics, 65, 241 (1996).

7) D. W. Mead, R. G. Larson, and M. Doi, Macromolecules, 31, 7895 (1998).

8) S. T. Milner, T. C. B. McLeish, and A. E. Likhtman, Journal of Rheology, 45, 539 (2001).

9) R. S. Graham, A. E. Likhtman, T. C. B. McLeish, and S. T. Milner, Journal of Rheology, 47, 1171 (2003).

10) Y. Masubuchi, H. Watanabe, G. Ianniruberto, F. Greco, and G. Marrucci, Nihon Reoroji Gakkaishi (Journal of the Society of Rheology, Japan), 32, 197 (2004).

11) K. Furuichi, C. Nonomura, Y. Masubuchi, H. Watanabe, G. Ianniruberto, F. Greco, and G. Marrucci, Rheologica Acta, 47, 591 (2008).

12) H. Watanabe, S. Ishida, and Y. Matsumiya, Macromolecules, 35, 8802 (2002).

13) P. Tapadia and S. Q. Wang, Physical Review Letters, 91, 198301 (2003).

14) P. Tapadia, S. Ravindranath, and S. Q. Wang, S. Q. Physical Review Letters, 96, 196001 (2006).

15) S. Q. Wang, S. Ravindranath, and P. E. Boukany, Macromolecules, 44, 183 (2011).

16) H. Watanabe, S. Ishida, Y. Matsumiya, and T. Inoue, Macromolecules, 37, 1937 (2004).

17) H. Watanabe, S. Ishida, Y. Matsumiya, and T. Inoue, Macromolecules, 37, 6619 (2004).

18) T. Sawada, X. Qiao, and H. Watanabe, Nihon Reoroji Gakkaishi (Journal of the Society of Rheology, Japan), 35, 11 (2007).

19) H. Watanabe, T. Sato, and K. Osaki, Macromolecules, 29,104 (1996).

20) H. Watanabe, Y. Matsumiya, and T. Inoue, Macromolecules, 35, 2339 (2002).

21) R. Hayakawa, H. Kanda, M. Sakamoto, and Y. Wada, Japanese Journal of Applied Physics, 14, 2039 (1975).

22) K. Adachi and H. Hirano, Macromolecules, 31, 3958 (1998).

23) H. Watanabe, Macromolecular Rapid Communications, 22, 127 (2001).

24) Y. Matsumiya, A. Uno, H. Watanabe, T. Inoue, and O. Urakawa, Macromolecules, 44, 4355 (2011).

25) J. D. Ferry, Viscoelastic Properties of Polymers, 3rd Ed., Wiley, New York, 1980.

26) H. Watanabe, Polymer Journal, 41, 929 (2009).

27) R. Cole, Journal of Chemical Physics, 42, 637 (1965).

28) Y. Matsumiya, K. Kumazawa, M. Nagao, O. Urakawa, and H. Watanabe, Macromolecules, 46, 6067 (2013)

29) H. Watanabe, T. Sawada, and Y. Matsumiya, Macromolecules, 39, 2553 (2006).

30) X. Qiao, T. Sawada, Y. Matsumiya, and H. Watanabe, Macromolecules, 39, 7333 (2006).

31) A. Blanchard, R. S. Graham, M. Heinrich, W. Pyckhout-Hintzen, D. Richter, A. E. Likhtman, T. C. B. McLeish, D. J. Read, E. Straube, and J. Kohlbrecher, Physical Review Letters, 95, 166001 (2005).

32) G. Ianniruberto and G. Marrucci, Journal of Non-Newtonian Fluid Mechanics, 95, 363 (2000).

33) M. Sugimoto, Y. Suzuki, K. Hyun, K. H. Ahn, T. Ushioda, A. Nishioka, T. Taniguchi, and K. Koyama, Rheologica Acta, 46, 33 (2006).

34) K. Hyun and M. Wilhelm, Macromolecules, 42, 411 (2009).

35) S. Höfl, F. Kremer, H. W. Spiess, M. Wilhelm, and S. Kahle, Polymer, 47, 7282 (2006).

36) S. Capaccioli, D. Prevosto, A. Best, A. Hanewald, and T. Pakula, Journal of Non-Crystalline Solids, 353, 4267 (2007).

Chapter 6. Summary

Following the general introduction (Chapter 1) and the description of current molecular pictures for the entangled polymer dynamics (Chapter 2), the results of theoretical analysis and experiments for rheo-dielectric behavior of type-A *cis*-polyisoprene (PI) chains are described/discussed in Chapters 3 to 5. The findings in these chapters are summarized below.

In Chapter 3, a theoretical analysis is conducted for the molecular expression of the dielectric response of the type-A PI chains under steady shear and LAOS. The analysis based on the Langevin equation suggests that the rheo-dielectric response under *steady shear* can be satisfactorily described by the end-to-end vector auto-correlation function and thus the Green-Kubo theorem holds satisfactorily for the end-to-end fluctuation even at high shear rates where significant nonlinearities are observed for viscoelastic properties. In particular, exact coincidence of the dielectric relaxation time and end-to-end fluctuation time is concluded from the analysis. In addition, the rheo-dielectric intensity under steady shear is found to be proportional to the mean-square chain size in the shear gradient direction, $\left\langle R_y^2 \right\rangle$ (that is an average over the time-independent conformational distribution function).

In contrast, under large amplitude oscillatory strain $\gamma = \gamma_0 \sin \Omega t$ (LAOS), the Green-Kubo analysis shows that the conformational distribution function f_{LAOS} is coupled with the LAOS field to oscillate with time, and the rheo-dielectric response detects this oscillation of f_{LAOS}.

Thus, the response against a constant electric field exhibits an oscillatory decay (with the dominant oscillation period of π/Ω). The response against the sinusoidal electric field splits into a series of two components oscillating at ω and $\omega \pm \beta\Omega$ (b = 1, 2, …), where ω is the angular frequency of electric field, and a resonant-like feature is noted for the latter component. Consequently, the rheo-dielectric intensity under LAOS, evaluated from the former component, is no longer proportional to $\left\langle R_y^2 \right\rangle$.

In Chapter 4, a non-equilibrium Langevin equation model for weakly entangled polymers, incorporating *anisotropic* mobility tensor (the anisotropic mobility model), was formulated and analyzed. The anisotropic mobility tensor was phenomenologically introduced on the basis of the symmetry argument and diffusion simulation. In the anisotropic mobility model, the dynamics of the polymer chains is *anisotropically* accelerated, and both the shear thinning of the steady state viscosity and the shear rate insensitive rheo-dielectric response function, observed experimentally, are naturally reproduced (though qualitatively). This is in contrast to the conventional CCR model, which incorporates the *isotropic* acceleration that unavoidably results in the acceleration of the rheo-dielectric relaxation. The anisotropic mobility model can also reproduce the difference in the shear rate dependence of the parallel and perpendicular moduli detected with a small oscillatory strain imposed on the steady shear in respective directions.

Chapter 5 is devoted for experimental tests of the rheo-dielectric behavior of entangled

solutions of linear and star-branched PI under uniform steady shear and LAOS. The particle tracking velocimetry confirmed uniformity of the flow field (lack of shear banding/secondary flow) in the range of Weissenberg number Wi (= $\dot{\gamma}\tau_G(0)$) examined. For linear PI examined at $Wi < 7$, the dielectric behavior was hardly affected by the steady shear, whereas the viscosity η exhibited considerable thinning. In contrast, for star PI, the dielectric relaxation was mildly accelerated by the steady shear in a similar range of Wi (< 8.5), but this acceleration was less significant compared to the thinning of η. On the basis of the molecular expression of the rheo-dielectric response function analyzed in Chapter 3, these rheo-dielectric features, observed under *uniform* steady shear, suggest an essential difference in the dynamics of the linear and star PI chains under steady fast shear. This difference possibly reflects a difference of the constraint release effect for those chains at equilibrium/under flow and is also related to anisotropy of the subchain mobility (cf. Chapter 4) that would emerge if the chains are highly oriented.

The rheo-dielectric behavior of the linear and star PI chains was examined also under LAOS, where the strain uniformity was confirmed from the particle tracking velocimetry. The relaxational current under a constant (rectangular) electric field exhibited oscillation around the monotonically decaying average current, and the main period of oscillation was close to π/Ω with Ω being the LAOS angular frequency. This behavior lent support to the analysis made in Chapter 3 on the basis of the Green-Kubo theorem. The decay of the

average current was not significantly affected by LAOS, which was in harmony with the behavior observed under steady shear.

List of Publication

I. Publications Included in This Thesis

1) Rheo-Dielectric Responses of Entangled cis-Polyisoprene under Uniform Steady Shear and LAOS

K. Horio, T. Uneyama, Y. Matsumiya, Y. Masubuchi, and H. Watanabe

Macromolecules, on line publication (2014); dx.doi.org/10.1021/ma402100t .

2) Rheo-Dielectric Behavior of Soft Matters

H. Watanabe, Y. Matsumiya, K. Horio, Y. Masubuchi, and T. Uneyama

Non-Equilibrium Soft Matter Physics (S. Komura and T. Ohta ed.), World Scientific, Singapore, vol 4, Chapter 2 (pp 37-87) (2012).

3) Anisotropic Mobility Model for Polymers under Shear and its Linear Response Functions

T. Uneyama, K. Horio, and H. Watanabe

Physical Review E, 83, [061802] 1-15 (2011).

4) A Theoretical Analysis of Rheo-dielectric Relaxation Function

T. Uneyama, Y. Masubuchi, K. Horio, Y. Matsumiya, H. Watanabe, J. A. Pathak, and C. M. Roland

Journal of Polymer Science, B: Polymer Physics, 47, 1039-1057 (2009).

II. Other related Publications

1) Equilibrium Statistics of Weakly Slip-Linked Gaussian Polymer Chains

   T. Uneyama and K. Horio

   Journal of Polymer Science B: Polymer Physics, 49, 966-977 (2011).

2) Primitive Chain Network Simulations for Entangled DNA Solutions

   Y. Masubuchi, K. Furuichi, K. Horio, T. Uneyama, H. Watanabe, G. Ianniruberto, F. Greco, and G. Marrucci

   Journal of Chemical Physics, 131, [114906] 1-8 (2009).

3) Fluctuation in entanglement positions via elastic slip-links

   J. D. Schieber and K. Horio

   Journal of Chemical Physics, 132, [074905] 1-11 (2009).

4) Pre-averaged sampling on the entanglement kinetics for polymer dynamics

   K. Horio and Y. Masubuchi

   Macromolecular Symposia, 242, 140-145 (2006).

Acknowledgements

This thesis is based on the study carried out under the direction of Professor Hiroshi Watanabe, Institute for Chemical Research, Kyoto University, from 2008 to 2013. The author would like to express his sincerest gratitude to Professor Watanabe for his generous guidance, invaluable suggestions, and continual encouragement throughout this study.

The author wishes to express his sincerest appreciation to Professor Toshiji Kanaya, Institute for Chemical Research, Kyoto University, and Professor Ryoichi Yamamoto, Department of Chemical Engineering, Kyoto University, for their kind review on this thesis.

The author also wishes to express his sincere thanks to Professor Yumi Matsumiya and Professor Yuichi Masubuchi, Institute for Chemical Research, Kyoto University, for their helpful guidance and advice.

The author especially wishes to express his sincere thanks to Professor Takashi Uneyama, at School of Natural System, College of Science and Engineering, Kanazawa University, for his continuous guidance and collaborations.

The author expresses his sincere thanks and appreciation for Dr. R. Graham at University of Nottingham who kindly allowed the author to utilize the GLaMM calculation results in Chapter 5 of this thesis.

The author also expresses thanks for Dr. J. A. Pathak and Dr. C. M. Roland at U. S. Naval Research Laboratory, for making the author aware of the problems of dielectric

responses under LAOS, and for their collaboration on the theoretical analysis in Chapter 3 of this thesis.

The author is deeply indebted to Professor Jay D. Schieber, The Center for the Molecular Study of Soft Condensed Matter, Illinois Institute of Technology and the members of Prof. Schieber's group for their invaluable discussions, collaborations and kind arrangements during his stay in Chicago.

Special Thanks are also due to Ms. Yukie Kajikawa, Dr. Quan Chen, Dr. Changkwon Chung, Dr. Hideaki Takahashi, Dr. Kenji Furuichi, Mr. Shinya Suzuki, Mr. Takatoshi Yaoita, Mr. Jun Takada, and to all the other past and current members in Prof. Watanabe's group for their continuous support and friendly cooperation.

The author acknowledges with thanks for Polyplastics Co., Ltd. for valuable supports.

The author is grateful for the financial support from the Japan Society for Promotion of Science from 2008 to 2011 (JSPS Research Fellowships for Young Scientists).

Finally, the author expresses heartfelt thanks to his wife, Shino Horio, his father, Tetsuo Horio, his mother Setsuko Horio, his daughter, Miyu Horio, for their continuous support, encouragement and patience during this work.

March, 2014

Kazushi Horio